

Advanced Electrode Materials for Efficient Hydrogen Production in Protonic Ceramic Electrolysis Cells

Zhipeng Liu, Lilin Zhang, Chunyue Joey Zheng, Yuan Zhang, Bin Chen,* Zongping Shao, and Jingjie Ge*

Protonic ceramic electrolysis cells (PCECs) exhibit superior proton conductivity under intermediate-temperature operation (300–600 °C), emerging as a promising water electrolysis technology compared to traditional low-temperature proton-conducting polymer electrolysis and high-temperature oxygen ion-conducting oxide electrolysis. However, the sluggish kinetics of the oxygen evolution reaction (OER) and electrode instability in PCECs hinder their large-scale development. This review highlights recent advancements in PCEC technology, emphasizing its thermodynamic and kinetic advantages, the categorization of advanced electrode materials, and material regulation strategies, including chemical doping, microstructural engineering, and multiphase design to improve their catalytic performance and stability. Additionally, the current challenges are discussed and future research directions are outlined for advanced PCEC electrode materials. By summarizing recent advancements in electrode materials and their optimization strategies, this review provides valuable insights into the rational design of efficient and stable electrode materials, advancing PCEC technology for green hydrogen production.

prospected growth in industrial demand for green hydrogen, water electrolysis coupled with renewable energy technologies is considered one of the main future trends for green hydrogen synthesis.^[2] Compared with alkaline water (ALK) electrolysis, proton exchange membrane (PEM) electrolysis, and anion exchange membrane (AEM) electrolysis, solid oxide electrolysis cell (SOEC) technology is more attractive due to its unrivaled conversion efficiencies—a result of favorable thermodynamics and kinetics at higher operating temperatures.^[3] However, such high temperatures can undermine the stability of SOECs, leading to issues such as electrode material degradation^[4] and delamination between the electrode and electrolyte interfaces.^[5] Furthermore, the hydrogen produced in these systems often further requires costly purification and drying processes, as it is mixed with water vapor at the fuel electrode.^[6]

1. Introduction

As worldwide energy demands grow and the severity of environmental challenges worsen, the global shift toward green energy, particularly advancements in efficient hydrogen-based energy systems, has become a key priority worldwide.^[1] Given a

To overcome these limitations, researchers are shifting their focus to protonic ceramic electrolysis cells (PCECs), utilizing proton conductors as electrolytes instead of oxygen ion conductors.^[7] PCECs facilitate efficient hydrogen production at intermediate temperatures (400–700 °C), benefiting from reduced activation energy requirements for proton conduction^[8] This operating

Z. Liu, L. Zhang, J. Ge
 Department of Applied Biology and Chemical Technology
 The Hong Kong Polytechnic University
 Hung Hom
 Kowloon, Hong Kong 999077, China
 E-mail: jingjie.ge@polyu.edu.hk
 C. J. Zheng
 Sha Tin College
 Fo Tan
 New Territories
 Hong Kong 999077, China

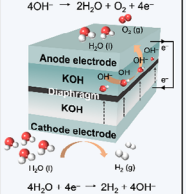
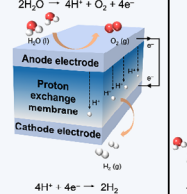
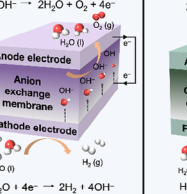
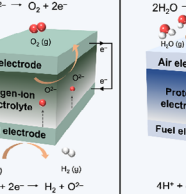
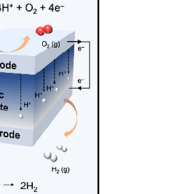
Y. Zhang
 Graphene Composite Research Center
 College of Chemistry and Environmental Engineering
 Shenzhen University
 Shenzhen 518060, P. R. China
 B. Chen
 State Key Laboratory of Intelligent Construction and Healthy Operation and Maintenance of Deep Underground Engineering
 Shenzhen Key Laboratory of Deep Underground Engineering Sciences and Green Energy
 College of Civil and Transportation Engineering
 Shenzhen University
 Shenzhen 518060, China
 E-mail: chenbin@szu.edu.cn
 Z. Shao
 Department of Chemical Engineering
 Curtin University
 Perth, Western Australia 6845, Australia

The ORCID identification number(s) for the author(s) of this article can be found under <https://doi.org/10.1002/adma.202503609>

© 2025 The Author(s). Advanced Materials published by Wiley-VCH GmbH. This is an open access article under the terms of the [Creative Commons Attribution-NonCommercial](#) License, which permits use, distribution and reproduction in any medium, provided the original work is properly cited and is not used for commercial purposes.

DOI: 10.1002/adma.202503609

Table 1. Comparative analysis of typical characteristics for ALK, PEM, AEM, SOEC, and PCEC in green hydrogen production systems. Data for efficiency, advantages, and disadvantages from refs. [10a] and [10b]; data for hydrogen production cost and development status from ref. [10c].

Technology Type	Alkaline Water Electrolysis (ALK)	Proton Exchange Membrane (PEM)	Anion Exchange Membrane (AEM)	Solid Oxide Electrolysis Cell (SOEC)	Proton Ceramic Electrolysis Cell (PCEC)
Schematic Diagram of the Technical Principles	$4\text{OH}^- \rightarrow 2\text{H}_2\text{O} + \text{O}_2 + 4\text{e}^-$  $4\text{H}_2\text{O} + 4\text{e}^- \rightarrow 2\text{H}_2 + 4\text{OH}^-$	$2\text{H}_2\text{O} \rightarrow 4\text{H}^+ + \text{O}_2 + 4\text{e}^-$  $4\text{H}^+ + 4\text{e}^- \rightarrow 2\text{H}_2$	$4\text{OH}^- \rightarrow 2\text{H}_2\text{O} + \text{O}_2 + 4\text{e}^-$  $4\text{H}_2\text{O} + 4\text{e}^- \rightarrow 2\text{H}_2 + 4\text{OH}^-$	$2\text{O}^{2-} \rightarrow \text{O}_2 + 2\text{e}^-$  $\text{H}_2\text{O} + 2\text{e}^- \rightarrow \text{H}_2 + \text{O}^{2-}$	$2\text{H}_2\text{O} \rightarrow 4\text{H}^+ + \text{O}_2 + 4\text{e}^-$  $4\text{H}^+ + 4\text{e}^- \rightarrow 2\text{H}_2$
Temperature Range	70–90 °C	50–80 °C	40–60 °C	700–900 °C	400–600 °C
Efficiency	60–70 %	65–75 %	60–75 %	70–90 %	80–90 %
Hydrogen Production Cost	2.8–3.5 \$/kg	3.5–4.9 \$/kg	2.5–3.2 \$/kg	2.8–4.2 \$/kg	5.6–8.3 \$/kg
Advantages	Mature technology, low capital cost, long lifetime	Rapid response, high hydrogen purity, compact design	Lower cost, suitable for mobile power sources	High efficiency, non-noble metal catalysts	Mid-temperature efficiency, simplified system, intermittency compatibility
Disadvantages	Low efficiency, frequent electrolyte maintenance	High catalyst cost, membrane degradation	Low efficiency, lower ion conductivity	Limited thermal cycling tolerance	Material instability, early-stage technical maturity
Development Status	Mature	Commercialized	Research and development	Research and development	Research and development

temperature range mitigates the degradation of metal-ceramic materials or perovskite materials, thereby improving the overall catalytic efficiency of hydrogen production.^[9] Moreover, since water vapor is introduced at the air electrode, the hydrogen produced at the fuel electrode can be directly stored without purification, significantly reducing production costs. To systematically evaluate the trade-offs between these technologies' efficiency, advantages, and disadvantages, Table 1 provides a comparative analysis of ALK, PEM, AEM, SOEC, and PCEC systems.

The past fifteen years have witnessed the rapid development of PCEC, evidenced by current density performance boosted from $\approx 0.3 \text{ mA cm}^{-2}$ ^[11] to 6 A cm^{-2} ^[12] under 600 °C and 1.5 V conditions. The achievement of such high current density at low voltages surpasses the capabilities of state-of-the-art ALK and PEM water electrolysis. Consequently, PCEC emerges as the most efficient method for large-scale water electrolysis. However, its commercialization is still hindered by various challenges, particularly regarding the materials, including but not limited to weak mechanical strength of fuel electrode support, current leakage and poor sinter ability of electrolyte, and low catalytic activity of the air electrode. In terms of air electrode materials for PCEC, perovskite-type oxides (simple perovskite oxides $(\text{ABO}_{3-\delta})$,^[13] double perovskite oxides $(\text{AA}'\text{B}_2\text{O}_{6-\delta})$,^[14] and Ruddlesden-Popper (RP) phase oxides $(\text{A}_{n+1}\text{B}_n\text{O}_{3n+1})$ ^[15] together with layered compounds^[16] are current options that exhibit good performance. To further enhance their proton conduction activity performance, the perovskites can be tailored via chemical doping with alien alkaline earth metal, rare earth metal, and transition metal atoms to substitute the original metal atoms at the A and B sites.^[17] This modification of the surface properties and bulk diffusion of the pristine perovskite leads to increased conductive activity of protons and oxygen ions. In terms of fuel electrode materials for PCEC, metal-based cermets, particularly those based on Ni, are widely utilized due to their high catalytic activ-

ity and stability in reducing atmospheres. However, challenges such as Ni migration and aggregation in Ni-based cermets result in an irreversible decline in performance.^[18] These issues can be alleviated by tailoring the electrode microstructure and optimizing the electrode–electrolyte interface, which effectively suppress Ni coarsening and migration.^[19] Additionally, certain non-perovskites such as carbon materials also serve as high-performance fuel electrodes, due to their exceptional properties in mass and charge transport, electrical and thermal conductivity, as well as mechanical and chemical stability.^[20] To optimally design highly efficient yet durable PCEC materials, a thorough understanding of the catalytic mechanism of the active sites is needed to regulate their catalytic performance, which plays a crucial role in enhancing the catalytic activity and stability of PCEC electrodes.

In this review, we explore the latest advancements in PCEC, beginning with its fundamental principles, which highlight the thermodynamic, kinetic, and potential durability advantages of PCEC over conventional ALK, PEM, AEM and SOEC technologies. We then categorize advanced electrode materials, focusing on their roles in enhancing catalytic activity and operational stability. Additionally, we outline strategies to improve their catalytic activity and stability, focusing on chemical doping, microstructure optimization, and multiphase regulating strategies. These methods aim to enhance performance by tuning atomic-level substitutions, optimizing electrode microstructure, and constructing multiphase composites. Finally, we discuss the key challenges and promising research directions for future development. Figure 1 comprehensively outlines the advantages and challenges of PCEC, including a systematic classification of state-of-the-art electrode materials, corresponding performance-enhancing strategies, and future research directions, thereby visually integrating the critical technical and developmental themes addressed in this review.

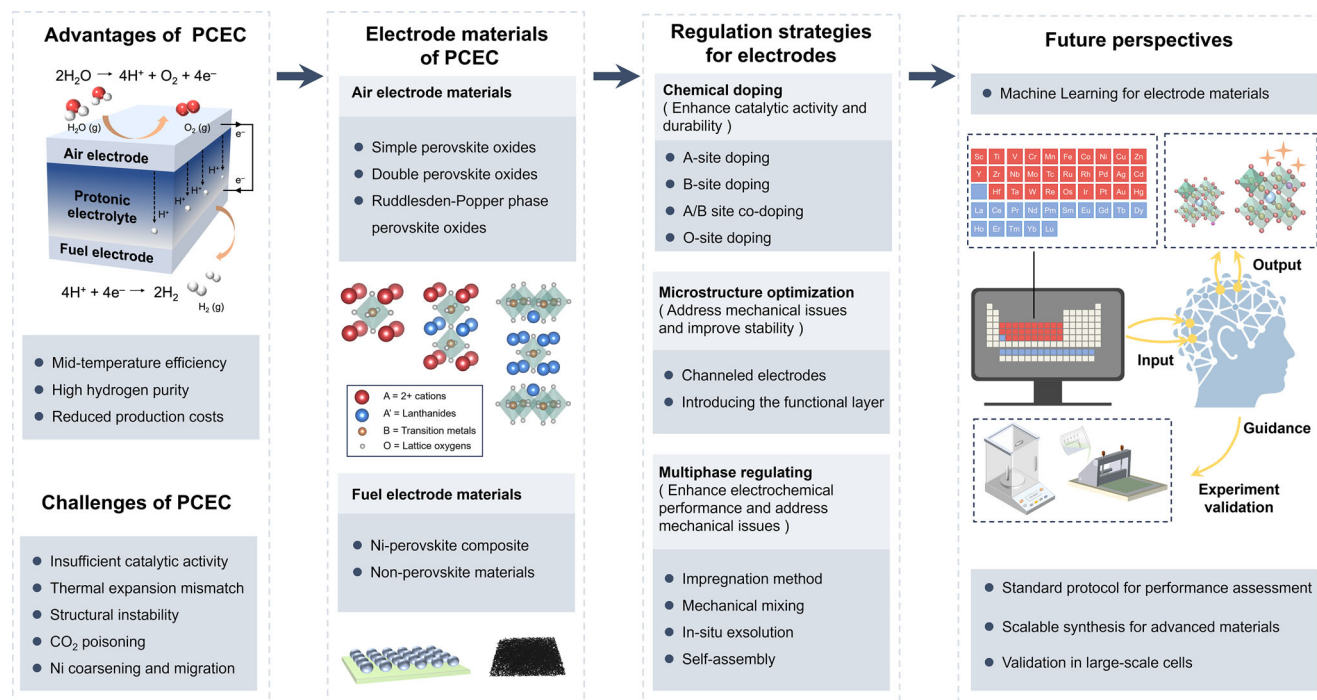


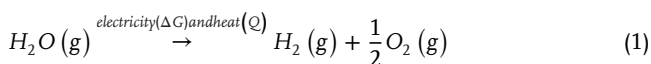
Figure 1. Schematic illustration of protonic ceramic electrolysis cells, highlighting the advantages and challenges of PCEC, as well as the advanced electrode materials associated with regulation strategies and future perspectives summarized in this work.

2. Fundamentals of PCEC

Unlike water electrolysis processes such as ALK and PEM cells that operate at low temperatures (<100 °C), PCEC operates at higher temperatures (350–600 °C) and exhibits distinct thermodynamic characteristics. This is attributed to the fact that both changes in enthalpy and entropy vary with temperature, affecting the energy required for water electrolysis at high and low temperatures. Additionally, the proton conduction in PCECs involves different activation energies and conduction pathways than the oxygen ion conduction in SOECs, due to the differing radii of hydrogen and oxygen ions. To better understand the fundamental principles of PCEC, the thermodynamics and related proton uptake and conduction mechanisms for water electrolysis in PCEC are introduced in this section.

2.1. Thermodynamics of PCEC

Steam can be split into hydrogen and oxygen under the influence of high-temperature generated heat and electricity.^[21] The reaction for steam electrolysis is represented in Equation (1).



The total energy $\Delta H(T)$ required for water steam electrolysis is $\Delta G(T)$ plus $Q(T)$:

$$\Delta H(T) = \Delta G(T) + Q(T) \quad (2)$$

where $\Delta G(T)$ is the minimum electric work demand by the electrolysis process, $Q(T) = T\Delta S(T)$ is the heat energy consumed for generating electricity and electrolysis process, and $\Delta H(T)$ is the standard enthalpy for the whole reaction at T .

The standard thermodynamic parameters ΔH and ΔS at different temperatures can be calculated according to Equations (3) and (4).

$$\Delta H = \Delta H_{298.15}^\circ + \int_{298.15}^T \Delta C_p dT \quad (3)$$

$$\Delta S = \Delta S_{298.15}^\circ + \int_{298.15}^T \frac{\Delta C_p}{T} dT \quad (4)$$

where ΔC_p is the constant-pressure molar heat capacity.

The electromotive force E_{mf} (also known as the Nernst voltage) and thermoneutral voltage U_{in} (also known as the enthalpy voltage) at unit activity and standard pressure can be calculated according to Equations (5) and (6).

$$Emf = -\frac{\Delta G}{nF} \quad (5)$$

$$U_{in} = -\frac{\Delta H}{nF} \quad (6)$$

where n is the number of electrons transferred during the water electrolysis reaction and F is the Faraday constant.

Through the above equations, the fundamental thermodynamic parameters at various temperatures are presented in **Figure 2**. The results indicate that $H(T)$ increases slightly with rising temperatures, while $G(T)$ decreases due to the increase in $Q(T)$. The ratio of $G(T)$ to $H(T)$ continues to drop as the

temperature rises, enhancing the thermal-to-hydrogen energy conversion efficiency as electrical energy demand decreases. Additionally, the total energy demand for liquid water electrolysis is higher than that for steam electrolysis, making large-scale water electrolysis (ALK and PEM) more energy-intensive than steam electrolysis when producing the same amount of hydrogen.

In practice, due to the presence of additional voltages, the equilibrium voltage U_{el} is generally significantly higher than the E_{mf} :

$$U_{el} = E_{mf} + U_{act} + U_{conc} + U_{ohm} \quad (7)$$

where the activation overvoltage, U_{act} , is the extra voltage required to satisfy the electrochemical kinetics of the electrode, which is related to the activation energy, electrolysis rate, and temperature; the concentration overvoltage, U_{conc} , reflects the loss in gas concentration caused by diffusion resistance within the porous electrode, which is related to the electrolysis rate and geometric parameters; the ohmic overvoltage, U_{ohm} , is the voltage loss caused by the resistance of the connectors, electrodes, and electrolyte.

For Equation (1), the electrolysis efficiency is given by:

$$\eta_{el} = \frac{\Delta H}{nFU_{el}} = \frac{U_{in}}{U_{el}} \quad (8)$$

where nFU_{el} represents the electrical energy input during the reaction process. For low-temperature electrolysis (ALK or PEM electrolysis operating at $\approx 80^\circ\text{C}$), U_{el} is typically 1.2 to 1.8 times of U_{in} such that the electrolysis device releases heat to the surroundings and has a relatively low efficiency of $\approx 55\%$ to 83% .^[22]

For water electrolysis working at a higher temperature range, the thermodynamic and chemical kinetic characteristics of the electrolysis reaction are improved, and the ohmic resistance of the electrolyte is reduced, thereby U_{act} and U_{ohm} are significantly reduced. The terminal voltage of PCEC remains essentially unchanged and is also much lower than those of electrolysis technologies at ambient temperatures such as PEM, leading to a substantial increase in efficiency.

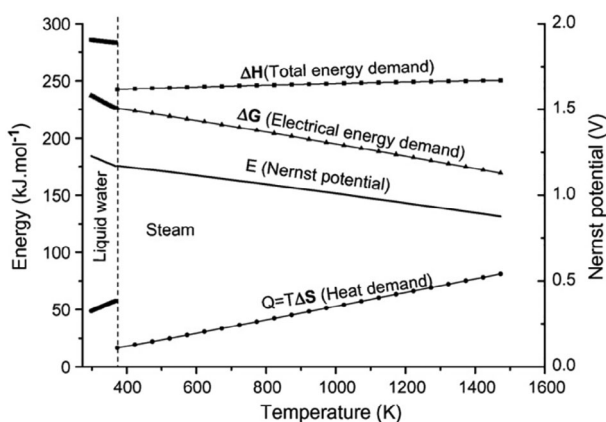


Figure 2. Energy demand for water and steam electrolysis. Reproduced with permission.^[21] Copyright 2007, Elsevier.

2.2. Proton Uptake and Conduction Mechanisms

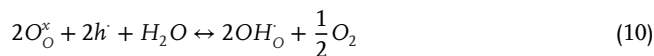
The materials used in various parts of PCEC, such as air electrodes, electrolytes, and fuel electrodes, do not inherently contain protons within their lattice structure. However, during the water electrolysis process, humid conditions facilitate interactions between water molecules and oxide ion vacancies or holes, which consequently generate protons. These interactions occur through hydration or hydrogenation reactions. Subsequently, the protons form hydrogen bonds with lattice oxygen. These protons are transported from the air electrode to the fuel electrode via the electrolyte, facilitating a continuous water electrolysis reaction. The processes of proton uptake and conduction are intricately linked to the structural and ionic conduction characteristics of the materials used in PCEC. Therefore, a thorough understanding of the proton conduction mechanism within PCEC is crucial for designing high-performance proton-conducting electrodes and electrolytes.

Typically, there are three possible reaction mechanisms for proton uptake in oxides: hydration, hydrogenation, and new-type hydration mechanisms. The hydration mechanism, first proposed by Kreuer et al.,^[23] requires the presence of oxide ion vacancies. These vacancies may be formed intrinsically by varying the ratio of the main constituents or be formed extrinsically to compensate for another dopant chemical element. This is clearly described in Equation (9), using the Kröger–Vink notation.



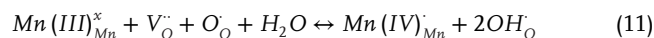
In this mechanism, the dissociation of H_2O produces a hydroxide ion (OH^-) and a proton (H^+), which then fills the oxygen vacancy ($\text{V}_\text{O}^\bullet$) and bonds with the lattice oxygen (O_O^\times) at the site of a lattice oxide ion (O^{2-}), respectively. This leads to the incorporation of two mobile proton defects (OH_O) within the lattice structure (Figure 3a).

Considering certain materials exhibit both oxygen vacancies and electron holes (typical for perovskite proton conductors), the related mechanism is described by Equation (10).



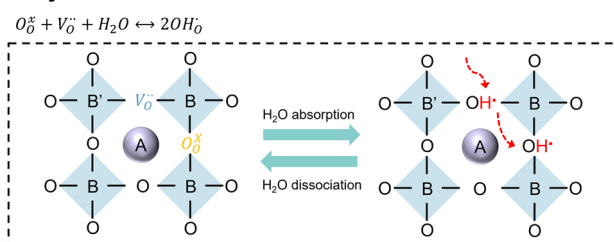
In this mechanism, the generation of protons occurs through a hydrogenation reaction. This process involves incorporating hydrogen into the material, which then interacts with the existing electron holes (h^\bullet). As a result of this interaction, protons are produced and oxygen is released as a byproduct. This mechanism highlights the dual role of oxygen vacancies and electron holes in facilitating proton conduction, as illustrated in Figure 3b.

Apart from the above two common mechanisms for proton uptake, a new mechanism was observed in the $\text{La}_{0.7}\text{Sr}_{0.3}\text{MnO}_{3-\delta}$ ^[24] through the hydration reaction mediated by Mn oxidation.

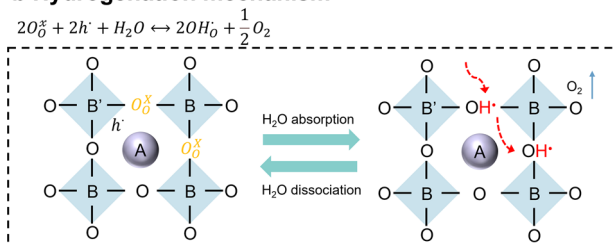


In this mechanism, proton uptake is driven by coupling the interaction of oxygen vacancies with water molecules together with the exchange reaction between oxygen holes and metals (Figure 3c). Specifically, in $\text{La}_{0.7}\text{Sr}_{0.3}\text{MnO}_{3-\delta}$, Mn cations exhibit mixed valence states. When O^{2-} is incorporated into an oxygen

a Hydration mechanism



b Hydrogenation mechanism



c New hydration mechanism

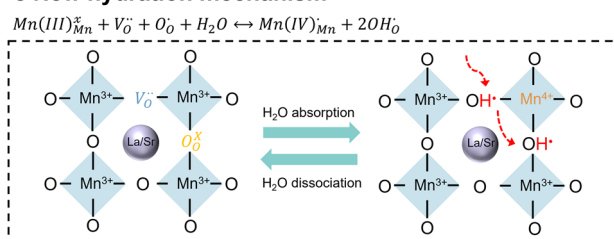


Figure 3. Three types of proton uptake mechanisms: a) hydration mechanism, b) hydrogenation mechanism, and c) new-type hydration mechanism.^[24]

vacancy, it leads to the oxidation of adjacent Mn cations from Mn^{3+} to Mn^{4+} . Concurrently, the oxygen holes are replaced by protons from water to neutralize the excess positive charge resulting from Mn oxidation.

Upon the formation of hydrogen ions, it is imperative to explore the mechanisms of proton conduction. The Grotthuss and Vehicle mechanisms are two distinct models that describe the transport of protons in ceramic oxide media.^[25] The Grotthuss mechanism, also known as the proton hopping or proton relay mechanism, describes the rapid transport of protons through a network of hydrogen-bonded water molecules with other hydrogen-bonded networks, facilitated by low activation energy. When water dissociates into protons and hydroxide ions, the proton forms a covalent bond with lattice oxygen. The resulting hydroxyl group bends toward adjacent oxygen ions, reducing the bond length and lowering the energy barrier for proton transfer to enable proton transfer via hydrogen bond breaking and formation. Subsequently, proton migration occurs, where protons hop between neighboring oxide ions to break weak O—H bonds and form new ones with the adjacent oxygen ions.^[26] The total activation energy required for proton rotation and hopping is relatively low (<0.4 eV). In contrast, the Vehicle mechanism describes proton transport in which the proton is carried by a larger molecular entity—specifically O^{2-} in the context of ceramic oxides.

Through this mechanism, proton transport is tied directly to the diffusion of the OH^- (with O^{2-} carrying H^+) into the oxygen vacancy. This process requires a higher activation energy, (>0.4 eV), which makes it generally slower than the Grotthuss mechanism. A representative study on $LaMO_3$ ($M = Cr, Mn, Fe$) perovskites demonstrates that oxygen vacancy engineering can directly switch the dominant mechanism: defect-free surfaces favor Grotthuss-type proton hopping, whereas oxygen-deficient surfaces promote Vehicle-driven transport due to vacancy-induced electron redistribution weakening O—H bonds.^[25a] This highlights the critical role of defect chemistry in tailoring proton conduction pathways for energy applications.

3. Air Electrode Materials in PCEC

3.1. Introduction of Air Electrode Materials in PCEC

In traditional solid oxide fuel cells (SOFCs) that use oxygen ion-conducting electrolytes, $La_{0.8}Sr_{0.2}MnO_3$ (LSM) is a widely used air electrode material due to its high electronic conductivity, superior catalytic activity and stability, and excellent thermal and chemical compatibility with other cell components, including the electrolyte. However, LSM typically performs poorly below 700°C , where its ionic conductivity significantly decreases. This reduction limits the triple-phase boundary (TPB) at the intersection of the electrolyte, air electrode, and gas, leading to a rapid decline in overall cell performance.^[27] In contrast, proton-conducting electrolytes in PCECs demonstrate higher ionic conductivity and theoretical efficiency over a lower temperature range.^[28] Therefore, current research is increasingly focused on proton-conducting electrolytes for PCECs. In PCECs, the electrolyte mode functions reversely to traditional fuel cells, allowing the composition of the cell components to remain essentially unchanged. The air electrode is vital in facilitating the oxygen reduction reaction (ORR) and the oxygen evolution reaction (OER). To ensure optimal cell performance, the air electrode requires sufficient catalytic activity, adequate ionic conductivity (H^+/O^{2-}) and electronic conductivity (e^-).^[29] The air electrode must further satisfy several key requirements, including ease of synthesis, thermal stability, and chemical stability. Consequently, research on selecting appropriate materials and designing the electrode structure has become a priority to develop air electrodes that meet all the criteria: high ORR/OER activity at intermediate temperatures, a thermal expansion coefficient (TEC) compatible with other cell components (especially the electrolyte), excellent thermal cycling stability, good chemical compatibility, high conductivity, and ease of synthesis.^[30] Despite these challenges, various methods have been developed to prepare air electrodes with diverse characteristics and advantages. This review categorizes these advanced air electrode materials into three main types, i.e., simple perovskite, double perovskite, and RP phase perovskite (Figure 4).

3.2. Simple Perovskite Air Electrodes

In the early research stages of PCEC, typical ABO_3 perovskite electrode materials, such as $La_{0.6}Sr_{0.4}Co_{0.2}Fe_{0.8}O_{3-\delta}$ (LSCF),

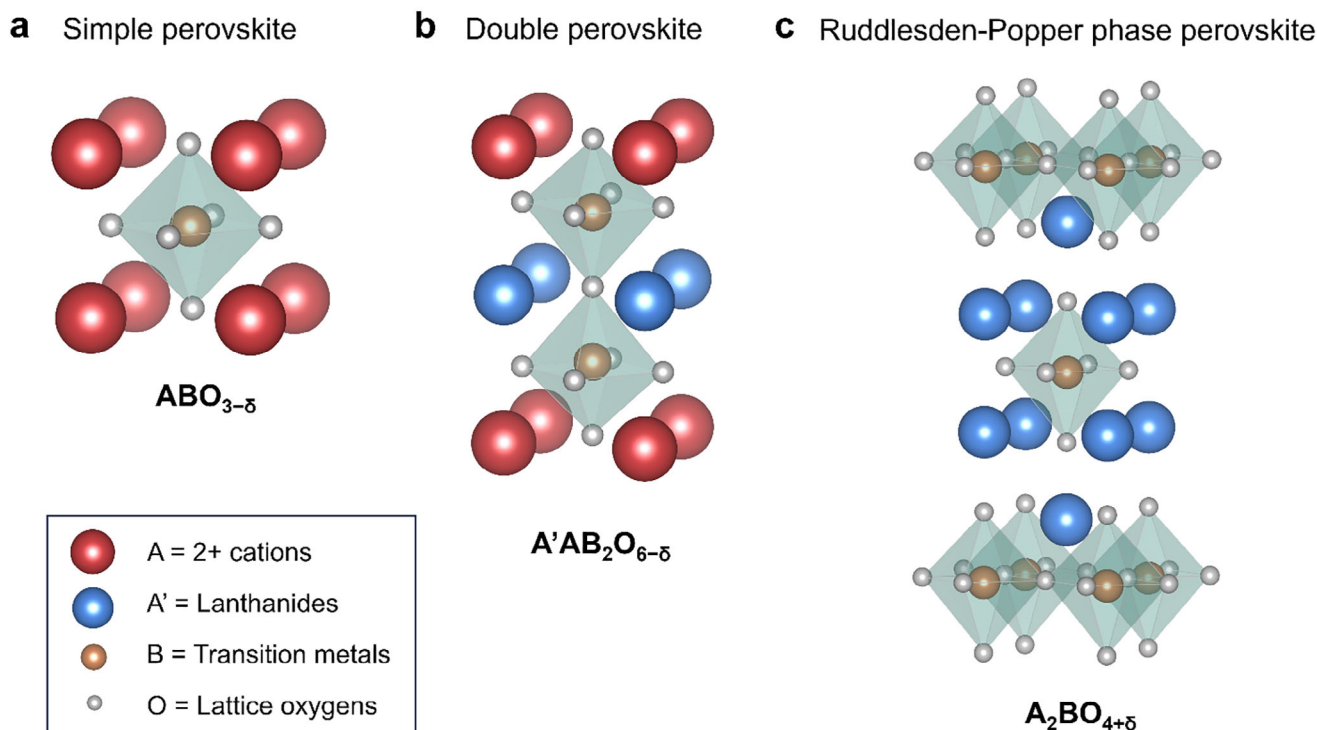


Figure 4. The schematic diagram for phase structures of a) simple perovskite, b) double perovskite, and c) RP phase perovskite.

$Ba_{0.5}Sr_{0.5}Co_{0.8}Fe_{0.2}O_{3-\delta}$ (BSCF), and $SrSc_{0.175}Nb_{0.025}Co_{0.8}O_{3-\delta}$ (SSNC), were commonly investigated.^[31] Although these materials perform exceptionally well in SOECs, insufficient proton conductivity and poor chemical stability in the humid air conditions used in PCECs reduce activity and operational stability. Research indicated that lowering the operational temperature could alleviate degradation challenges like electrode coarsening and various chemical interactions. However, this would simultaneously slow down the ORR and OER. Therefore, designing air electrode materials that sustain high activity at lower temperatures has emerged as a primary research objective. Recently, several novel cubic-phase ABO_3 perovskite air electrode materials, including $BaCo_{0.4}Fe_{0.4}Zr_{0.1}Y_{0.1}O_{3-\delta}$ (BCFZY), $Ba_{0.9}Co_{0.7}Fe_{0.2}Nb_{0.1}O_{3-\delta}$ (BCFN), and $PrNi_{0.5}Co_{0.5}O_{3-\delta}$ (PNC), have demonstrated considerable potential in both proton-conducting fuel cells (PCFC) and PCECs.^[32]

Among the ABO_3 perovskite air electrode materials, BCFZY has been extensively studied as the most promising potential air electrode due to its excellent performance in proton-conducting PCECs, outstanding redox activity, and the ability to conduct electrons, oxygen ions, and protons at the three-phase boundary. In terms of its crystal structure, BCFZY is a highly convenient oxide system, crystallizing at room temperature in a cubic perovskite structure (ABO_3) with the space group $Pm\bar{3}m$.^[33] Since BCFZY possesses the highest symmetry among ABO_3 compounds, it remains stable and does not undergo phase transitions at evaluated temperatures. Currently, doping a small amount of transition metal elements into BCFZY has proven to be an effective method to improve activity and stability. Liang et al.^[34] doped a small amount of magnesium (5%) into the

BCFZY system, producing a cubic-phase perovskite material, $Ba(Co_{0.4}Fe_{0.4}Zr_{0.1}Y_{0.1})_{0.95}Mg_{0.05}O_{3-\delta}$ (BCFZYM) that had triple conductivity (Figure 5a,d-e). Alongside improving the oxygen ion and proton conductivity, this slight magnesium doping significantly improved oxygen/vapor surface exchange. Cells with BCFZYM air electrodes achieved a peak power density of 850 mW cm^{-2} in fuel cell (FC) mode and a peak current density of 1244 mA cm^{-2} at 1.3 V in electrolysis cell (EC) mode, both measured at 600°C . Notably, the cells showed good stability, operating in EC mode for 200 h and FC mode for 300 h, and no significant performance degradation during 110 h of cyclic operation between FC and EC modes. Additionally, Shao et al.^[35] investigated the effects of various transition elements, including Mn, Ni, Cu, and Zn, on the BCFZY system. They found that doping Ni into $Ba(Co_{0.4}Fe_{0.4}Zr_{0.1}Y_{0.1})_{0.95}Ni_{0.05}O_{3-\delta}$ (BCFZYN) enhanced oxygen mobility, surface exchange kinetics, and both bulk oxygen ion and proton conductivities (Figure 5b,c). This led to higher ORR activity in proton-conducting PCFCs. Notably, at 550°C , the polarization resistance of symmetrical cells supported by proton conductors was reduced to $0.607 \Omega \text{ cm}^2$, and single cells with BCFZYN air electrodes achieved a peak power density of 450 mW cm^{-2} . Ryan et al.^[36] investigated the effects of varying Co/Fe ratios on electrocatalytic activity, electronic conductivity, oxygen ion binding and transport kinetics, and thermo-mechanical behaviors. Their studies revealed that the cobalt-rich $BaCo_{0.7}Fe_{0.1}Zr_{0.1}Y_{0.1}O_{3-\delta}$ (BCFZY7111) exhibited the highest performance due to its maximal oxygen vacancy content. Proton ceramic button cells using BCFZY7111 air electrodes achieved a peak power density of 695 mW cm^{-2} in FC mode, with an electrolysis current density of 1976 mA cm^{-2} at 600°C and 1.4 V.

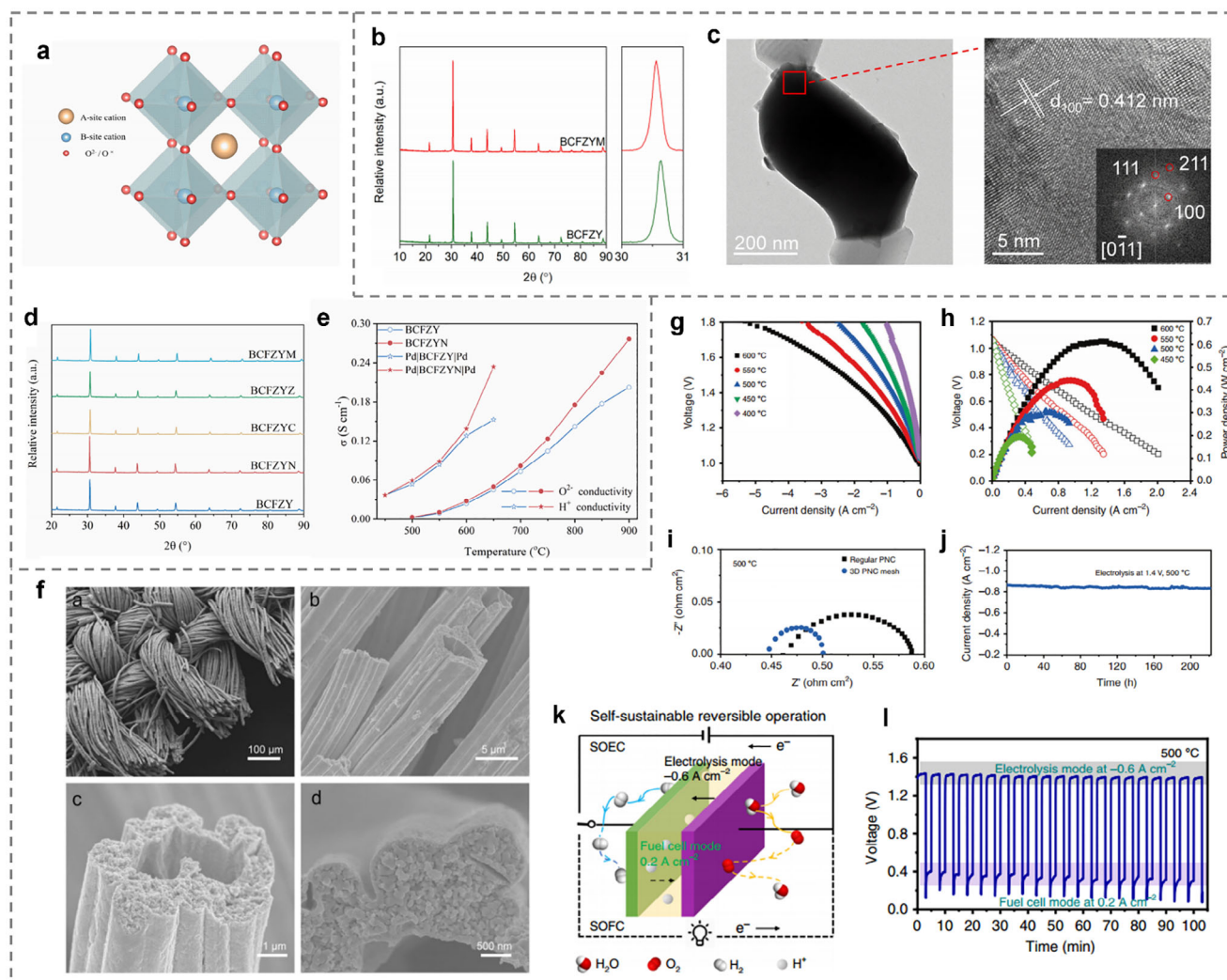


Figure 5. a) Schematic diagram of the ABO_3 -type perovskite structure. b) XRD patterns of BCFZY, BCFZYN, BCFZYC, BCFZYZ, and BCFZYM powders, and corresponding. c) ASRs in BZCYYb-supported symmetrical cells. d) XRD patterns of BCFZY and BCFZYM oxides. e) TEM and corresponding FFT images of the BCFZYM oxide. f) SEM images of the PNC electrode mesh with different magnification showing hollow-fiber-like string self-architecture to form mesh structure. g) I–V curves measured in the electrolysis mode. h) Performance in fuel cell mode. i) Comparison of impedance spectra under 1.4 V at 500 °C for cells with regular or 3D PNC electrodes. j) Durability testing of the cell in electrolysis mode at 500 °C. k) Schematic of self-sustainable reversible operation without external hydrogen feeding. l) Voltage observation under switchable electrolysis and fuel cell current densities at 500 °C. (a,d,e) Reproduced with permission.^[34] Copyright 2022, Elsevier. (b,c) Reproduced with permission.^[35] Copyright 2021, Elsevier. (f–l) Reproduced under the terms of the CC-BY Creative Commons Attribution 4.0 International license^[37] Copyright 2020, The Authors, published by Springer Nature.

Another common simple cubic perovskite air electrode system is PNC, proposed by Ding et al.,^[37] which has demonstrated enhanced hydration capacity and proton conductivity. PNC allows single cells to generate hydrogen via electrolysis and convert it back to electrical energy without requiring additional hydrogen, demonstrating self-sustainability and reversible operability. Additionally, Ding et al. optimized the microstructure of the three-phase conductive PNC electrode (Figure 5f), which improved overall gas diffusion and, consequently, the electrochemical performance of this PCEC. Namely, this electrode's electrolysis current density exhibited significant increments across various temperatures. Specifically, at 1.3 V and 600 °C, the current density peaked at 1.18 A cm^{-2} (Figure 5g–j), compared to 0.85 A cm^{-2} for conventional PNC. In FC mode, the peak power density increased

to 611 mW cm^{-2} at 600 °C, marking a 15.7% improvement. This work is the first to successfully demonstrate the self-sustained conversion of electrical energy and hydrogen by cycling between EC and FC modes (Figure 5k,l).

Currently, most air electrodes are composed of water-sensitive perovskite materials with specific ABO_3 crystal structures.^[38] Consequently, the alkaline earth metal cations at the A-site are prone to hydrolysis reactions when exposed to humid environments during extended electrolysis. The performance of perovskite materials is significantly influenced by their surface chemical properties, which are affected by water adsorption, leading to structural degradation and diminished electrochemical performance.^[39] Therefore, developing perovskite materials that can maintain high catalytic activity and structural stability under

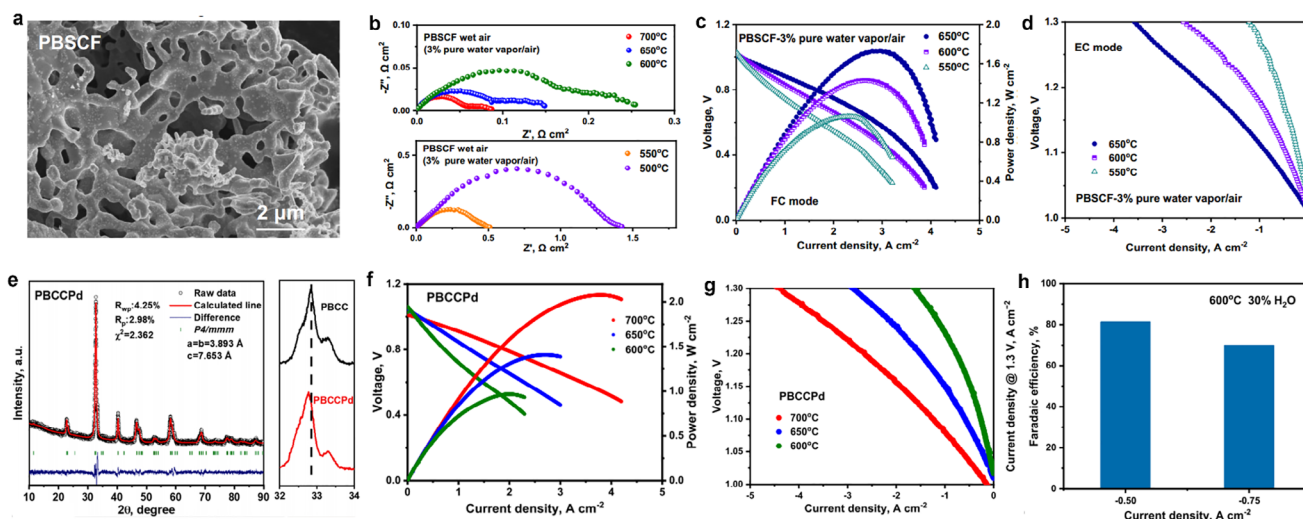


Figure 6. a) SEM images of PBSCF powders. b) EIS of PBSCF air electrode tested in 3% water vapor/air. c) The I–V–P curves of single cells tested in FC mode under 3% water air conditions. d) The I–V curves of single cells tested in EC mode under 3% water air conditions. e) Refined XRD profiles of PBCCPd powder fired at 1000 °C in air for 2 h. f) I–V–P curves of single cells with PBCCPd electrodes in FC mode. g) I–V curves of the R-PCECs with PBCCPd air electrode in EC mode. h) The Faradaic efficiencies of the R-PCEC with PBCCPd air electrode at -0.5 and -0.75 A cm $^{-2}$ in wet air with 30 vol.% H $_2$ O at 600 °C. (a–d) Reproduced with permission.^[48] Copyright 2024, Royal Society of Chemistry. (e–h) Reproduced with permission.^[47] Copyright 2024, Elsevier.

high temperature and humidity conditions, such as double perovskites and RP structured perovskites, has become a prominent research focus.

3.3. Double Perovskite Air Electrodes

Double perovskite structured materials typically have the general formula AA'B $_2$ O $_{6-\delta}$, where A represents a trivalent lanthanide cation, A' is barium or strontium, and B is a transition metal cation or a mixture of different elements, such as GdBaMn $_2$ O $_{6-\delta}$ and GdBaCo $_2$ O $_{6-\delta}$.^[40] Compared to simple perovskite materials, studies on conductivity relaxation and depth profiles of ion exchanges have revealed that double perovskites exhibit significantly faster oxygen surface exchange properties alongside oxygen ion and proton transport rates, and improved electronic conductivity due to their large cation ordering.^[41]

For example, double perovskites based on LnBaCo $_2$ O $_{6-\delta}$ (where Ln is a lanthanide element) feature alternating stacks of Ln–O and Ba–O layers along the crystal c-axis, resulting in preferential oxygen vacancies appearing in the Ln–O layers. This provides a pathway that facilitates rapid transport of oxygen ions or protons.^[42] Although there hasn't been sufficient research to clearly support the specific roles of these defects, oxygen vacancies are generally believed to facilitate surface reactions.^[43] Though, double perovskites LnBaCo $_2$ O $_{6-\delta}$, where Ln = La, Pr, Nd, Sm, and Gd, have been explored in multiple studies. Among them, Vøllestad et al. reported Ba $_{1-x}$ Gd $_{0.8}$ La $_{0.2+x}$ Co $_2$ O $_{6-\delta}$ (BGLC) as the most promising mixed proton and electronic conductor for use in proton ceramic cells. It was shown that the composite oxygen electrode Ba $_{0.5}$ Gd $_{0.8}$ La $_{0.7}$ Co $_2$ O $_{6-\delta}$ –BaZr $_{0.1}$ Ce $_{0.2}$ Y $_{0.1}$ O $_3$ – δ demonstrated a polarization resistance of less than 1 Ω cm 2 at 600 °C in tubular PCC cells and exhibited good stability for over 700 h at -62.5 mA cm $^{-2}$ in EC mode.^[44]

Moreover, several double perovskite oxides exhibit excellent performance as air electrodes in proton ceramic electrochemical cells due to their remarkable ability to conduct electrons, oxygen ions, and protons. These include PrBa $_{0.5}$ Sr $_{0.5}$ Co $_{1.5}$ Fe $_{0.5}$ O $_{5+\delta}$ (PBSCF),^[45] PrBaCo $_{1.6}$ Fe $_{0.2}$ Nb $_{0.2}$ O $_{5+\delta}$ (PBCFN),^[46] and PrBa $_{0.8}$ Ca $_{0.2}$ Co $_2$ O $_{5+\delta}$ (PBCC).^[47] This was proven as Du et al.^[48] revealed that the classic double perovskite air electrode PBSCF has an area-specific resistance (ASR) of only 0.269 Ω cm 2 at 600 °C, shown in Figure 6a,b. It also achieved a peak power density of 1.388 W cm $^{-2}$ in FC mode (Figure 6c) and that of -2.392 A cm $^{-2}$ in EC mode (Figure 6d) when in humid environments of 600 °C. Additionally, Xu et al.^[46] reported that the PBCFN air electrode achieved a current density of 2148 mA cm $^{-2}$ at 1.3 V and 650 °C in 3% H $_2$ O-air, demonstrating desirable durability for 200 h. Moreover, Zhou et al.^[47] prepared PBCC air electrodes, which achieved a current density of 1510 mA cm $^{-2}$ at 1.3 V and 600 °C in 3% H $_2$ O-air, whilst Du et al.^[49] reported that the PrBa $_{0.8}$ Ca $_{0.2}$ Co $_{1.95}$ Pd $_{0.05}$ O $_{5+\delta}$ (PBCCPd) double perovskite air electrode (Figure 6e) exhibited a polarization resistance of 0.056 Ω cm 2 at 700 °C in a BaZr $_{0.1}$ Ce $_{0.7}$ Y $_{0.1}$ O $_3$ (BZCYYb)-based symmetrical cell, achieving a peak power density (PPD) of 2.08 W cm $^{-2}$ in FC mode and a current density of -4.42 A cm $^{-2}$ at 1.3 V in EC mode, shown in Figure 6f–g. Furthermore, the PCEC composited with PBCCPd air electrodes showed excellent stability in both FC and EC modes, achieving a high Faradaic efficiency of up to 81.26% (Figure 6h).

3.4. Ruddlesden–Popper Phase Perovskite Air Electrode

Due to the limitations of simple perovskite air electrodes in achieving durable, high catalytic activity for ORR in the medium to low-temperature range in PCECs, extensive research has been conducted on RP perovskites. It has been found that RP

perovskites exhibit rapid oxygen surface exchange kinetics and excellent stability at medium to low temperatures, making them promising candidates for further exploration in this field. RP perovskites have the general formula $A_{n+1}B_nO_{3n+1}$, characterized by alternating layers of ABO_3 perovskite and AO rock salt along the c-axis.^[50] The A-site typically consists of rare earth or alkaline earth elements, while the B-site is occupied by transition metals such as Ni, Mn, Co, or Fe.^[51] The exact mechanism of proton transport in RP-type perovskites has not been definitively established, so most researchers still adhere to the widely accepted two-step Grotthuss mechanism for proton transport.^[52] The main features of proton defect transportation involve rotational diffusion and octahedral hopping; protons jump from one oxygen ion to a neighboring oxygen ion within the same octahedron, resulting in long-range diffusion of protons as the oxygen remains in its crystalline position.^[23] Evidently, Hermet et al.^[52b] revealed that proton transport in $BaCeO_3$ perovskite involves two processes: reorientation and transfer (or hopping), where protons can directly hop from one octahedron to another, nonetheless of geometry. Wang et al.^[52a] utilized a combination of theoretical (first-principles) and experimental methods to investigate two potential proton migration pathways, discovering that the highest barrier for proton migration is ca. 0.63 eV, which closely matches with the experimental findings.

RP structure perovskites are considered potential air electrode materials since they have the ability to avoid the surface segregation issues often associated with alkaline earth metals, which would otherwise negatively impact electrode performance.^[53] For instance, Druce et al.^[54] employed surface-sensitive low-energy ion scattering techniques to study the RP material $PrLaNiO_{4+\delta}$ to find no segregation of lanthanide cations, while the surface of LSCF exhibited significant Sr segregation. Little segregation is crucial the long-term stability of electrode materials. Moreover, RP-type perovskites demonstrate enhanced ORR activity alongside excellent thermal and chemical stability.^[55] These attributes make them attractive candidates for use in low-temperature solid oxide fuel cells. Bassat et al.^[56] calculated the ionic conductivity of RP-type $Ln_2NiO_{4+\delta}$ (where $Ln = La, Pr, Nd$) based on oxygen diffusion data, concluding that the RP perovskite exhibits significantly higher ionic conductivity at 700 °C compared to simple perovskites like LSCF ($\approx 3.7 \times 10^{-3} \text{ S cm}^{-1}$) and $La_{0.6}Sr_{0.4}Fe_{0.8}Ni_{0.2}O_{3-\delta}$ (LSFN) ($\approx 1.5 \times 10^{-3} \text{ S cm}^{-1}$). Additionally, compared to conventional perovskite LSCF ($D_{\text{chem}} \approx 5.40 \times 10^{-9} \text{ cm}^2 \text{ s}^{-1}$, $k_{\text{chem}} \approx 9.26 \times 10^{-8} \text{ cm s}^{-1}$), RP structure $Ln_2NiO_{4+\delta}$ ^[57] exhibits inherently higher oxygen diffusion ($D_{\text{chem}} \approx 4.15 \times 10^{-7} \text{ cm}^2 \text{ s}^{-1}$) and surface exchange kinetics ($k_{\text{chem}} \approx 7.57 \times 10^{-6} \text{ cm s}^{-1}$) at 700 °C. Gilev et al.^[58] also reported that $La_{1.5}Sr_{0.5}Ni_{1-y}Fe_yO_{4+\delta}$ and $La_{1.2}Sr_{0.8}Ni_{1-y}Fe_yO_{4+\delta}$ demonstrate rapid oxygen surface exchange characteristics. Moreover, a fuel electrode-supported cell with a $Pr_2NiO_{4+\delta}$ air electrode exhibited a power density exceeding 650 mW cm^{-2} at 0.8 V and 750 °C, with a degradation rate of only 1%–3% per 1000 h, starkly contrasting to cells with LSCF air electrodes which experienced a degradation rate of 10–20% over the same period. Zhou et al.^[59] demonstrated that the RP structure $Pr_2NiO_{4-\text{Ce}_{0.9}\text{Gd}_{0.1}O_{2-\delta}}$ air electrode offers excellent electrochemical performance and stability for reversible ceramic cells.

4. Fuel Electrode Materials in PCEC

4.1. Introduction of Fuel Electrode Materials in PCEC

The fuel electrode in a PCEC must meet several crucial requirements to optimally drive the hydrogen evolution reaction. First, it should demonstrate suitable ionic and electronic conductivities coupled with high catalytic activity.^[60] Additionally, the material must maintain its chemical and physical stability under reducing conditions while demonstrating compatibility with adjacent components, such as the electrolyte. This compatibility extends to having a well-matched TEC to ensure stability during redox reactions and thermal cycling.^[61] To ensure optimal performance, the fuel electrode is designed to serve as a structural support. Therefore, adequate mechanical strength and shock resistance are required to prevent the chances of cell failure during operation. Moreover, the electrode should possess appropriate porosity to facilitate rapid diffusion and transport of gases or electrolysis products.^[62] In this section, we primarily discuss three categories of fuel electrodes, including the widely used Ni-electrolyte composite electrodes, perovskite-based electrodes, and non-perovskite fuel electrodes.

4.2. Ni-Perovskite Composite Fuel Electrode

Currently, Ni-based materials are the most used fuel electrode materials in proton-conducting ceramic fuel cells. They are favored for their low cost, excellent catalytic activity, high conductivity, and compatibility with ceramic conductors.^[63] Mixing metallic Ni with proton-conducting electrolyte perovskite materials forms a triple-conducting composite, being the most common method to alleviate thermal expansion differences between the electrode and electrolyte while lengthening the TPB. A longer TPB can effectively reduce the electrochemical polarization resistance of the fuel electrode.^[60]

Besides mechanically mixing to create composite electrodes to increase TPB density, catalytic activity can be effectively enhanced via in situ generation of nanoscale catalytic materials.^[64] The precipitation of Ni nanoparticles appears to facilitate hydrogen production in EC mode and hydrogen oxidation in FC mode.^[65] During high-temperature operation, particularly under high current conditions, nanoscale Ni particles (less than 200 nm) can precipitate in situ from the fuel electrode, forming structures that have a significantly larger effective catalytic surface area. These in situ precipitated Ni nanoparticles bond closely with the electrolyte material, such as $BaZr_{0.8}Y_{0.2}O_{3-\delta}$ (BZY), effectively reducing the migration distance between Ni and BZY.^[66] This results in a high specific surface area, leading to improved catalytic activity and coke resistance. Interestingly, the precipitation of Ni creates unique interfaces that can enhance stability and reduce the tendency for coking with hydrocarbons—a trend confirmed with the $La_{0.4}Sr_{0.4}Ni_{0.03}Ti_{0.97}O_{3-\delta}$ perovskite electrode reported by Irvine and colleagues.^[67]

The use of Ni-perovskite (electrolyte/electrolyte + other perovskite) composite fuel electrodes not only increases the density of the TPB but also serves as structural support, providing sufficient mechanical strength to the entire cell. This fuel

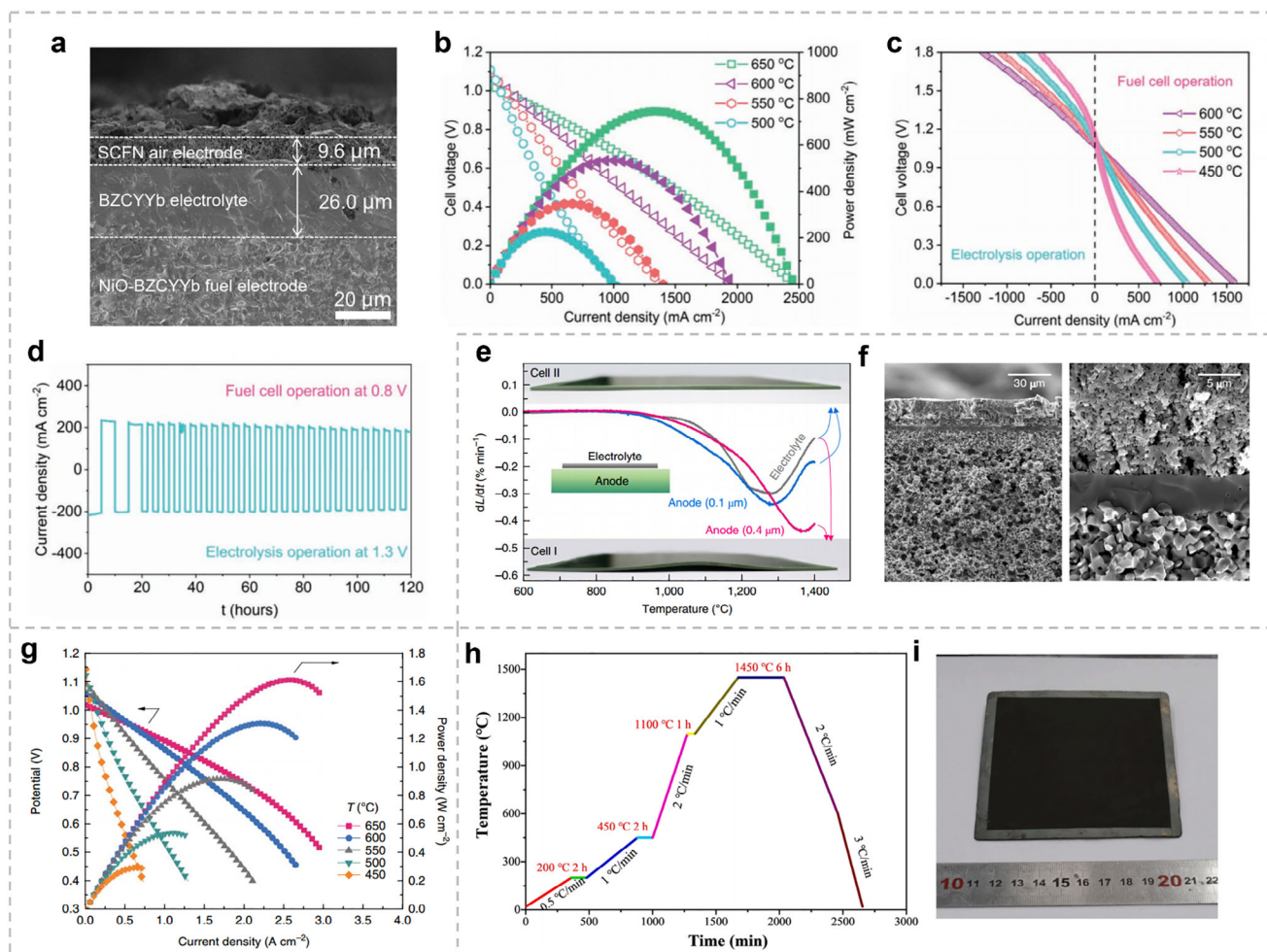


Figure 7. a) Cross-sectional SEM image of a NiO-BZCYYb fuel electrode-supported single cell with SCFN composite electrode. b) I–V and I–P curves of the Ni-BZCYYb fuel electrode-supported cell in H_2 fuel at 500–650 °C. c) I–V curves of the Ni-BZCYYb fuel electrode-supported cell measured in electrolysis mode in H_2 fuel at 450–600 °C. d) Continuous RePCC operation, cycling between electrolysis and fuel cell mode at 550 °C. e) Fabrication of flat PCFC cell with a dense electrolyte 5 μm thick. f) The microstructure of a single cell composed of a BSCF electrode. g) Potential and power density curves as functions of the current density under humidified H_2 as the fuel and dry air as the oxidant. h) Temperature program for the scale-up of a cell consisting of NiO-BZCYYb and i) $10 \times 10 \text{ cm}^2$ cell after sintering. (a–d) Reproduced with permission.^[70] Copyright 2021, John Wiley and Sons. (e–g) Reproduced with permission.^[71] Copyright 2018, Springer Nature. (h–i) Reproduced with permission.^[72] Copyright 2023, Elsevier.

electrode-supported configuration allows for thin and dense electrolyte layers to be fabricated which enhances PCEC performance.^[68] During hydrogen production via water electrolysis, Bi et al.^[69] reported that a PCEC with a Ni-BZCYYb composite fuel electrode, with 10 wt.% pore-forming agents, achieved a peak power density of 540.7 mW cm^{-2} in FC mode and a high current density of -2.28 A cm^{-2} in EC mode, at 1.3 V and 700 °C. The cell also demonstrated excellent durability, maintaining good performance for over 100 h. Song et al.^[70] fabricated a single cell supported by a NiO-BZCYYb composite fuel electrode as shown in **Figure 7a**. They revealed that the cell achieved peak power densities of 745, 531, 347, and 225 mW cm^{-2} at 650, 600, 550, and 500 °C, respectively, in FC mode, alongside excellent operational stability for over 290 h with no detectable degradation (Figure 7b). As shown in Figure 7c–d, the current densities in EC mode at 1.3 V were reported to be -364 , -269 , -179 , and -91 mA cm^{-2} at 600, 550, 500, and 450 °C, respectively. Cycling between 1.3 V

(EC mode) and 0.8 V (FC mode) at 550 °C for 27 reversible cycles (120 h) also revealed negligible performance degradation. Similarly, a PCEC fabricated rapidly sintered Ni-BZCYYb composite fuel electrodes exhibited outstanding electrochemical performance due to its high heating rate ($\approx 50 \text{ °C min}^{-1}$), which effectively inhibited cation diffusion and grain growth, resulting in a nanostructured fuel electrode. Ultimately at 600 °C, the cell achieved a maximum power density of 0.85 W cm^{-2} in FC mode and a maximum current density of 1.88 A cm^{-2} in EC mode.

Furthermore, Ni-electrolyte composite electrodes provide adequate strength as fuel electrode support material with high performance, making them a promising approach for fabricating large-scale full cells. Notably, An et al.^[71] achieved an ASR of $0.09 \Omega \text{ cm}^2$ at 600 °C and a peak power output of 20.8 W from a single $5 \times 5 \text{ cm}^2$ PCEC (Figure 7e,f), fabricated using a NiO and $\text{BaCe}_{0.55}\text{Zr}_{0.3}\text{Y}_{0.15}\text{O}_{3-\delta}$ (BCZY3) composite fuel electrode as a support. Moreover, the PPDs are significantly high,

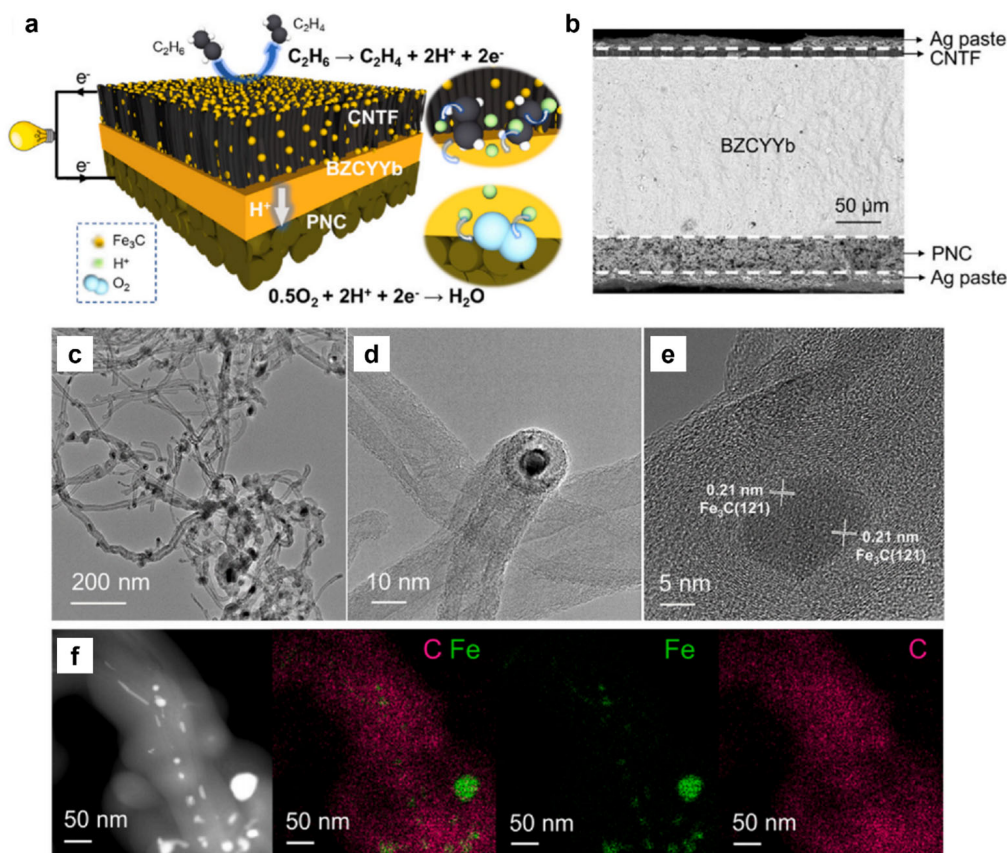


Figure 8. Structure and morphology of CNTF fuel electrode on BZCYYb electrolyte. a) Schematic of the electrolyte supporting ethane-fueled PCEC with CNTF fuel electrode. b) A typical cross-sectional SEM image of the electrolyte-supported single cell including the CNTF fuel electrode, PNC electrode, and the dense BZCYYb electrolyte. c–e) Low- and high-magnification TEM images of the CNTs sampled from CNTF electrode. f) High-angle annular dark-field (HAADF) STEM image of an individual CNT and the corresponding EDS mapping of the C and Fe elements in the CNTs. (a–f) Reproduced with permission.^[20] Copyright 2022, Elsevier.

reaching 1.302 W cm⁻² at 600 °C and 0.535 W cm⁻² at 500 °C, as shown in Figure 7g. At 550 °C, under a constant current density of 0.5 A cm⁻² (0.95 V, 0.475 W cm⁻²), the cell also exhibited negligible microstructural changes with only slight degradation over 80 h. Interestingly, this slight degradation was attributed to the increased polarization in the BSCF air electrode, rather than the degradation of the fuel electrode. Two key factors could have contributed to this BSCF degradation: Cr poisoning from the metal interconnector, which contaminates the BSCF surface, and the instability of the BSCF electrode when exposed to humid conditions. This finding offers valuable insights into future PCEC development and strongly supports the effectiveness of Ni-electrolyte composite fuel electrodes for large-size ceramic cells. Similarly, Huang et al.^[72] successfully fabricated a large 10 × 10 cm² single cell using a Ni-BZCYYb composite fuel electrode as the support shown in Figure 7h–i. The cell, fueled by hydrogen, achieved a maximum power density of 400 mW cm⁻² at 700 °C. Moreover, it demonstrated excellent performance and durability during a 425-h thermal cycling test. Marrony et al.^[73] employed a Ni-BaCe_{0.8}Zr_{0.1}Y_{0.1}O_{3-δ} (BZCY8) composite as the fuel electrode support, successfully fabricating a 20 cm² single cell. At 600 °C, this cell reached a peak power density of 0.15 W cm⁻², maintaining stability over several hours without significant

degradation. Overall, these efforts highlight the promising potential of Ni-electrolyte composite electrodes as fuel electrode supports to use in large-area PCECs, offering valuable insights into the commercial-scale production of large-area protonic PCFCs as well.

4.3. Non-Perovskite Materials

Traditional perovskite-based fuel electrode materials in PCECs are often limited by their low active surface area and propensity for coking. Hence, functional materials such as carbon nanotubes (CNTs), nanofibers, and graphene have emerged as ideal choices for various electrochemical applications due to their excellent mass/charge transport, electrical/thermal conductivity, and mechanical/chemical stability. Ding et al.^[20] reported a novel fuel electrode design for PCECs by growing aligned carbon nanotube forests (CNTF) on the BaZr_{0.4}Ce_{0.4}Y_{0.1}Yb_{0.1}O_{3-δ} (BZCYYb4411) electrolyte, using chemical vapor deposition (CVD) (Figure 8a,b). During the CVD process, highly dispersed iron carbide nanoparticles are formed in situ on the CNTF, acting as highly active catalysts. As shown in Figure 8c–f, the multi-walled CNTs exhibit a morphology with an outer diameter

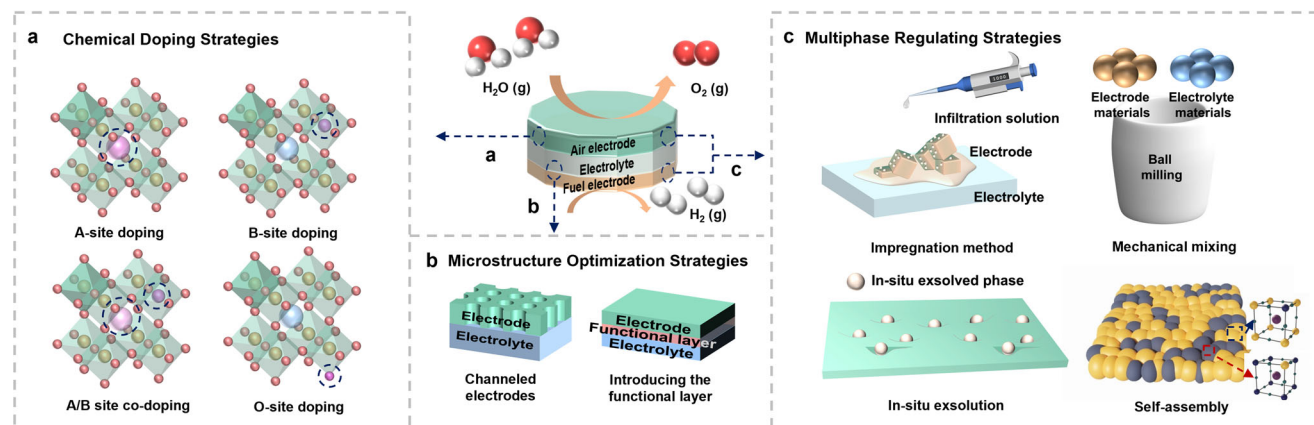


Figure 9. Schematic diagram of different regulation strategies for PCEC electrodes.

under 30 nm, and Fe nanoparticles primarily consisting of overlapping onion-like carbon shells. This new PCEC outperformed traditional perovskite-based fuel electrodes, achieving a peak power density of 0.137 W cm^{-2} at 700°C and demonstrating excellent durability and coking resistance during a 100-h test.

While optimizing the fuel electrode in proton-conducting ceramic cells can enhance PCEC performance, developing effective non-nickel-based fuel electrodes remains a significant challenge in advancing PCEC technology. Non-nickel-based fuel electrodes face limitations under reductive conditions, particularly low conductivity and chemical incompatibility, resulting in substantially lower power densities compared to nickel-metal ceramic fuel electrodes.^[67] Despite their potential, these perovskite oxide fuel electrodes still require considerable improvement before practical application.

5. Regulation Strategies of PCEC Electrode Materials for Water Electrolysis

In Sections 3 and 4, we have compared and summarized the crystal structures, conductive properties (electronic and ionic conductivity), thermal expansion coefficients, surface oxygen exchange coefficients, and other material properties that significantly influence the performance of PCEC fuel electrode and air electrode materials. Despite several electrode materials demonstrating excellent electrocatalytic activity and stability in PCECs, numerous issues remain unresolved, for instance, metal migration and agglomeration in cermet fuel electrode materials,^[74] poor electronic conductivity in perovskite-type electrode materials,^[75] and mismatched thermal expansion coefficients between air electrode materials and electrolytes.^[76] These challenges necessitate design strategies that optimize and regulate the electrode material properties. To enhance the performance of PCEC air electrode and fuel electrode materials, ionic and electrical conductivity, chemical stability, and thermal expansion need to be addressed. In this section, we will thoroughly examine three principal approaches to address these limitations: chemical doping, microstructural engineering, and multiphase design strategies, as illustrated in Figure 9.

5.1. Chemical Doping

Perovskite oxides, the most widely used materials for PCEC electrodes, are characterized by their stable crystal structure and exceptional versatility in elemental substitutions at the A, B, and O sites. This allows for the electrodes to be modified by a wide range of elements. Doping solid solutions with multiple elements thereby enhances their ionic conductivity, electronic conductivity, and catalytic activity.

5.1.1. A-Site Doping

In perovskite oxides, the A sites are generally occupied by larger cations, such as alkaline earth metals (e.g., calcium, strontium) or rare earth metals (e.g., lanthanum). These cations are positioned at the vertices of the perovskite unit cell and are coordinated by twelve oxygen anions. By doping elements with lower electronegativity at the A site, the electron density at the oxygen sites in the M–O bonds will increase. Enhancing electron density will result in higher basicity, making the hydration enthalpy more negative, which is favorable for proton conductivity. For instance, Xu et al.^[77] selected monovalent alkali metals with high basicity as doping elements. They examined the effects of replacing Ba ions with K ions on two types of oxygen vacancies within the BSCF and $\text{Ba}_{0.4}\text{K}_{0.1}\text{Sr}_{0.5}\text{Co}_{0.8}\text{Fe}_{0.2}\text{O}_{3-\delta}$ (BKSCF) lattices, focusing on oxygen vacancy formation energy and hydration energy. Their results showed that BKSCF demonstrates superior oxygen vacancy formation and exhibits a more negative hydration enthalpy compared to BSCF (Figure 10a), leading to reduced polarization resistance, which thereby enhances proton migration and catalytic activity (Figure 10b). Similarly, Park et al.^[78] introduced monovalent alkali metals with high basicity into $\text{BaCo}_{0.4}\text{Fe}_{0.4}\text{Zr}_{0.18}\text{Y}_{0.02}\text{O}_{3-\delta}$, facilitating the exsolution of barium oxides under humidified air conditions. It was conveyed that BaO_x -exsolved $\text{K}_{0.05}\text{Ba}_{0.95}\text{Co}_{0.4}\text{Fe}_{0.4}\text{Zr}_{0.18}\text{Y}_{0.02}\text{O}_{3-\delta}$ (KBCFZY) exhibits the lowest ASR compared to other oxygen electrode perovskites. Density Functional Theory (DFT) calculations of proton mobility energetics in $\text{BaCo}_{0.4}\text{Fe}_{0.4}\text{Zr}_{0.18}\text{Y}_{0.02}\text{O}_{3-\delta}$ and KBCFZY further demonstrated that K^+ doping reduces the overall migration energy, enhancing proton mobility (Figure 10c). Both

studies demonstrate that substituting Ba with K at the A-site enhances the proton conductivity of the material, which improves catalytic activity. Additionally, replacing A-site metal atoms like Sr with elements of a relatively smaller ionic radius, such as Ca, can increase the yield of hydrogen production at the fuel electrode in SOEC mode. Mahata et al.^[79] demonstrated this as they discovered that partially or fully substituting Sr with Ca in $\text{La}_{0.65}\text{Sr}_{0.30}\text{MnO}_3$ enhances their electrical conductivity, catalytic activity, and electrolyte compatibility. Specifically, electrical conductivity increased with higher Ca content in samples where Sr was completely replaced by Ca. Furthermore, compared to $\text{La}_{0.65}\text{Sr}_{0.30}\text{MnO}_3$, both $\text{La}_{(1-x)}\text{Ca}_x\text{MnO}_3$ (LCM) and $\text{La}_{0.65}\text{Sr}_y\text{Ca}_{(0.3-y)}\text{MnO}_3$ (LSCM) exhibited overall higher hydrogen production and barely reacted to increasing temperature.

Another significant type of perovskite oxides are RP phase perovskites. They exhibit a unique layered structure consisting of alternating ABO_3 perovskite layers and AO rock salt layers. This configuration endows the RP phase with excellent electronic and oxygen conductivities. Recently, studies at both the microscopic conduction site simulation level and the macroscopic conducting rail testing level have demonstrated that doping alkaline elements at the A-site of the pristine RP phase increases hydration, which was found to be directly proportional to both the dopant concentration and its basicity. Zhong et al.^[80] discovered that $\text{La}_2\text{NiO}_{4+\delta}$ contains oxygen interstitials, which would facilitate the localization and migration of protons. Through theoretical calculations, they simulated the proton conduction pathways via oxygen interstitials (Figure 10d). Hebb–Wagner polarization tests indicated that doping alkaline elements at the A-site increases protonic conductivity, with Sr content in $\text{La}_{2-x}\text{Sr}_x\text{NiO}_{4+\delta}$ (LSN) samples showing a positive correlation (Figure 10e). Besides, Li et al.^[81] investigated the $\text{Pr}_2\text{NiO}_{4+\delta}$, manipulating its conductivities by substituting Ba at the Pr-site to explore the relationship

between conductivity types and reaction kinetics. By optimizing Ba content for balanced proton conductivity and oxygen surface desorption capabilities, they found that $\text{Pr}_{1.7}\text{Ba}_{0.3}\text{NiO}_{4+\delta}$ exhibits the best performance at 700 °C, with a reaction resistance of $0.022 \Omega \text{ cm}^2$ and a current density of 1.96 A cm^{-2} .

Apart from doping into the A-site with alkaline elements, constructing deficiencies in the A-site can also efficiently enhance proton uptake and conduction. This approach creates additional oxygen vacancies that significantly improve the ionic conductivity and catalytic activity of the perovskites, which consequently exhibit higher current densities and lower overpotentials. For instance, Ren et al.^[82] developed A-site-deficient perovskite oxides, specifically $\text{Ba}_x\text{Co}_{0.4}\text{Fe}_{0.4}\text{Zr}_{0.1}\text{Y}_{0.1}\text{O}_{3-\delta}$ ($x = 1, 0.95, 0.9$) (B_xCFZY), by altering the charge-compensation mechanisms. As illustrated in Figure 11a, the overall charge of the B_xCFZY system can be regulated by the formation of oxygen vacancies and the oxidation of Co(Fe)^{3+} to Co(Fe)^{4+} to maintain electrical neutrality. With increasing Ba deficiency, the O1s peak area of lattice oxygen decreases (Figure 11b), proton concentration increases (Figure 11c) and ASR decreases (Figure 11d), indicating that A-site vacancies not only facilitate the formation of oxygen vacancies but also enhance proton uptake, thereby improving ORR performance. Tang et al.^[14b] developed an A-site deficient layered perovskite, $(\text{PrBa}_{0.8}\text{Ca}_{0.2})_{0.95}\text{Co}_2\text{O}_{6-\delta}$ (PBCC95), to serve as an oxygen electrode for a PCEC. The current densities of the PBCC95 cell in EC mode significantly increase at lower temperatures of 550 °C and 500 °C compared to the PBCC reference (Figure 11e). Furthermore, the PCEC utilizing PBCC95 demonstrates excellent durability under practical operating conditions, maintaining stable performance for 160 h across both operating modes without any observable degradation (Figure 11f).

Recent advancements in high-entropy strategies to perovskite-based air electrodes for PCEC have shown significant

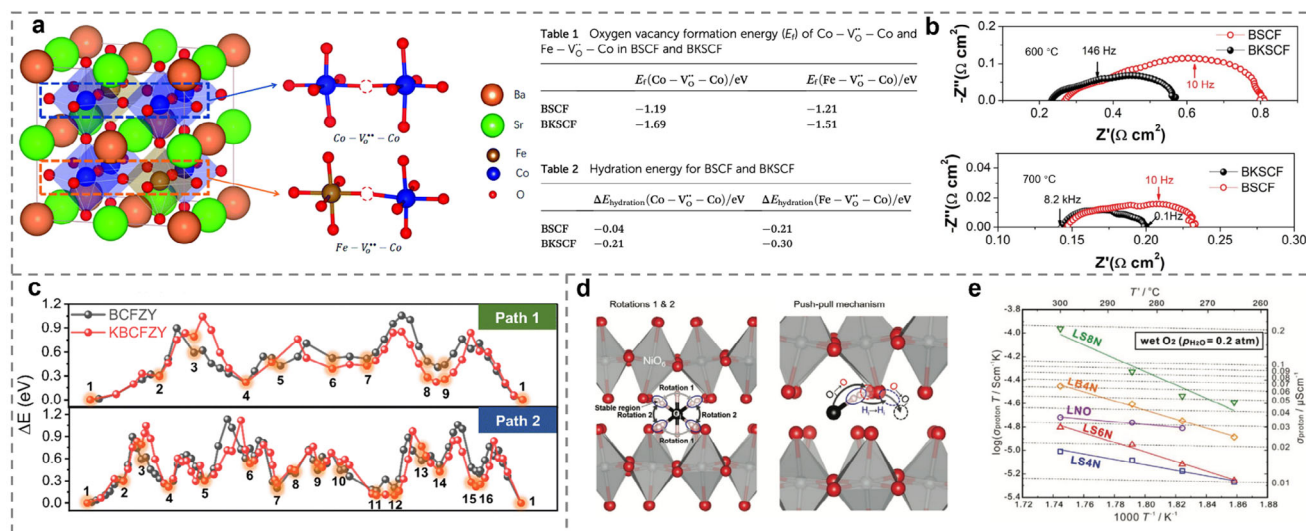


Figure 10. a) Scheme of two types of oxygen vacancies and the comparison of their oxygen vacancy formation energy and hydration energy. b) EIS plots of the cell using BSCF and BKSCF air electrodes tested at 600 and 700 °C. c) Calculated energy along the pathway relative to the energy of the most stable position. d) Three elementary processes of proton migration during the FPMD simulation for 100 ps at 1000 K in La_2NiO_4 with a proton and an interstitial O ion. e) Arrhenius plot of measured proton conductivity of LNO, LS4N, LS6N, LS8N, and LB4N in wet O_2 . (a,b) Reproduced with permission.^[77] Copyright 2019, Royal Society of Chemistry. (c) Reproduced with permission.^[78] Copyright 2024, Royal Society of Chemistry. (d,e) Reproduced with permission.^[80] Copyright 2022, John Wiley and Sons.

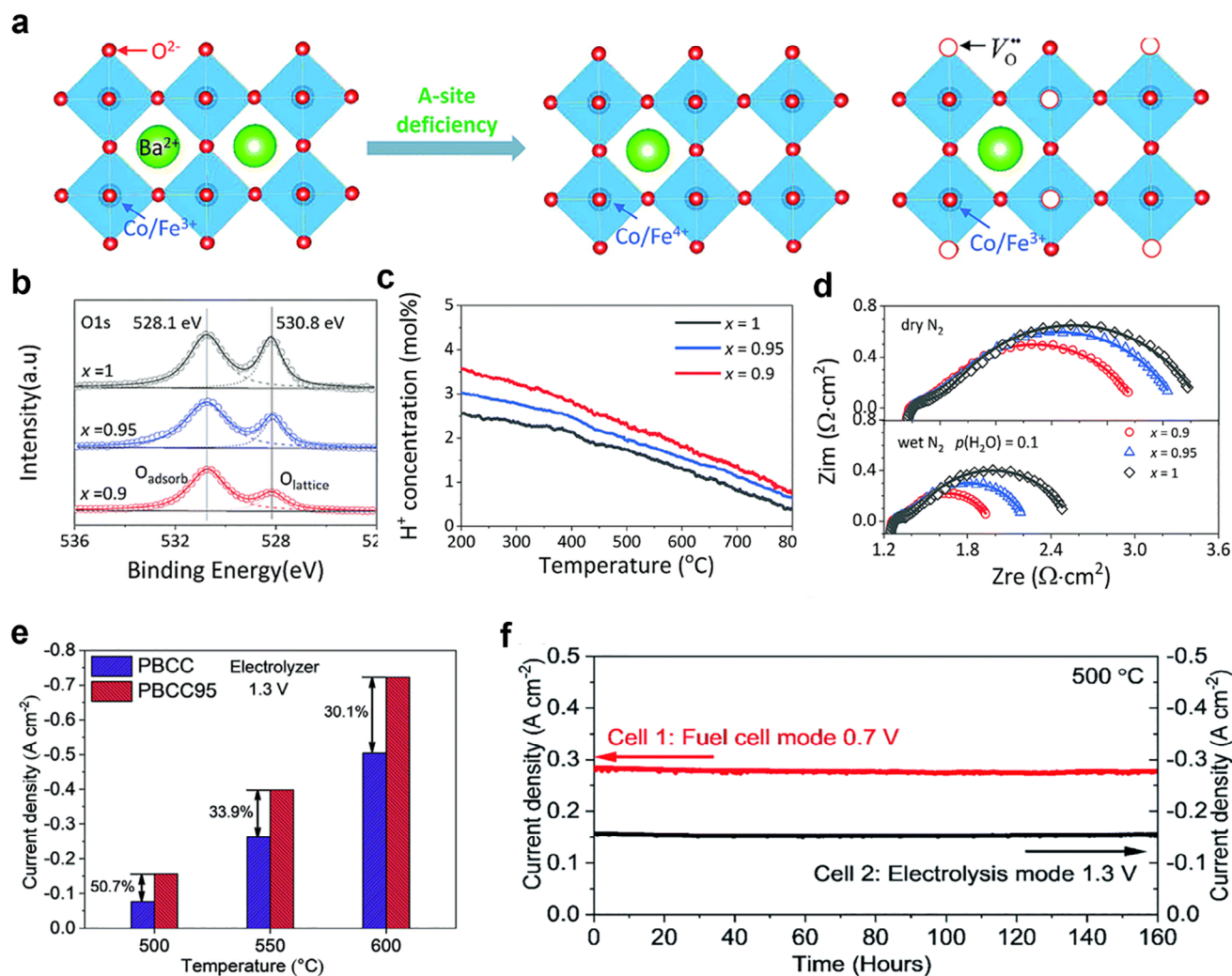


Figure 11. a) Schematic illustration of the charge-compensation mechanisms. b) XPS spectra of O 1s peaks. c) The calculated proton concentration at different temperatures. d) EIS recorded at 550 $^\circ\text{C}$ in dry and wet N_2 . e) Electrolysis current density comparison of PBCC95 and PBCC at 1.3 V. f) Long-term stability testing of the cell in fuel cell mode at 0.7 V and in electrolysis mode at 1.3 V and 500 $^\circ\text{C}$. (a–d) Reproduced with permission.^[82] Copyright 2019, Royal Society of Chemistry. (e, f) Reproduced with permission.^[14b] Copyright 2020, Royal Society of Chemistry.

improvements in structural tolerance and thermal compatibility under harsh humidified conditions, while simultaneously maintaining high catalytic activity. Typically, a high-entropy single-phase structure is achieved by incorporating multiple different cations (≥ 5 elements) into the same crystallographic site (either the A site or B site) of perovskite oxides. This multi-component design not only enhances configurational entropy but also creates lattice distortion and disordered stress fields around mobile cations (e.g., Sr), which kinetically impede their segregation by reducing ionic migration rates, as evidenced by atomic-scale studies of high-entropy $\text{La}_{0.2}\text{Pr}_{0.2}\text{Nd}_{0.2}\text{Sm}_{0.2}\text{Sr}_{0.2}\text{MnO}_{3-\delta}$ cathodes under thermal stress.^[83] Besides, He et al.^[84] designed a high-entropy $\text{Pr}_{0.2}\text{Ba}_{0.2}\text{Sr}_{0.2}\text{La}_{0.2}\text{Ca}_{0.2}\text{CoO}_{3-\delta}$ (HE-PBSLCC) compound, leveraging the excellent conductivity and favorable thermal expansion coefficients of Or-based perovskite oxides. The substitution of La^{3+} , which has a larger ionic radius, for Sr^{2+} was intended to reduce the B–O bond strength, while the inclusion of Ca^{2+} was chosen for its stable chemical prop-

erties and cost-effectiveness. The successful synthesis of the PBSLCC electrode is further validated by the uniform distribution of Pr, Ba, Sr, La, Ca, and Co elements at the nanoscale, as evidenced by X-ray energy dispersive spectroscopy (EDS) (Figure 12a). When utilized as the air electrode in PCEC, HE-PBSLCC exhibits enhanced electrochemical activity and superior structural stability, achieving a current density of -2.68 A cm^{-2} at 1.3 V, along with robust operational durability over 500 h. Similarly, Liu et al.^[85] has developed a high-entropy perovskite oxide comprising six equimolar metals at the A-site, specifically $\text{Pr}_{1/6}\text{La}_{1/6}\text{Nd}_{1/6}\text{Ba}_{1/6}\text{Sr}_{1/6}\text{Ca}_{1/6}\text{CoO}_{3-\delta}$ (PLNBSCC). A PCEC employing this PLNBSCC air electrode is able to achieve an impressive current density of -1.95 A cm^{-2} at an electrolysis voltage of 1.3 V and a temperature of 600 $^\circ\text{C}$, which is remarkable. Instead of doping multiple elements at the A-site to construct high-entropy single-phase perovskites, He et al.^[86] introduced a novel composite material, $\text{Ce}_{0.2}\text{Ba}_{0.2}\text{Sr}_{0.2}\text{La}_{0.2}\text{Ca}_{0.2}\text{CoO}_{3-\delta}$ (CBSLCC), which spontaneously

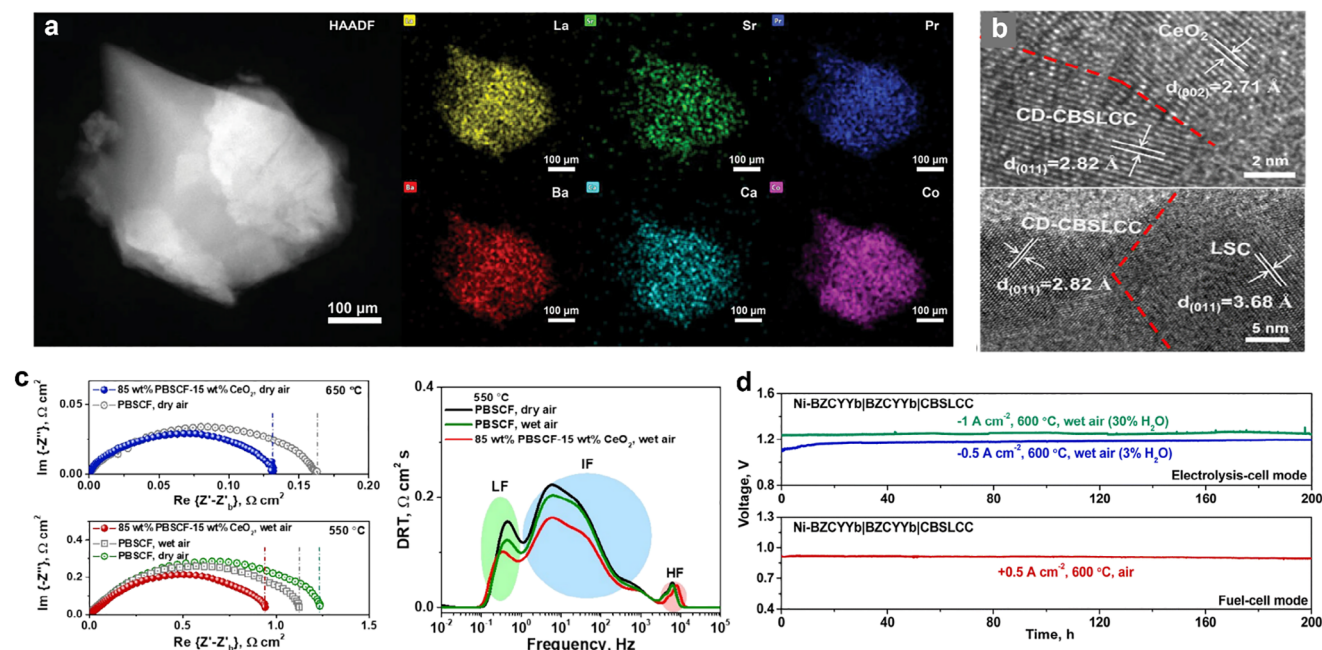


Figure 12. a) High-angle annular dark-field STEM image and the X-ray EDS mapping of Pr, Ba, Sr, La, Ca, and Co from the HE-PBSLCC grain. b) HRTEM images of the CD-CBSLCC, CeO₂, and LSC interfaces in the selected CBSLCC composites. c) EIS of PBSCF and 85 wt% PBSCF-15 wt% CeO₂ electrodes measured in dry air at 650 °C and 550 °C and DRT analysis on the corresponding EIS. d) Stability of the single cells in EC (top) and FC (bottom) modes under different conditions. (a) Reproduced with permission.^[84] Copyright 2023, John Wiley and Sons. (b–d) Reproduced with permission.^[86] Copyright 2024, Royal Society of Chemistry.

self-assembles into three-phase electrocatalysts with deficient Ce_{0.2–y}Ba_{0.2}Sr_{0.2–x}La_{0.2–x}Ca_{0.2}CoO_{3–δ} (CD-CBSLCC), CeO₂, and La_{0.5}Sr_{0.5}CoO_{3–δ}. This three-phase structure was confirmed using high-resolution TEM (HRTEM) images (Figure 12b). The CeO₂ phase provides and consumes protons, facilitating oxygen evolution and reduction kinetics in reversible protonic ceramic electrochemical cells (R-PCECs). Moreover, electrochemical impedance spectroscopy (EIS) and distribution of relaxation times (DRT) analyses demonstrate that the CeO₂ phase acts as a hydrating and ionic-conducting secondary phase, optimizing mass and gas transfer processes on the composite electrode surface at 550 °C in humid air (Figure 12c). Single-cell durability testing based on the self-architected CBSLCC composite air electrode revealed exceptional robustness and long-term viability, with no noticeable voltage degradation over 200 h in both electrolysis-cell and fuel-cell modes (Figure 12d).

5.1.2. B-Site Doping

In perovskite oxides, the B-site occupies six-fold coordination within the oxygen octahedra and typically serves as the active site for various electrochemical reactions. By doping the B-site with rare earth or transition metals, the coordination environment of the M–O bond in the B-site can be altered. This allows for enhanced control over key processes such as electron transport, oxygen migration, and proton conduction during high-temperature water electrolysis. A common approach involves doping with low-valence cations such as Ni²⁺/Ni³⁺, Fe²⁺/Fe³⁺, Mg²⁺, Zn²⁺, and Sc³⁺, which possess suitable ionic radii for B-site doping and can

adjust the metal to a lower oxidation state, promoting the formation of oxygen vacancies. This in turn enhances the ORR activity, proton and oxygen ion conductivities, and surface exchange processes.^[87] Doping the B-site with an appropriate amount of Ni is a commonly used effective approach to enhance the electrocatalytic activity of the air electrode in PCEC across various perovskite material systems. For example, Li et al.^[88] reported that substituting Fe with Ni in Ba_{0.5}Sr_{0.5}Co_{0.7}Fe_{0.2}Ni_{0.1}O_{3–δ} (BSCFN) results in a cubic structure with a high density of oxygen vacancies, facilitating rapid oxygen binding and diffusion kinetics in oxygen ion conductors. In addition, Park et al.^[89] investigated the impact of doping Ni contents on the performance of NdBa_{0.5}Sr_{0.5}Co_{1.5}Fe_{0.5}O_{5+δ} double perovskite as an air electrode for PCEC, in which 5 mol% Ni doping notably enhances the activity of oxygen electrodes in humidified air. Furthermore, substituting Co with Ni at the B-site of La_{0.8}Sr_{0.2}CoO_{3–δ} improves the hydration capacity due to the large negative hydration enthalpy that thereby reduces polarization resistance, as demonstrated in La_{0.8}Sr_{0.2}Co_{0.7}Ni_{0.3}O_{3–δ}.^[13a] Di et al.^[13b] showed that Ni substitution at the B-sites of PrCoO₃, another commonly used oxygen electrode in oxygen-ion conducting fuel cells, lowers the migration barrier for proton conduction when proton defects are readily introduced via hydration reactions. The authors employed DFT calculations to simulate two representative proton transfer pathways during hydration reactions: inter-octahedral hopping and intra-octahedral hopping. The computational results revealed that, regardless of the pathway, Ni doping facilitates proton transport through the bulk material (Figure 13a).

Besides Ni, other types of low valence transition metal element such as Fe, Zn, Mg, and Sc can be doped at B-site in

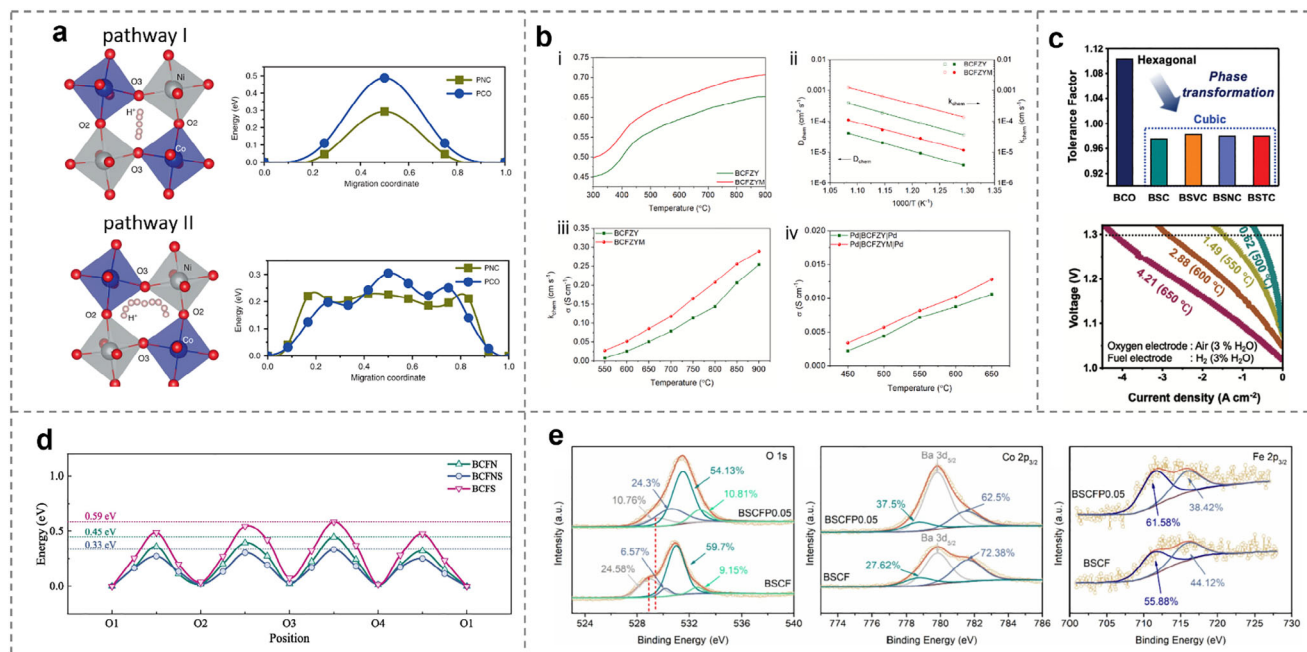


Figure 13. a) Minimum energy paths for proton migration along pathway I (inter-octahedral hopping) and II (intra-octahedral hopping) in bulk PNC and PNO. b) Oxygen non-stoichiometries curves i), the fitted D_{chem} and k_{chem} ii), oxygen-ion conductivity iii), and proton conductivity iv) of BCFZY and BCFZYM. c) Tolerance factors of BSC and BMM'C, I–V curves of the BSTC (PLD) cell in EC mode. d) Minimum-energy paths of proton diffusion along the intra-octahedron direction. e) XPS spectra for O 1s, Co 2p_{3/2}, Fe 2p_{3/2} of BSCFP0.05 and BSCF powders. (a) Reproduced under the terms of the CC-BY Creative Commons Attribution 4.0 International license.^[13b] Copyright 2020, The Authors, published by Springer Nature. (b) Reproduced with permission.^[34] Copyright 2022, Elsevier. (c) Reproduced with permission.^[93] Copyright 2024, John Wiley and Sons. (d) Reproduced with permission.^[94] Copyright 2023, Elsevier. (e) Reproduced with permission.^[95] Copyright 2022, Elsevier.

perovskites to enhance the overall performance of air electrodes in water electrolysis. For instance, Zhu et al.^[90] found that doping Fe into PNC to form $\text{PrNi}_{0.4}\text{Co}_{0.4}\text{Fe}_{0.2}\text{O}_{3-\delta}$ (PNCf) reduced the TEC from 19.2×10^{-6} to $17.4 \times 10^{-6} \text{ K}^{-1}$. In terms of Zn, Yang et al.^[15b] showed that $\text{Pr}_{1.8}\text{Ba}_{0.2}\text{Ni}_{0.9}\text{Zn}_{0.1}\text{O}_{4+\delta}$ (PBNZ1), which was doped at the B-site of $\text{Pr}_{1.8}\text{Ba}_{0.2}\text{NiO}_{4+\delta}$ (PBN), significantly enhances the electrolysis performance; under operating conditions of 700 °C and 1.3 V, the PBNZ1 composition achieved a current density of 2.95 A cm^{-2} , representing a 30% improvement over the undoped PBN electrode. Moreover, Cheng et al.^[91] explored the Zn-doping effect on $\text{Sr}_2\text{Fe}_{1.5}\text{Mo}_{0.5}\text{O}_{6-\delta}$ (SFM), which is commonly employed as a fuel electrode in high-temperature CO_2 electrolysis or as an anode in PCEC for water electrolysis. After doping with Zn, the current density of $\text{Sr}_2\text{Fe}_{1.4}\text{Zn}_{0.1}\text{Mo}_{0.5}\text{O}_{6-\delta}$ (SFZM) nearly doubled compared to SFM in a single-cell EC mode. Despite the fact that the ionic radius of Mg is typically considered too large for effective B-site doping in many perovskite oxides, Liang et al.^[34] successfully synthesized a phase-pure triple conducting perovskite by doping a small amount (5%) of Mg into the BCFZY lattice. The resulting Mg-doped perovskite, $\text{Ba}(\text{Co}_{0.4}\text{Fe}_{0.4}\text{Zr}_{0.1}\text{Y}_{0.1})_{0.95}\text{Mg}_{0.05}\text{O}_{3-\delta}$ (BCFZYM), demonstrated enhanced oxygen ion and proton conductivities, as well as an improved proton uptake capability compared to the pristine BCFZY (Figure 13b). Finally, Wang et al.^[92] explored substituting Ce with Sc, which has a smaller ionic radius, in $\text{BaFe}_{0.6}\text{Ce}_{0.4}\text{O}_{3-\delta}$ (BFC) to enhance the structural stability and mechanical compatibility. Doping of Sc optimizes Fe 3d- e_g orbital occupancy and increases oxygen vacancies in $\text{BaFe}_{0.6}\text{Ce}_{0.2}\text{Sc}_{0.2}\text{O}_{3-\delta}$ (BFCS), re-

sulting in a significantly lower ASR of $\approx 0.175 \Omega \text{ cm}^2$ at 600 °C in symmetrical cells, which is ca. 1/3 of that in the undoped BFC electrode.

Co-doping with both low-valence and high-valence metals at the B-site of perovskites can significantly enhance their electrocatalytic activity. Incorporating high-valence cations stabilizes the perovskite structure whilst low-valence metals reduce the pristine metal's oxidation state, increasing oxygen vacancies and improving ionic conductivity. Kim et al.^[93] found that dual metal doping in $\text{BaCoO}_{3-\delta}$ (BCO) inhibits the formation of a hexagonal perovskite, rather than converting the undoped electrode it into a cubic perovskite structure that enhances water uptake and hydration capabilities. Among the various doped compositions, $\text{BaSc}_{0.1}\text{Ta}_{0.1}\text{Co}_{0.8}\text{O}_{3-\delta}$ (BSTC) exhibited the best performance. The Sc-Ta pair doping facilitated a 3D proton diffusion pathway within the BCO lattice (Figure 13c), achieving a current density of 4.21 A cm^{-2} at 650 °C in the EC mode. Lu et al.^[94] also employed co-doping with Nb^{5+} and Sc^{3+} to enhance the hydration capability of BCO-based air electrodes. As illustrated in Figure 13d, the minimum energy path (MEP) calculations for proton diffusion reveal that the most considerable migration barriers for $\text{BaCo}_{0.4}\text{Fe}_{0.4}\text{Nb}_{0.2}\text{O}_{3-\delta}$, $\text{BaCo}_{0.4}\text{Fe}_{0.4}\text{Nb}_{0.1}\text{Sc}_{0.1}\text{O}_{3-\delta}$ (BCFNS), and $\text{BaCo}_{0.4}\text{Fe}_{0.4}\text{Sc}_{0.2}\text{O}_{3-\delta}$ (BCFS) are 0.45, 0.33, and 0.59 eV, respectively. The relatively low proton transfer energy barrier in BCFNS suggests enhanced proton conductivity, likely to enhance the performance of devices utilizing BCFNS oxygen electrodes.

Beyond rare-earth elements and transition metals, doping non-metal dopants at B-sites are also an option for modification.

For instance, Liu et al.^[95] synthesized a novel oxygen electrode, $\text{Ba}_{0.5}\text{Sr}_{0.5}(\text{Co}_{0.8}\text{Fe}_{0.2})_{0.95}\text{P}_{0.05}\text{O}_{3-\delta}$ (BSCFP_{0.05}), by partially incorporating the non-metallic element phosphorus (P) into BSCF. The introduction of P modified the electronic structure of surface Co and Fe ions, enhancing the surface oxygen exchange and bulk diffusion capabilities of BSCF. This improvement is attributed to the higher electronegativity of P (2.1) compared to Co (1.9) and Fe (1.8), which weakens the binding force of oxygen ions to Co and Fe. Consequently, this facilitates the migration of oxygen ions and the bulk diffusion of the hydrated product OH^- , which is evidenced by the intensified peaks at 531.5 eV, corresponding to surface-adsorbed oxygen (O_2/OH^-) (Figure 13e).

5.1.3. A/B Site Co-Doping

Introducing metals, particularly alkaline earth metals, into the A-site helps increase oxygen vacancies, thus enhancing oxide ion conductivity. In contrast, modifications at the B-site of BO_6 octahedra affect electrochemical reactions, influencing magnetic and electrical properties. By selecting elements for co-substitution at both A and B sites, it is possible to simultaneously optimize oxygen transport, electron conduction, and proton conductivity. For instance, Taylor et al.^[96] investigated the impact of co-doping LaFeO_3 with various divalent dopants at both A- and B-sites on its mixed ionic-electronic conductivity, which enhances the formation of both oxygen vacancies and electronic holes within the system (Figure 14a). Choi et al.^[97] reported that co-doping Sr at the A-site and Fe at the B-site in cation-ordered double perovskite materials, such as $\text{PrBa}_{0.5}\text{Sr}_{0.5}\text{Co}_{2-x}\text{Fe}_x\text{O}_{5+\delta}$, results in improvements in both oxygen ion diffusion and surface oxygen exchange rates. The ordered stacking sequence, specifically $[\text{Ba}(\text{Sr})\text{O}]-[\text{Co}(\text{Fe})\text{O}_2]-[\text{PrO}_\delta]-[\text{Co}(\text{Fe})\text{O}_2]-[\text{Ba}(\text{Sr})\text{O}_2]$, is confirmed by the HRTEM (Figure 14b). Compared to materials without Fe, incorporating up to 50% of Fe increases the concentration of mobile oxygen defects in the Ln–O layers, facilitating faster oxygen kinetics and enhanced electrochemical performance. Fuel cells based on these air electrodes exhibited maximum power densities of 710 and 2200 mW cm^{-2} at 500 and 600 °C, respectively (Figure 14c).

In addition to co-doping strategies, enhancing the electrochemical activity and durability of a perovskite-type air electrode can also be achieved through A-site defects and B-site doping.^[98] Liu et al.^[98] reported that A-site deficient BCFN with Nb-deficient BCFN nanoparticles formed under steam conditions due to surface reconstruction (Figure 14d). This resulted in a peak power density of 1.70 W cm^{-2} at 650 °C in FC mode and a current density of 2.8 A cm^{-2} at 1.3 V in EC mode (Figure 14e). Similarly, Liang et al.^[99] developed $\text{Ba}_{0.95}(\text{Co}_{0.4}\text{Fe}_{0.4}\text{Zr}_{0.1}\text{Y}_{0.1})_{0.95}\text{Ni}_{0.05}\text{O}_{3-\delta}$ (BCFZYN) by combining A-site Ba deficiency and B-site Ni doping. This material comprises a predominant perovskite phase (D-BCFZYN) alongside a minor NiO phase. DFT calculations suggest that NiO nanoparticles enhance water molecule adsorption, whereas the D-BCFZYN phase facilitates oxygen desorption and proton conduction. Moreover, Ni et al.^[15a] designed a $\text{Sr}_3\text{Fe}_2\text{O}_{7-\delta}$ (SF)-based perovskite with A-site Sr deficiency and B-site Nb substitution for PCEC. Nb^{5+} doping stabilizes the crystal structure by consuming oxygen vacancies for charge compensation whilst Sr deficiency regenerates oxygen vacancies. It elevates Fe valence,

balancing bulk transport and surface reactivity (Figure 14f). This system exhibits a stable performance for ≈ 142 h at 0.8 V in PCFC mode and 109 h stability at 1.3 V in PCEC mode (Figure 14g).

5.1.4. O-Site Doping

Anionic doping, achieved by substituting lattice oxygen or occupying oxygen vacancies, effectively modulates the perovskite oxides' properties by altering charge balance, electronegativity, and band structure.^[100] For instance, F doping generates oxygen vacancies due to its high electronegativity and low negative charge, while S doping can enhance oxygen electrocatalytic activity by tuning the electronic structure of B-site transition metal elements.^[101] Despite typically accounting for only 0.1–0.2 of the oxygen stoichiometry, anion doping at the O site significantly influences various properties of perovskite oxides, including electronic and crystal structures, ionic and electronic conductivity, chemical stability, oxygen vacancy concentration, and oxygen ion mobility.^[102] Therefore, alongside A/B-site cation doping, O-site anionic doping is a promising modification method to improve perovskite oxides.

When anions are introduced into the perovskite lattice, their crystallographic regularity and stability changes. F doping can induce phase transitions in $\text{Sr}_2\text{Co}_2\text{O}_5$, transforming its hexagonal phase into a cubic phase $\text{SrCoO}_{2.85-\delta}\text{F}_{0.15}$ (SCF0.15), with the CoO_6 octahedra transitioning from a face-sharing to a corner-sharing configuration.^[103] Li et al.^[104] further confirmed this effect in their study of F-doped $\text{Pr}_{1.1}\text{Ba}_{0.9}\text{Co}_2\text{O}_{5+\delta}\text{F}_{0.1}$ ($\text{P}_{1.1}\text{BCOF}_{0.1}$), where the introduction of F^- anions induced cation ordering between Pr^{3+} and Ba^{2+} , leading to a symmetry shift from cubic/tetragonal to purely tetragonal in $\text{Pr}_{1.1}\text{Ba}_{0.9}\text{Co}_2\text{O}_{5+\delta}$ (Figure 15a). Besides, F doping enhances the lattice symmetry of a crystal structure. Specifically, in the case of $\text{Sr}_2\text{Fe}_{1.5}\text{Mo}_{0.5}\text{O}_{6-x-\delta}\text{F}_x$ (SFMF), F doping shifts the structure from an orthorhombic configuration (space group Cmmm) to a pseudo-cubic configuration (space group Pm3m), thereby enhancing the lattice symmetry of SFMF.^[105] Moreover, in a RP perovskite such as $\text{Ln}_{1.2}\text{Sr}_{1.8}\text{Mn}_2\text{O}_7\text{F}_2$ (Ln = La, Pr, Nd, Sm, Eu, Gd), F doping significantly expands the interlayer distance along the c-axis of the perovskite lattice, while notable contraction occurs along the a-b plane.^[106] Li et al.^[107] also found that fluorine-doped $\text{Pr}_2\text{NiO}_{4+\delta}$ (PNO) exhibited excellent electrochemical activity and durability as an air electrode. In symmetric cells supported by BZCYYb, $\text{Pr}_2\text{NiO}_{3.9+\delta}\text{F}_{0.1}$ (PNOF) demonstrated lower polarization resistance and activation energy compared to PNO, indicating superior kinetics at lower temperatures.

Anion doping effectively regulates the TEC of perovskites by influencing B-site ion behavior. For example, in $\text{PrBaCo}_2\text{O}_{5+\delta}$ (PBC), TEC is primarily affected by the reduction of B-site transition metal ions (Con^+) and/or chemical expansion resulting from their spin state transitions.^[108] Fluorine doping, due to its higher electronegativity compared to oxygen, inhibits electron transfer to Con^+ , suppressing their reduction and limiting oxygen vacancy formation, which reduces TEC. Similarly, anion doping enhances ionic conductivity and modulates oxygen vacancies. In $\text{BaCaNbO}_{5.5}$, both F and Cl doping improve oxygen conductivity despite variations in dopant radius and electronegativity.^[109] Likewise, changes in electron density caused by anion doping

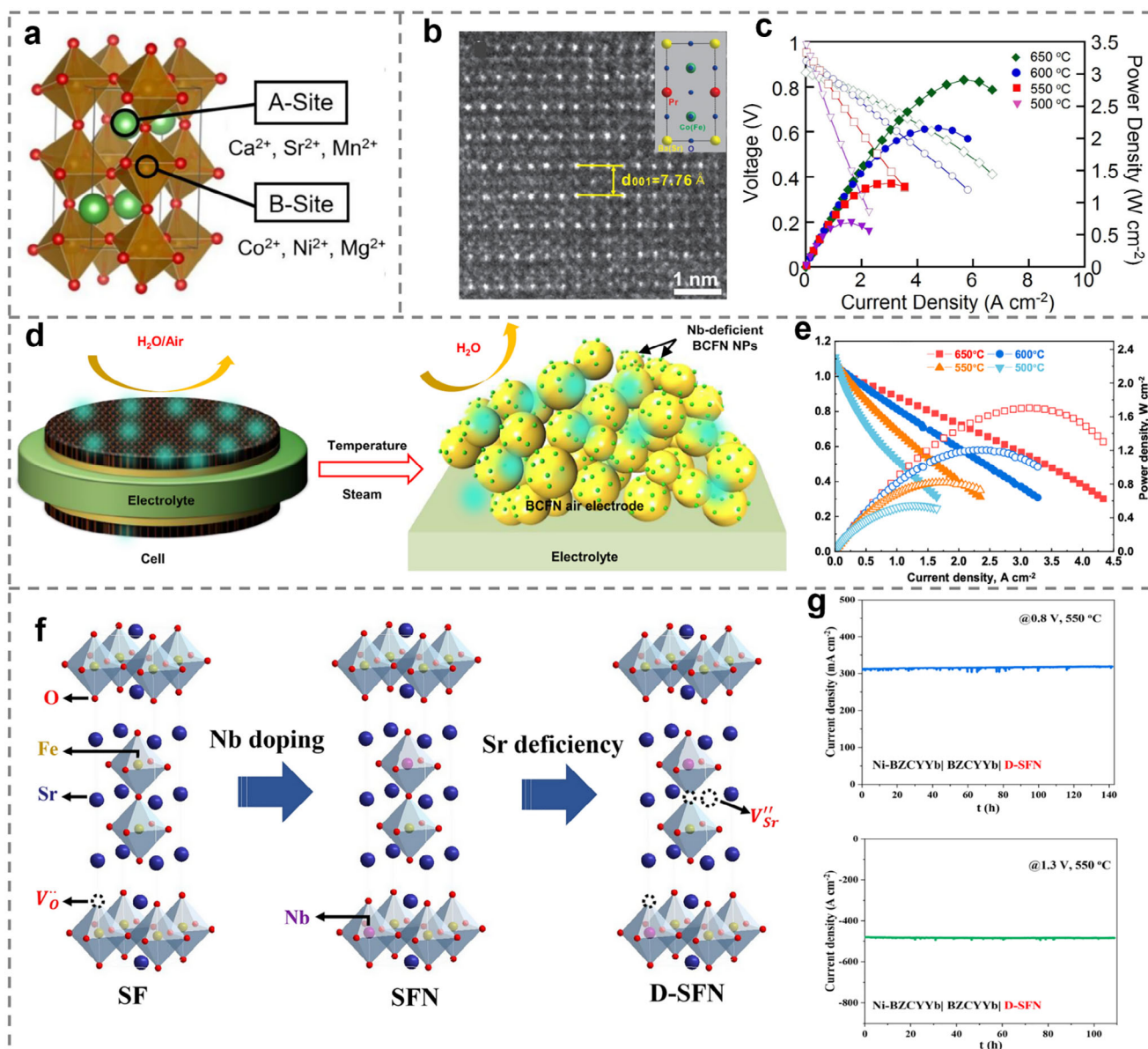


Figure 14. a) A schematic illustration of the A- and B-sites co-doping for promoting oxygen vacancies and holes. b) The TEM image of $\text{PrBa}_{0.5}\text{Sr}_{0.5}\text{Co}_{2-x}\text{Fe}_x\text{O}_{5+\delta}$ and high-resolution TEM image of its grain. c) I–V curves and the corresponding power densities of test cells. d) A schematic illustration of Nb-deficient BCFN NPs forming on the BCFN air electrode. e) Typical I–V–P curves of the single-cell. f) Schematic diagram of the dual modification strategy. (g) Long-term stability under PCFC mode and PCEC mode. (a) Reproduced with permission.^[96] Copyright 2017, American Chemical Society. (b, c) Reproduced with permission.^[97] Copyright 2013, Springer Nature. (d,e) Reproduced under the terms of the CC-BY Creative Commons Attribution 4.0 International^[98] Copyright 2022, The Authors, published by Springer Nature. (f,g) Reproduced under the terms of the CC-BY Creative Commons Attribution 4.0 International^[15a] Copyright 2024, The Authors, published by Springer Nature.

can lead to electrostatic repulsion between different anions (O^{2-} and X^-) located on identical sublattice oxygen vacancies, which serve as key active sites for reactions and ion transport pathways, in turn improving proton mobility and conductivity.^[101] When halide ions directly replace lattice oxygen to maintain charge neutrality, the oxidation state of nearby metal cations is reduced, making it easier to lose lattice oxygen such that the concentration of oxygen vacancies increases. For instance, in F-doped SFM (F-SFM), the substitution of O^{2-} with F^- , resulted in a partial shift of Fe ions from Fe^{4+} to Fe^{3+} , adjust-

ing the average oxidation state from $\text{Fe}^{3.17+}$ in SFM to $\text{Fe}^{3.06+}$ in F-SFM.^[110]

Although PCEC already exhibits high proton conductivity, anion doping can further enhance this by reducing the basicity of the perovskite oxide.^[111] For example, the hydration capability of $\text{BaCo}_{0.4}\text{Fe}_{0.4}\text{Zr}_{0.1}\text{Y}_{0.1}\text{O}_{2.9-\delta}\text{F}_{0.1}$ (BCFZYF) was significantly enhanced after doping a small amount of F.^[112] The high electronegativity of F^- compared to O^{2-} increases the polarity of $\text{M}-\text{V}''_{\text{O}}-\text{M}$ bonds, promoting H_2O adsorption at oxygen vacancies, and generating more proton defects. As

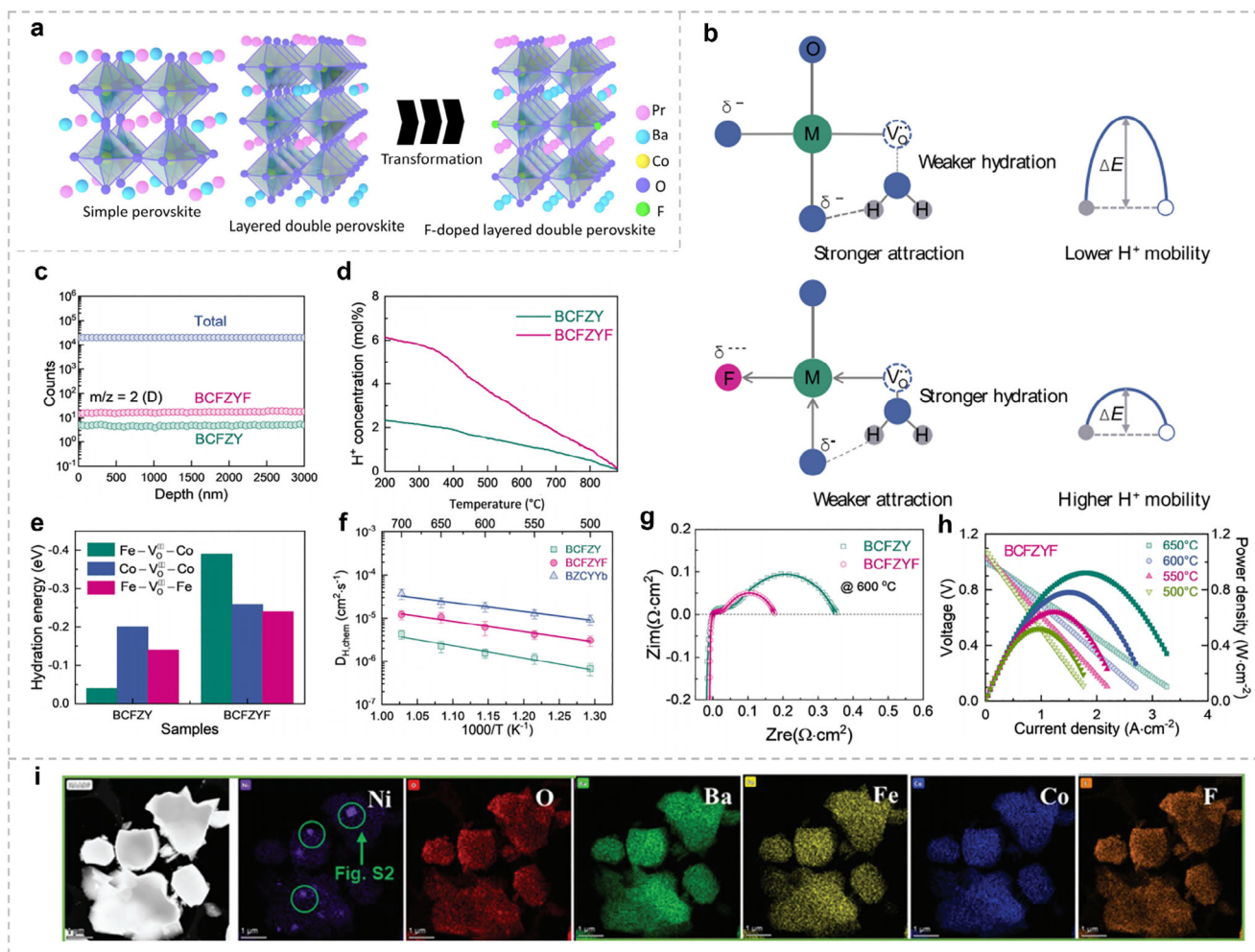


Figure 15. a) Schematic illustration of the $\text{Pr}_{1.1}\text{Ba}_{0.9}\text{Co}_2\text{O}_{5+\delta}$ sample and the $\text{P}_{1.1}\text{BCOF}_{0.1}$ sample phase transformation after F-doping. b) Schematic of fluorination inductive effect to promote the hydration reaction and the proton mobility in perovskite oxides. c) TOF-SIMS depth profile of $m/z = 2$ (D) signal in D_2O treated BCFZY(F) samples. d) estimated proton concentration of BCFZY and BCFZYF samples at various temperatures. e) hydration energy value comparison for BCFZY(F). f) Arrhenius plots of $D_{\text{H, chem}}$ of BCFZY, BCFZYF, and BZCYYb bar samples. g) typical Nyquist plots of symmetric BCFZY(F)|BZCYYb = BCFZY(F) cells at 600 °C. h) I–V–P curves of PCFC with BCFZY(F) as air electrode. i) The elements distribution of N-BCFZYNF sample. (a) Reproduced with permission.^[104] Copyright 2023, Elsevier. (b–h) Reproduced with permission.^[112] Copyright 2022, Elsevier. (i) Reproduced with permission.^[113] Copyright 2024, John Wiley and Sons.

illustrated in Figure 15b, this weakened O···H interactions and lowered the proton diffusion barrier in the perovskite oxide, as corroborated by time-of-flight secondary ion mass spectrometry (TOF-SIMS) and thermogravimetric analysis (TGA). These showed higher proton concentrations and faster proton mobility in BCFZYF than BCFZY (Figure 15c–e). Moreover, anion doping also improves proton mobility. As depicted in Figure 15f, the D_{chem} value for BCFZYF was $1.21 \times 10^{-5} \text{ cm}^2 \text{ S}^{-1}$ at 700 °C, three times higher than that of BCFZY ($4.30 \times 10^{-6} \text{ cm}^2 \text{ S}^{-1}$), and comparable to the electrolyte BZCYYb. A symmetric cell with a BCFZYF air electrode demonstrated lower polarization impedance, and the peak power density of a single cell reached 0.921 W cm^{-2} at 650 °C shown in Figure 15g,h. Chen et al.^[113] further observed that doping $\text{Ba}(\text{Co}_{0.4}\text{Fe}_{0.4}\text{Zr}_{0.1}\text{Y}_{0.1})_{0.95}\text{Ni}_{0.05}\text{O}_{3-\delta}$ with a small amount of fluorine led to the in situ precipitation of NiO (as shown in Figure 15i). The high electronegativity of F weakened lattice M–O bonds, selectively precipitat-

ing Ni–O during high-temperature treatment.^[114] Through this dual modification of bulk and surface properties, the as-prepared $\text{Ba}(\text{Co}_{0.4}\text{Fe}_{0.4}\text{Zr}_{0.1}\text{Y}_{0.1})_{0.95}\text{Ni}_{0.05}\text{F}_{0.1}\text{O}_{2.9-\delta}$ exhibited faster oxygen adsorption/desorption and hydration rates, as well as enhanced oxygen ion and proton transport. Consequently, single cells with this air electrode achieved a peak power density of 996 mW cm^{-2} at 650 °C in FC mode and a maximum electrolysis current density of 1570 mA cm^{-2} under 1.3 V in EC mode.

5.2. Microstructure Optimization

The structure of an electrode directly affects its efficiency and stability, making it crucial to optimize this aspect to enhance PCEC performance. The structure of electrode-pore morphology, channel design, and the introduction of functional layers play a significant role in enhancing mass transport, reducing polarization

resistance, and increasing the number of active reaction sites. A well-optimized electrode structure facilitates better gas diffusion, proton conduction, and electrochemical reaction kinetics, leading to higher power densities and more durable performance. The development of advanced electrode designs, such as finger-like channeled structures and the incorporation of functional layers, has been shown to address challenges such as poor gas diffusion, high tortuosity, and electrode degradation, ultimately boosting the overall efficiency of PCECs. These structural improvements not only enhance performance but also help mitigate degradation mechanisms, such as Ni migration and particle coarsening, ensuring stable operation over long-term usage.^[115]

5.2.1. Finger-Like Channeled Electrodes

Traditional sponge-like porous electrodes suffer from poor uniformity of pores, high tortuosity, and limited gas diffusion, reducing the overall performance of ceramic cells. While adjustments to pore morphology or filling methods may improve performance,^[116] the inherently tortuous microstructure will continue to present significant limitations.^[117] Research has demonstrated that finger-like channels in fuel and air electrodes improve gas diffusion and conduction.^[118] In fuel electrodes, these channels significantly reduce the molar fraction gradients of H₂, CO, CH₄, and CO₂ compared to structures without them.^[119] Phase inversion technology is widely used to fabricate microtubular ceramic cells with finger-like channels in the fuel electrode layers, further optimizing efficiency.^[120]

Pan et al.^[121] successfully fabricated Ni-BZCYYb supported single cells with straight, open, finger-like pores (diameter 30–80 μm; length 500 μm) by combining tape casting and phase inversion techniques to graphite and substrate layers (Figure 16a,b). Fabricated under dry-pressing conditions, the electrochemical performance of these unique micro-structured cells was significantly better than single cells. Specifically, using hydrogen with 3% H₂O as fuel and ambient air as the oxidant, the peak power density of Ni-BZCYYb reached 1.389 W cm⁻², with a polarization resistance of 0.039 Ω cm², whilst the dry-pressed single cells only achieved 0.929 W cm⁻² and 0.113 Ω cm² at 700 °C in FC mode. Furthermore, in EC mode (with 3% steam in the air), the current density of Ni-BZCYYb at 1.3 V was 2.066 A cm⁻², considerably higher than that of the dry-pressed single cells. This was attributed to the phase inversion technique, which improved mass transport, reduced concentration polarization, and boosted output.

Fuel electrode-supported tubular PCECs are more commonly fabricated using phase inversion methods than flat single cells with finger-like channels. Zhao et al.^[120b] utilized the immersion-induced phase inversion technique to create NiO-BZCYYb hollow fibers featuring an asymmetric structure in the fuel electrode support, composed of a sponge-like layer and a finger-like porous layer (Figure 16c). By applying a porous Sm_{0.5}Sr_{0.5}CoO₃ (SSC)-BZCYYb air electrode using a suspension coating process, the resulting single cell achieved a peak power density of 254 mW cm⁻² at 650 °C. Similarly, Hou et al.^[120a] fabricated tubular PCECs using a combination of phase inversion and dip coating, producing cells that exhibited excellent peak power density, electrolysis current density, along reasonable Faradaic ef-

iciency. In addition, Li et al.^[122] used phase inversion to co-extrude NiO-BZCYYb-supported seven-channel micro-monolithic structures (Figure 16d), which featured uniform channel distribution and shorter gas diffusion paths. The assembled cell, with a Ni-BZCYYb fuel electrode support |BZCYYb electrolyte| PBSCF air electrode structure, exhibited a peak power density of 0.94 W cm⁻² in FC mode at 700 °C and an electrolysis current density of 2.17 A cm⁻² at 1.3 V at 700 °C (Figure 16e,f). EIS analysis revealed that the structured cell demonstrated significantly reduced gas diffusion polarization resistance compared to single-channel cells. Dmitry Medvedev et al.^[123] developed tubular PCECs using a tape casting method combined with a dual approach using all Ni-based functional electrodes, resulting in a larger electrode area of 4.6 cm² (Figure 16g). This cell exhibited a high hydrogen production rate, generating 19 mL min⁻¹ of hydrogen at 600 °C, outperforming the most conventional button-type and planar PCECs.

5.2.2. Introducing Functional Layer

A functional layer (FL) is a thin coating applied at the interface between the electrode and electrolyte in PCECs to optimize their interaction. Designed to enhance electrical conductivity, stability, and catalytic activity, the FL improves the overall performance of the electrode by facilitating better electrode-electrolyte interaction. Additionally, it reduces impedance, increases the number of reaction sites, and boosts long-term stability by preventing common degradation mechanisms, such as Ni migration and particle coarsening, during high-temperature operation.^[124]

In recent studies, interface engineering has been shown to significantly improve the electrochemical performance of PCECs. For instance, Choi et al.^[125] introduced a thin layer of PrBa_{0.5}Sr_{0.5}Co_{1.5}Fe_{0.5}O_{5+δ} (PBSCF) on the surface of BZCYYb electrolyte, as shown in Figure 17a–d. This modification improved the electrode-electrolyte contact, significantly reducing the ohmic resistance, leading to enhanced peak power density and overall cell performance, that the power density increased from 0.89 W cm⁻² to 1.098 W cm⁻² at 600 °C. Another representative example involves the introduction of a mono-grain composite interlayer composed of PBSCF and BZCYYb as an FL to optimize the air/steam electrode-electrolyte interface in PCECs,^[12] as shown in Figure 17e–f. This novel interlayer structure significantly extends the electrode/electrolyte interface and increases the concentration of vertically aligned oxygen vacancies. As a result, both ohmic and polarization resistance were reduced, leading to better performance at low operating temperatures, down to 350 °C. Under these conditions, the PCEC exhibited an exceptional peak power density of 0.50 W cm⁻² in fuel cell mode and a current density of 0.25 A cm⁻² at 1.3 V in electrolysis mode (Figure 17g–h). The PCEC with this mono-grain composite interlayer demonstrated high peak power density, current densities, and excellent stability under static and dynamic conditions, as shown in Figure 17i–j, highlighting the potential of interface engineering for high-performance reversible PCECs.

Additionally, air electrode functional layers composed of PBSCF and BZCYYb composites have been employed to mitigate thermal strain and enhance electrochemical performance. When applied at the electrode-electrolyte interface, the FL led to

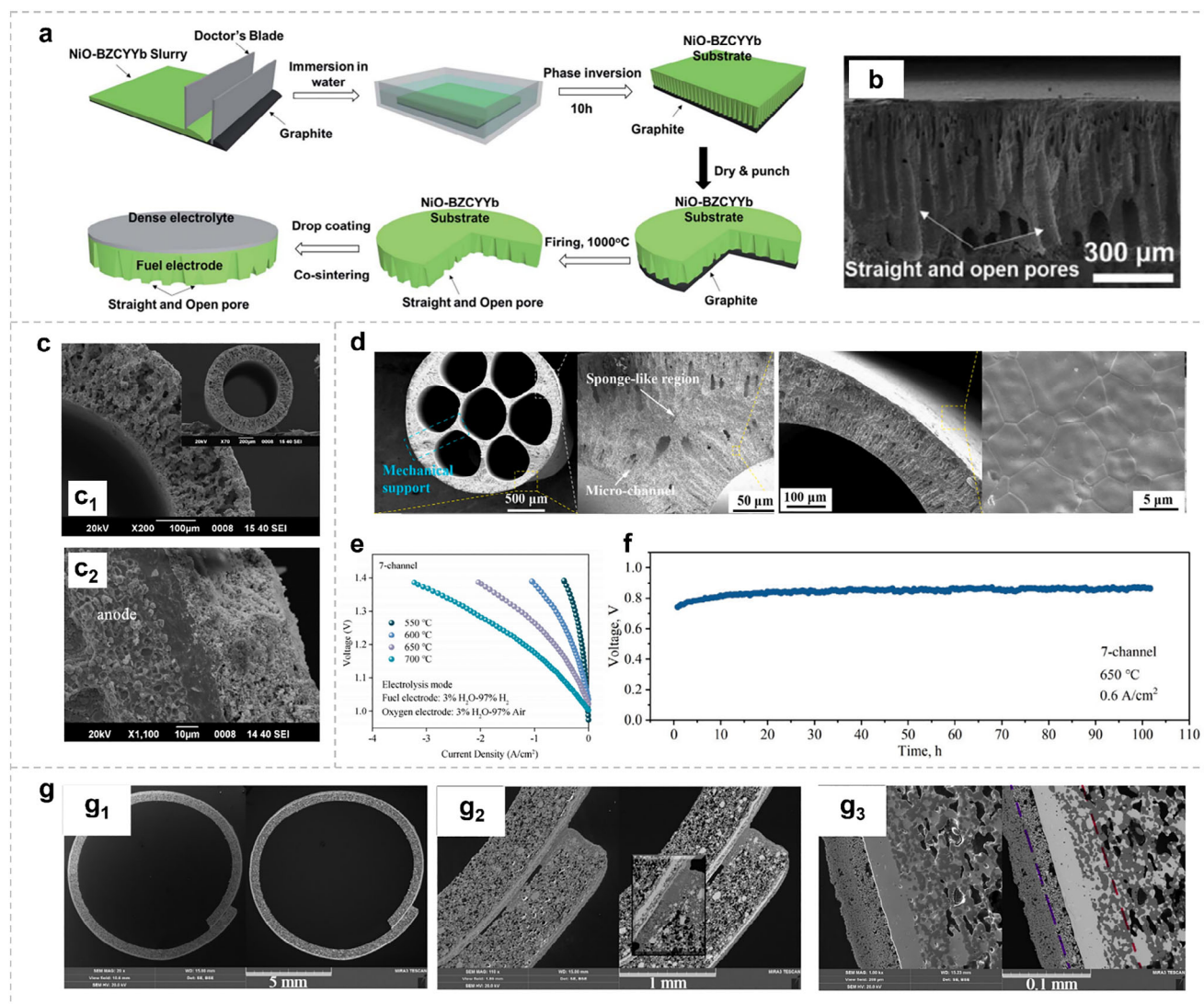


Figure 16. a) Schematics of the fabrication process for PCECs with straight and open pores. b) Microstructure of the overall cross-sectional view after electrochemical testing. c) Fractured surface micro views of NiO-BZCYYb hollow fibers sintered for 5 h at 1400 °C and Cross-sectional views of single cells with fuel electrode-electrolyte bi-layers sintered at 1400 °C. d) 7-channel overall view, the enlarged image on the 7-channel fuel electrode, the electrochemically active region of the 7-channel with a relatively uniform thickness, and the outer surface of the BZCYYb electrolyte. The performance of micro-monolithic cell in electrolysis cell mode at different temperatures (550–700 °C): e) 7-channel, f) Short-term stability test of the 7-channel cell at 650 °C and 0.6 A cm⁻². g) Images of the developed PCEC, including the general view and the glued section. (a,b) Reproduced with permission.^[121] Copyright 2021, Royal Society of Chemistry. (c) Reproduced with permission.^[120b] Copyright 2011, Elsevier. (d–f) Reproduced with permission.^[122] Copyright 2024, Elsevier. (g) Reproduced with permission.^[123] Copyright 2020, Elsevier.

increased peak power densities, reduced polarization resistance, and enhanced stability compared to standard single-cell configurations. These benefits were particularly evident in the intermediate temperature range of 450–600 °C, where the activation energy was reduced from 1.19 to 0.84 eV upon the introduction of the FL. The long-term stability of PCFCs with and without the FL was assessed through potentiostatic measurements at 0.7 V and 500 °C. The results confirmed that the FL significantly improved the operational stability of single cells, with a degradation rate of only 1.7% after 100 h, in contrast to a 2.8% performance loss observed in cells without the functional layer. The results demonstrate the effectiveness of interface modifications in im-

proving both electrochemical properties and thermal stability at the electrode/electrolyte interface.^[126]

Additionally, Ni-BZCYYb electrodes are widely used in both PCFC and PCEC modes owing to their good catalytic activity. Nonetheless, these electrodes suffer long-term stability issues, especially under electrolysis conditions. This is primarily caused by microstructural changes at the Ni-electrolyte interface, such as Ni migration and particle coarsening, reducing the TPB density and diminishing electrode performance. Specifically, Ni migration into the electrolyte layer reduces proton conduction while introducing electronic conduction. Meanwhile, particle coarsening shortens the TPB and weakens the electronic conductivity of

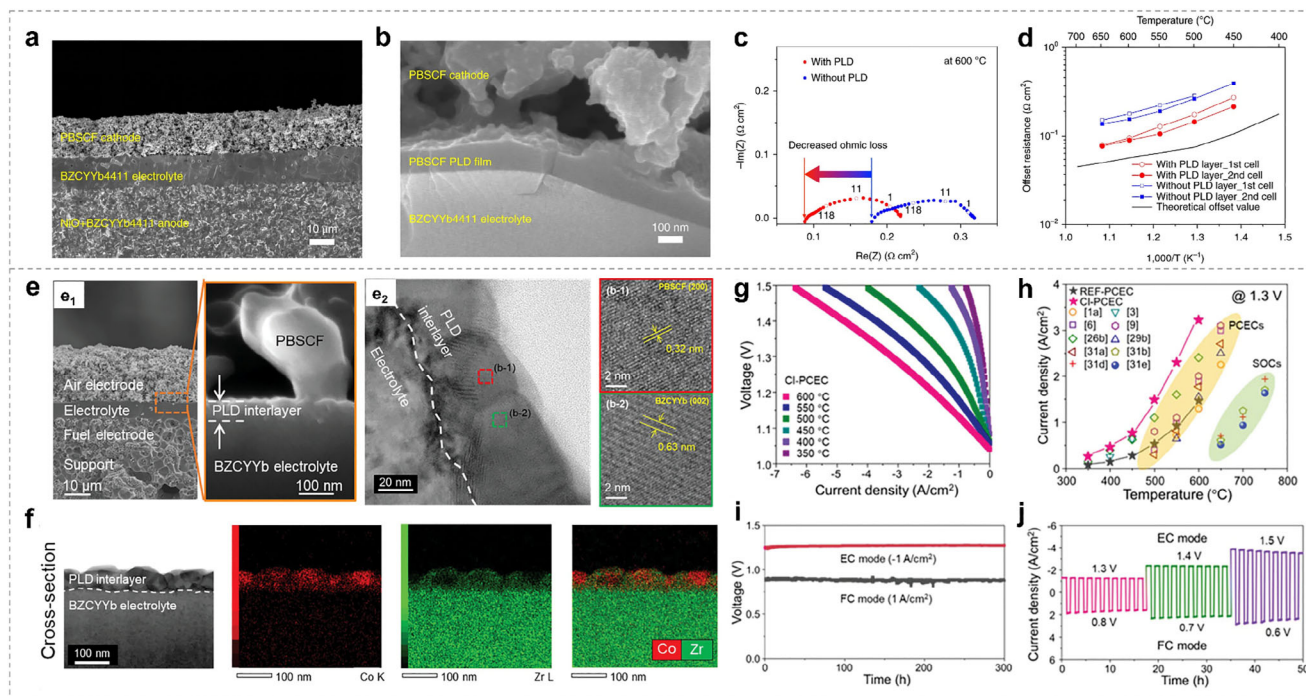


Figure 17. SEM images of the single cells: a) Cross-section. b) Expanded view showing the FL layer at the electrolyte–air electrode interface. c) Impedance spectra at 600 °C, showed a significant decrease after the introduction of the FL layer. d) Reduced ohmic resistance under OCV. e) Cross-sectional SEM image and TEM image of the composite interlayer between the air electrode and electrolyte. f) TEM image and EDS mapping of the interlayer cross-section. g) I–V curve of the single cell in electrolysis mode. h) Comparison of current density at 1.3 V with previously reported single cells. i) Stability test at 500 °C under constant current densities of $\pm 1 \text{ A cm}^{-2}$ in FC and EC modes. j) Reversible FC/EC cycling with dynamic voltage from 0.8–0.6 V (FC) and 1.3–1.5 V (EC). (a–d) Reproduced with permission.^[125] Copyright 2018, Springer Nature. (e–j) Reproduced with permission.^[12] Copyright 2024, John Wiley and Sons.

the electrode, leading to irreversible degradation.^[127] These effects are exacerbated by high temperatures (above 1400 °C), accelerating both Ni migration and coarsening. To address these degradation issues, a NiO–BZCYYb nanocomposite FL has been introduced between the fuel electrode and the electrolyte, functioning as an active catalytic interlayer. This FL effectively limits Ni migration into the electrolyte and suppresses particle coarsening, owing to the nanoscale dispersion of NiO and electrolyte phases. Such structural advantages contribute to improved long-term stability of the electrode while preserving a high TPB density.

Beyond its roles in extending the TPB length and sustaining catalytic activity at intermediate temperatures, the porosity of the FL plays a crucial role in cell performance and stability. The fine-grained structure of FL helps improve interfacial conductivity and ensures sustained performance over time. The adjacent fuel electrode support structure provides i) mechanical support for the fuel cell (for fuel electrode-supported cells) and ii) low-resistance gas diffusion pathways for fuel and reaction products (such as H_2) at the fuel electrode.^[128] Notably, the low porosity of the FL also aids the deposit of the electrolyte layer via colloidal coating or spin-coating methods.^[129] To better understand the influence of FL porosity, various studies have focused on optimizing the microstructure to improve their catalytic activity and durability. For example, Ebbesen et al.^[130] demonstrated that the porosity of the FL significantly affects the single-cell performance and durability, influencing gas diffusion and concentration resis-

tance during electrolysis. Hauch et al.^[127] also showed that optimizing the microstructure of Ni–BZCYYb FL would reduce the performance degradation rate to as low as 0.3–0.4% kh^{-1} , primarily by suppressing Ni migration through decreased porosity and a well-distributed TPB. Although Ni migration could still be observed after over a year of testing, its rate had significantly slowed down.^[74] Rainwater et al.^[131] investigated the effect of porosity on Ni–BZCYYb FL and found that reducing the porosity to $\approx 37\%$ resulted in the best performance, reaching a peak power density of 1.2 W cm^{-2} at 750 °C. Altogether, these examples demonstrate the critical role of FL porosity in improving the stability, efficiency, and overall performance of proton-conducting ceramic cells.

5.3. Multiphase Regulating Strategies

Multiphase regulating strategies involve the integration of multiple phases within a single electrode structure to optimize the electrochemical properties of electrodes, overall playing a crucial role in the performance and stability of PCECs. This is done through careful control of phase composition, morphology, and interactions between different phases. By leveraging the synergy between multiple phases, such as proton conductors, oxygen ion conductors, and electronic conductors, these approaches can significantly improve catalytic activity, proton conductivity, and electrode stability. These multiphase materials are designed to create

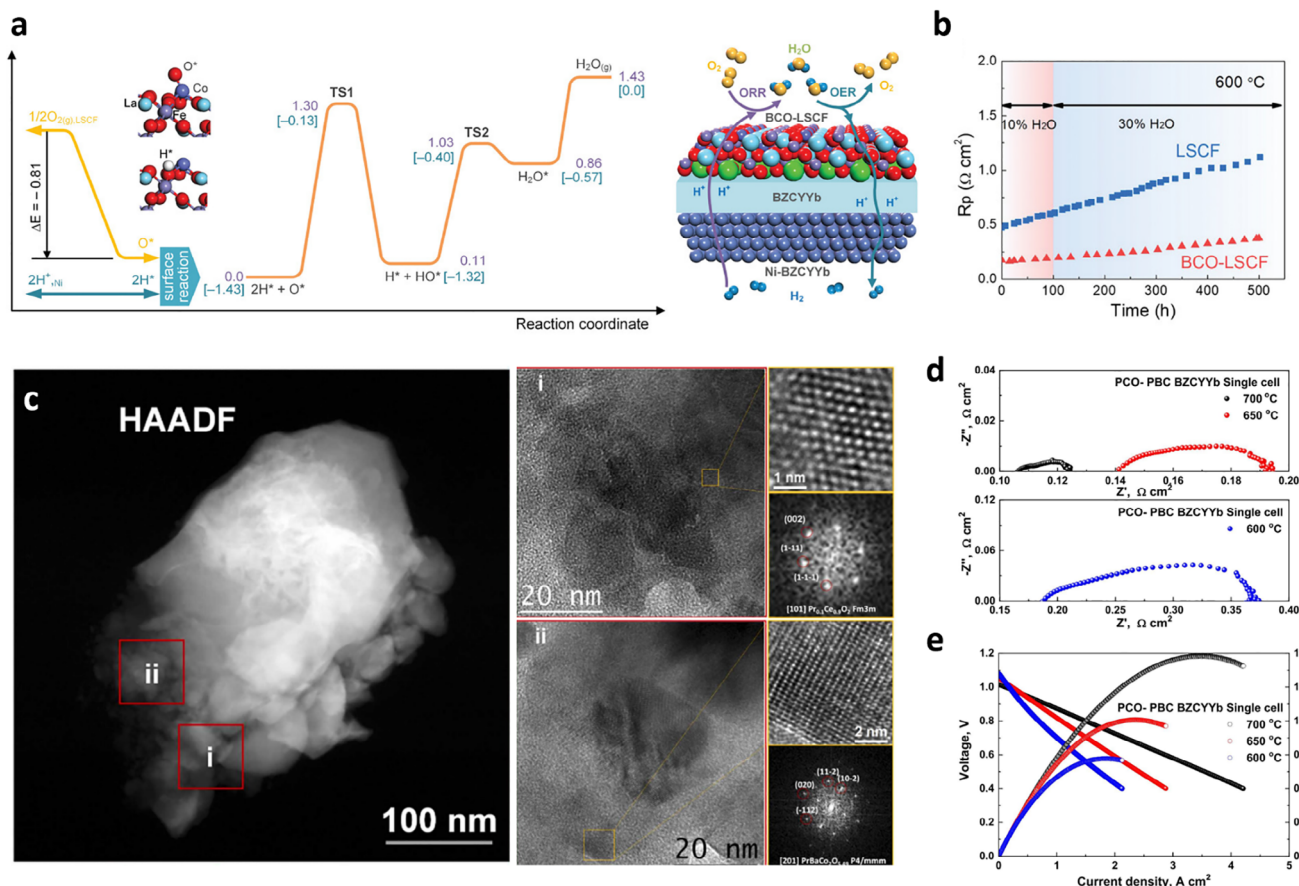


Figure 18. a) Schematic of the energy profile for the fuel cell and water electrolysis modes. b) The polarization resistance of LSCF and BCO-LSCF electrodes in humid air at 600 °C over 500 h. c) High-angle annular dark-field (HAADF) STEM micrograph and X-ray energy dispersive spectrum mapping of PCO-PBC. d) EIS curves at 700, 650, and 600 °C with wet H_2 fuel. e) I–V–P curves at 700, 650, 600 °C. (a,b) Reproduced with permission.^[134] Copyright 2021, John Wiley and Sons. (c–e) Reproduced with permission.^[136] Copyright 2023, Elsevier.

well-defined interfaces and ensure robust electrochemical performance under various operating conditions, enhancing both the ORR and OER. This section delves into various techniques employed to achieve such multiphase structures, highlighting their impact on improving the performance and durability of PCECs.

5.3.1. Impregnation Method

In SOFCs, a common strategy to enhance the ORR activity and durability of the air electrode is through surface modification with a material that functions as a protective coating or catalyst, known as the impregnation method. In this process, the precursor solution infiltrates the porous scaffold. Subsequent heat treatment causes the nitrate solution to decompose, leading to a uniform distribution of nanoscale catalysts across the surface of the scaffold. This is also applicable to PCEC, where impregnating active and ionically conductive catalysts into the PCEC electrode materials can improve water electrolysis performance. Wang's group^[132] used BZY as the backbone with $LaCoO_3$ (LC) as the electrocatalysts, yielding stable performance over 900 h in a durability test on a symmetric cell, run in humidified air. Saqib et al.^[133] incorporated an oxygen-ionic conductor,

$Sm_{0.2}Ce_{0.8}O_{2-\delta}$ (SDC), into BCFZY-BZCYYb air electrode, enhancing both OER and ORR catalytic activities and effectively reducing the impedance of both the symmetric cell and the single cell. Zhou's group^[134] deposited a BCO coating onto the LSCF electrode using a one-step impregnation method and conducted DFT calculations to investigate the electrochemical mechanism, as depicted in Figure 18a. Their computational analysis revealed that BCO modification reduces the energy barrier for hydroxyl species decomposition by 0.45 eV compared to bare LSCF, which directly correlates with the enhanced oxygen exchange kinetics shown in Figure 18b. They proposed that during fuel cell and electrolysis cell operation, Co ions act as active centers, with the rate-determining step being the formation and decomposition of surface hydroxyl species. After BCO impregnation, the surface oxygen exchange process is enhanced, which facilitates the ORR and OER processes. The long-term stability of the material was also improved, as evidenced by a reduction in the degradation rate of the polarization resistance for the BCO-coated LSCF electrode, from 1.3×10^{-3} to $4.1 \times 10^{-4} \Omega \text{ cm}^2 \text{ h}^{-1}$ (Figure 18b). Later, the group incorporated a multiphase catalyst consisting of PBC and BCO nanoparticles via impregnation, which further enhanced catalytic activity and stability, reducing polarization resistance to $0.043 \Omega \text{ cm}^2$ at 600 °C and achieving a high current

density of 1.82 A cm^{-2} at 1.3 V in EC mode.^[135] Similarly, Pei's group^[136] used fluorite-based ceria doped with praseodymium oxides (PCO) as a surface coating catalyst for the PBC air electrode, enhancing both activity and durability in the EC mode. As shown in Figure 18c, the HAADF STEM images of PCO-PBC powder reveal that the lattices in the red squared regions i) and ii) correspond to the PCO and PBC phases, respectively. This distinct phase separation enables PCO to preferentially interact with steam, as confirmed by post-test compositional analysis showing an 83% reduction in Ba surface segregation compared to unmodified PBC. Electrochemical tests conducted on a single cell with the PCO-PBC oxygen electrode showed a notably total low resistance and high current density of 2.69 A cm^{-2} at 1.3 V (Figure 18d,e). These studies highlight the potential of impregnation strategies to improve the performance of both LSCF and double perovskite-based air electrodes in PCECs.

5.3.2. Mechanical Mixing Strategy

The mechanical mixing strategy involves blending different materials physically, via grinding or milling, to form composite structures that leverage the beneficial properties of each component. This approach is widely applied in the development of air electrodes for PCECs. By mixing electrolyte materials, such as BZCYYb, with perovskite electrodes, composite air electrodes are created that not only enhance proton conductivity but also lengthen the three-phase boundary (TPB), mitigating thermal mismatch between the electrode and electrolyte. The primary function of mechanical mixing is to improve proton conduction, which is often a rate-limiting factor in electrochemical performance. Research has shown that the mechanical mixing of perovskite electrodes with proton-conducting electrolytes can substantially improve electrochemical performance. For instance, Wang et al.^[137] developed a composite electrode of $\text{Ba}_{0.5}\text{Sr}_{0.5}\text{Co}_{0.7}\text{Fe}_{0.2}\text{Ni}_{0.1}\text{O}_{3-\delta}$ - $\text{BaZr}_{0.1}\text{Ce}_{0.7}\text{Y}_{0.1}\text{Yb}_{0.1}\text{O}_{3-\delta}$ (BSCFN-BZCYYb) in different mass ratios for PCEC applications. Their results showed that the 8:2 ratio yielded optimal performance, achieving a peak power density of 1.14 W cm^{-2} and low polarization resistance of $0.062 \Omega \text{ cm}^2$ at 750°C . Moreover, the composite electrode possesses excellent stability with negligible impedance changes during a 50-h cycling test, demonstrating the effectiveness of mechanical mixing in the electrolyte-perovskite composite in enhancing its efficiency and durability.

Additionally, mechanical mixing has been shown to improve the chemical compatibility and long-term stability of perovskite-based composites. Wang et al.^[138] further enhanced the chemical stability of composite electrodes by mixing the cobalt-free perovskite $\text{Ba}_{0.95}\text{La}_{0.05}\text{Fe}_{0.8}\text{Zn}_{0.2}\text{O}_{3-\delta}$ (BLFZ) with BZCYYb. They found that the composite exhibited excellent chemical compatibility at temperatures below 1100°C . When exposed to humidified air (3% H_2O), the polarization resistance decreased from 2.072 to $1.334 \Omega \text{ cm}^2$ at 600°C . The power density of single cells using the BLFZ-BZCYYb composite electrodes reached 329 mW cm^{-2} at 750°C , and the composite electrodes maintained long-term stability over 100 h of operation. The optimization of composite ratios is another key aspect of mechanical mixing. Yang et al.^[139] explored the effect of varying the ratio of BZCYYb and

$\text{Nd}_{1.95}\text{NiO}_{4+\delta}$ (NNO) in composite electrodes to reduce polarization resistance. Their findings showed that increasing the NNO content led to a reduction in polarization resistance, with the lowest value of $0.43 \Omega \text{ cm}^2$ achieved at 60 wt% NNO at 750°C . This study highlighted the importance of fine-tuning the TPB and proton conductivity to enhance electrode performance under different operating conditions. Mechanical mixing has also been used to optimize charge transfer efficiency in composite electrodes.

Yang et al.^[140] introduced a composite of PBSCF and BZCYYb to create a thin-film electrode-electrolyte composite functional layer. This design expanded the interface between the air electrode and the electrolyte, significantly reducing polarization resistance. The result was a 4% to 20% increase in power output, demonstrating that structural optimization through mechanical mixing can significantly boost performance in proton ceramic fuel cells. Finally, composite electrodes have been proven to improve electrochemical performance under specific operating conditions, such as steam electrolysis. Zheng et al.^[141] studied a $\text{Ba}_{0.5}\text{Gd}_{0.8}\text{La}_{0.7}\text{Co}_2\text{O}_{6-\delta}$ - $\text{BaZr}_{0.5}\text{Ce}_{0.4}\text{Y}_{0.1}\text{O}_{3-\delta}$ (BGLC587-BZCY541) composite oxygen electrode under steam electrolysis conditions, revealing that the rate-limiting step for steam electrolysis occurred at the surface oxygen electrode process. Their results indicated that the three-phase boundary process at the contact point of BGLC587-BZCY541 outperformed the two-phase boundary process, emphasizing the advantages of composite electrode structures in achieving high electrochemical performance. Overall, these studies demonstrate the significant potential of mechanically mixed composite electrodes in improving proton conductivity, catalytic activity, and stability in PCECs. They highlight the importance of optimizing the TPB and electrode-electrolyte interactions for enhanced performance.

5.3.3. In Situ Exsolved Strategy

Impregnation, electro(deposition), and vapor deposition techniques are the most common methods used to create supported catalyst structures and improve catalytic capability by decorating high-surface-area supports with nanoparticles. Despite the abilities of these conventional methods to improve PCEC performance, they often also result in weak and shallow bonding between the metal nanoparticles and the support,^[67] which can cause the nanoparticles to migrate, sinter, or even detach during thermochemical or electrochemical catalysis. In contrast, in situ exsolution is a process where nanoparticles grow through phase separation within the solid phase, forming a tightly bonded precipitate phase with the host material. This process avoids the separation issues common in traditional methods whilst still enhancing catalytic activity, effective surface area, and resistance to external gas poisoning.^[142] A notable example of in situ exsolution is the selective exsolution of cations from the perovskite lattice, which has been successfully demonstrated in various perovskite oxides for catalytic and electrocatalytic applications.^[143] Liang et al.^[144] manipulated the elemental composition of the perovskite precursor and introduced A-site cation vacancies to facilitate the exsolution of NiO nanoparticles (as shown in Figure 19a,b). The resulting

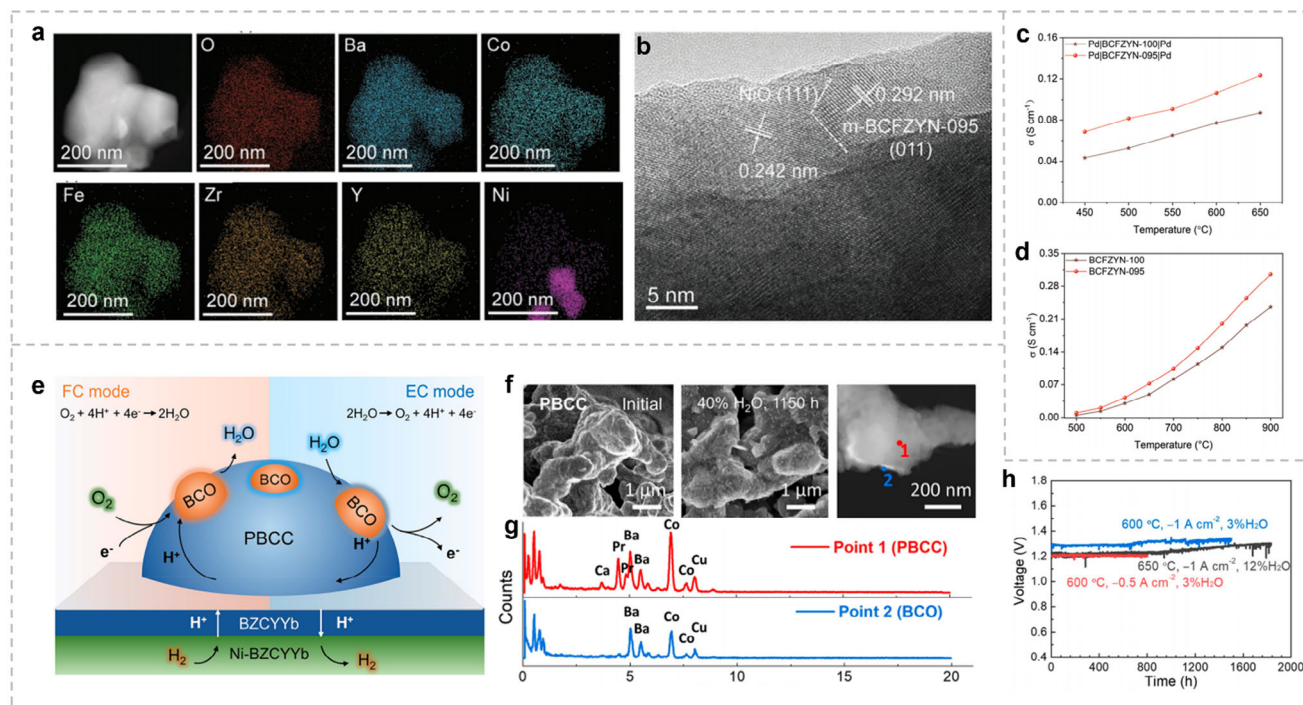


Figure 19. a) EDX-mapping result of BCFZYN-095. b) HRTEM image of BCFZYN-095. c) The proton conductivity of BCFZYN-100 and BCFZYN-095 at 450–650 °C. d) Oxygen-ion conductivity of BCFZYN-100 and BCFZYN-095 from 500 to 900 °C. e) Schematic illustration of an R-PCEC with a PBCC exsolved BCO air electrode operated in fuel cell and electrolysis modes. f) SEM and TEM images of the PBCC electrodes before and after testing (1150 h, 700 °C, 40% H₂O), and g) EDX spectra of point 1 and point 2, as marked in the TEM image. h) Long-term stability of PBCC measured in electrolysis mode. (a–d) Reproduced with permission.^[144] Copyright 2022, John Wiley and Sons. (e–h) Reproduced with permission.^[147] Copyright 2021, American Chemical Society.

Ba_{0.95}(Co_{0.4}Fe_{0.4}Zr_{0.1}Y_{0.1})_{0.95}Ni_{0.05}O_{3-δ} (BCFZYN-095) composite exhibited improved proton conductivity and enhanced ORR activity. Moreover, a single cell using this material achieved a peak power density of 1040 mW cm⁻² at 650 °C, with excellent stability over 400 h at 550 °C. The selective exsolution of Ni cations was attributed to the A-site cation deficiency and the difference in ionic radius between Ni³⁺ and Ni²⁺.^[145] Enhanced proton and oxygen ion conductivity (Figure 19c,d) were confirmed by hydrogen and oxygen permeation measurements, further demonstrating the catalytic benefits of this approach.

In addition to optimizing metal cation exsolution, researchers have explored anion regulation to modify perovskite materials. For example, Chen et al.^[113] introduced fluoride (F) into the perovskite structure to weaken the metal-oxygen (M–O) bonds, resulting in a modified perovskite material, Ba(Co_{0.4}Fe_{0.4}Zr_{0.1}Y_{0.1})_{0.95}Ni_{0.05}F_{0.1}O_{2.9-δ} (N-BCFZYNF). This material showed significantly improved oxygen relaxation times and surface exchange kinetics compared to the unmodified material. At 600 °C, N-BCFZYNF exhibited a relaxation time of 120 s, far shorter than the 453 s required for the unmodified BCFZY. This enhancement improved oxygen transport and surface exchange kinetics, leading to improved overall performance. Similarly, Zhou et al.^[47] synthesized PrBa_{0.8}Ca_{0.2}Co₂O_{5+δ} with exsolved BaCoO_{3-δ} nanoparticles (PBCC-BCO) shown in Figure 19e–g, which significantly reduced polarization resistance (0.24 Ω cm² at 600 °C) and exhibited excellent stability in humidified air. The interaction between BCO nanoparticles and the PBCC phase pro-

moted efficient water dissociation and rapid oxygen desorption, contributing to superior OER activity. An R-PCEC using PBCC-BCO delivered a peak power density of 1.06 W cm⁻² at 600 °C in FC mode and sustained durability over 1833 h in EC mode at 1.3 V (as shown in Figure 19h). Further studies have also explored in situ exsolution for enhancing surface reaction kinetics. Zhu et al.^[14a] used temperature-induced exsolution to generate SrCo_{0.5}Nb_{0.5}O_{3-δ} (SCN) nanoparticles on PrSrCo_{1.8}Nb_{0.2}O_{6-δ} (PSCN), improving both ORR and OER performances by facilitating steam adsorption and protonation. In situ X-ray diffraction confirmed the stability of SCN nanoparticles above 900 °C, and DFT calculations further indicated reduced energy barriers for oxygen and steam dissociation, thus enhancing electrochemical performances.

Moreover, in situ exsolution is often observed by reducing atmospheres in PCECs, which boosts catalytic activity and CO₂ poisoning resistance. Duan et al.^[66] demonstrated that exsolved Ni nanoparticles facilitate hydrogen production in EC mode and hydrogen oxidation in FC mode. Notably, under high temperatures and extensive current conditions, the nanoscale Ni particles exsolved from the fuel electrode effectively increased catalytic surface area and reduced migration distances between Ni and BZY, thereby improving coking resistance. Therefore, in situ exsolution is a highly effective strategy that enhances proton conductivity, resistance to external poisoning, and durability under extreme operational conditions, altogether enhancing the catalytic activity and stability of perovskite-based electrodes in PCECs.

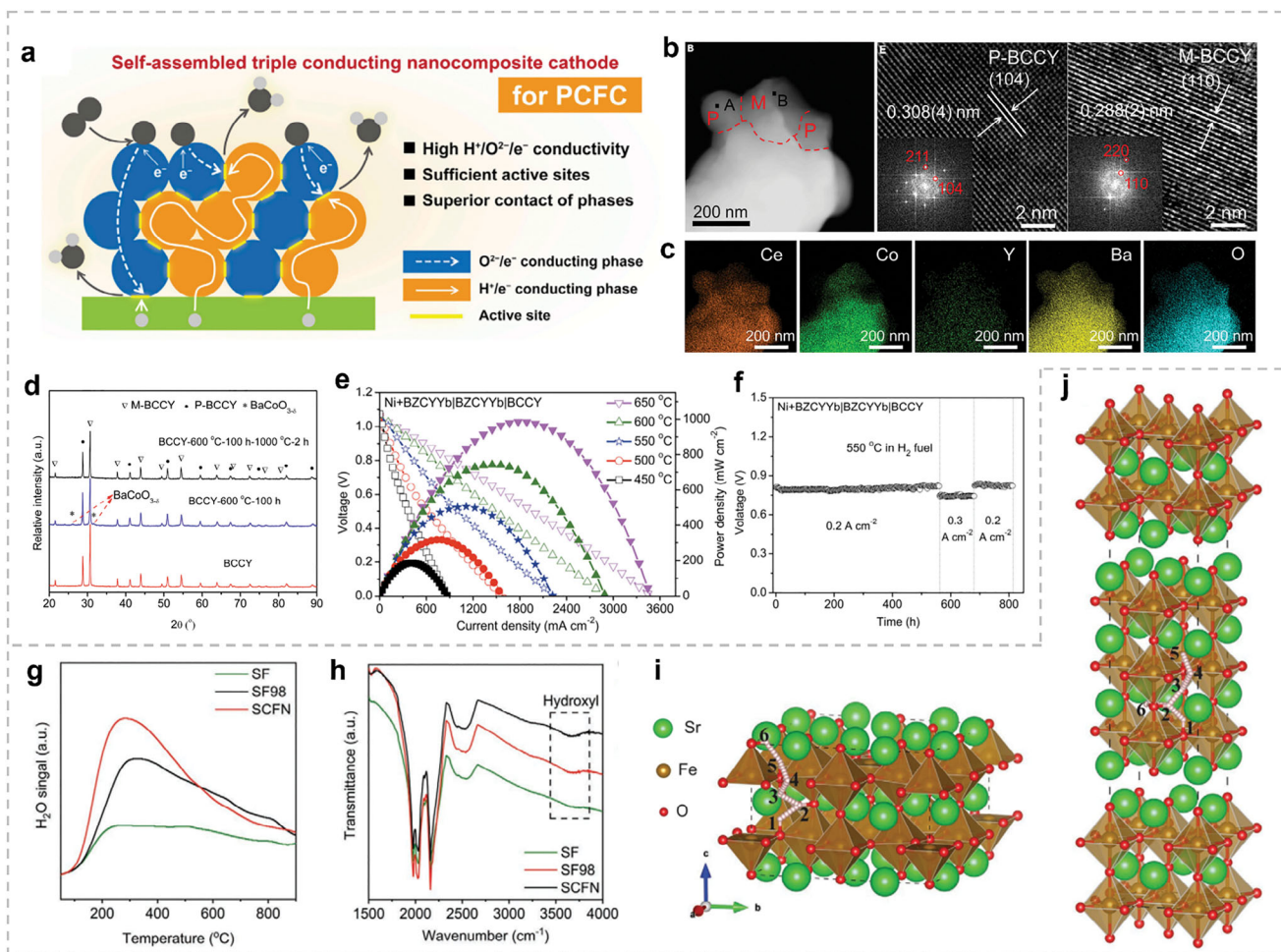


Figure 20. a) Schematic of a self-assembled triple phase ($\text{H}^+/\text{O}^{2-}/\text{e}^-$) conducting nanocomposite electrode. b) STEM image and HRTEM image of a BCCY composite particle. c) STEM-EDX result. d) XRD patterns of the as-synthesized BCCY composite, the BCCY composite calcined at 600 °C for 100 h in air (21 vol.% $\text{O}_2\text{-N}_2$), and the calcined BCCY composite after further treatment at 1000 °C for 2 h in air. e) I–V and I–P curves of a single cell with the configuration of $\text{Ni+BZCYYb|BZCYYb|BCCY}$ at 450–650 °C. f) Operational stability of a single cell with the configuration of $\text{Ni+BZCYYb|BZCYYb|BCCY}$ at constant current densities of 0.2 and 0.3 A cm^{-2} at 550 °C. g) H_2O -TPD signal comparison of SCFN and other samples. h) FTIR profiles of steam-treated powders. i) Distinct OH^- sites in hydrated $\text{Sr}_{16}\text{Fe}_{16}\text{O}_{46}\text{H}$ (SF) and j) hydrated $\text{Sr}_{16}\text{Fe}_{12}\text{O}_{40}\text{H}$ (RP-SF). (a–f) Reproduced with permission.^[148] Copyright 2019, Elsevier. (g–j) Reproduced with permission.^[70] Copyright 2021, John Wiley and Sons.

5.3.4. Self-Assemble Strategy

Various studies have focused on developing composite air electrodes by combining proton-conducting electrolytes with single-phase perovskites or employing surface modifications like infiltration, aimed to introducing proton conduction and additional reaction sites for air electrodes.^[146] However, the weak interactions between mechanically mixed electrodes or infiltrated coatings and the air electrode often lead to significant performance degradation over long-term operations.^[147] Besides, single-phase perovskite electrodes suffer from limited ion transport pathways and fewer active reaction sites. Consequently, there is growing interest in self-assembly strategies. Self-assembled electrodes exhibit stable dual-phase or multiphase structures that enhance proton conductivity, improve electrocatalytic activity, and increase durability.^[148] This strategy leverages the differences in ionic radii and valence states to facilitate the in situ self-assembly of com-

posite phase structures. This strengthens the interaction between different phases, ensures appropriate thermal and chemical compatibility between electrodes and electrolytes, and ultimately enhances stability.^[148,149]

Song et al.^[148] introduced a self-assembled, single-step reconstructed triple-conducting ($\text{H}^+/\text{O}^{2-}/\text{e}^-$) composite electrode via the one-pot method, $\text{BaCo}_{0.7}(\text{Ce}_{0.8}\text{Y}_{0.2})_{0.3}\text{O}_{3-\delta}$ (BCCY), as an air electrode for intermediate-temperature protonic ceramic fuel cells. This composite electrode exhibited enhanced electronic conductivity, a reduced TEC of $15.73 \times 10^{-6} \text{ K}^{-1}$, and sufficient reaction sites (Figure 20a). During the calcination process, the material self-assembled into two distinct phases: the $\text{BaCe}_x\text{Y}_y\text{Co}_z\text{O}_{3-\delta}$ (P-BCCY) phase, which conducts H^+/e^- , and the $\text{BaCo}_x\text{Ce}_y\text{Y}_z\text{O}_{3-\delta}$ (M-BCCY) phase, which conducts O^{2-}/e^- . The two phases were well mixed and intimately connected inside at the nanoscale within the sintered micrometer-sized grains (Figure 20b,c). An additional $\text{BaCoO}_{3-\delta}$ (BC) phase also formed

(Figure 20d) under fuel cell conditions, enhancing electronic conductivity. The composite's exceptional activity stemmed from its triple-conducting properties, with P-BCCY facilitating proton diffusion, M-BCCY enhancing oxygen ion diffusion, and BC ensuring efficient electron transport. The increased number of active sites at the nanoscale interfaces also contributed to the electrode's enhanced performance. When put in practice, a single cell using the BCCY air electrode achieved a peak power density of 508 mW cm⁻² at 550 °C and demonstrated stable operation for over 800 h (Figure 20e,f).

Similarly, Hu et al.^[150] developed a cobalt-free perovskite, PrBa_{0.8}Ca_{0.2}Fe_{1.8}Ce_{0.2}O_{6-δ} (PBCFC), which self-assembled into three phases: defect-rich PBCFC, BaCeO₃, and CeO₂. When used as the air electrode in a single cell, it achieved a peak power density of 1.78 W cm⁻² at 700 °C in FC mode and a current density of 5.00 A cm⁻² at 1.3 V in EC mode. Besides, Huang et al.^[151] synthesized PrBaCo_{1.8}Nb_{0.1}Y_{0.1}O_{5+δ} (PBCNY), which self-assembled into a primary cation-deficient phase and a secondary Ba₂YNbO₆ phase. The secondary phase, formed through Nb, Y, and Ba interactions, stabilized the perovskite structure, provided additional active sites for the ORR and OER, and enhanced proton conductivity. Electrochemical tests revealed a polarization resistance of 0.24 Ω cm² at 600 °C, with single cells achieving a peak power density of 1.99 W cm⁻² in FC mode and a current density of -5.20 A cm⁻² at 1.3 V in EC mode. Building on this approach, Song et al.^[70] further advanced the self-assembly method by developing a cobalt-free multi-phase electrode, Sr_{0.9}Ce_{0.1}Fe_{0.8}Ni_{0.2}O_{3-δ} (SCFN). This electrode comprised two main perovskite phases: a tetragonal SrFeO_{3-δ} (SF) phase and an RP Sr₄Fe₃O_{10-δ} (RP-SF) phase, along with minor NiO and CeO₂ oxide phases. Mass spectrometry (MS) and Fourier transform infrared (FTIR) analyses (Figure 20g,h) showed that the RP-SF phase enhanced hydration and proton transfer related to OER. Additionally, proton migration simulations using the climbing image nudged elastic band (CI-NEB) method confirmed lower migration barriers in RP-SF, facilitating efficient proton transfer (Figure 20i-j). The introduction of NiO and CeO₂ nanoparticles also improved oxygen reaction kinetics. Ultimately, single cells with the SCFN electrode achieved a peak power density of 531 mW cm⁻² at 600 °C and exhibited remarkable stability over 120 h at 550 °C. Berger et al.^[152] discovered that BaCe_{1-(x+0.2)}Fe_xY_{0.2}O_{3-δ} (x = 0.1–0.6) naturally forms a Fe-rich cubic phase and a Ce-rich triangular phase, while Cheng et al.^[153] demonstrated that calcining BaCe_{0.5}Fe_{0.5}O_{3-δ} at 1370 °C produces a dual-phase composite: Ce-rich BaCe_{0.8}5Fe_{0.15}O_{3-δ} (BCF8515) and Fe-rich BaCe_{0.15}Fe_{0.85}O_{3-δ} (BCF1585). This dual-phase material combines the proton-conducting capabilities of BCF8515 with the electronic conductivity of BCF1585, offering a balanced and effective solution for various applications.

Despite significant progress in synthesizing self-assembled perovskite electrodes via one-pot methods, their composition and fine structures are still difficult to control. Therefore, further validation is still required to confirm the scalability of the self-assembly approach for electrode material preparation. Additionally, the interactions between the multi-phase or potentially unstable material layers during this self-assembled process may negatively affect stability or performance. Therefore, a more comprehensive investigation into the physicochemical properties of

the materials and the kinetic behavior involved in the restructuring processes is needed, along with further long-term durability testing.

6. Conclusion and Perspectives

Advancements in PCEC technology present a promising solution for tackling global energy and environmental challenges, particularly through efficient hydrogen production via water electrolysis. This review summarizes the latest advances in electrode materials, focusing on novel material synthesis and structural innovations aimed at improving performance. Key strategies to enhance PCEC efficiency include increasing proton conductivity, optimizing the length of the TPB, and minimizing thermal expansion mismatches between the electrodes and electrolytes. These efforts are essential for advancing PCEC technology to meet future energy demands. However, despite considerable progress, several challenges persist in the field. One of the key obstacles is the limited proton conductivity of conventional perovskite materials, which hampers the catalytic efficiency of PCECs. While composite electrodes that integrate proton-conducting electrolytes such as BZCYYb with perovskite materials show promise, challenges remain in enhancing the mechanical strength, water resistance, and long-term durability of air electrodes. As PCEC technology is still in its infancy, future efforts should concentrate on improving scalability, refining material synthesis techniques, and optimizing interactions between electrode materials and electrolytes. These initiatives are vital for addressing existing limitations and ensuring the technology's viability for large-scale hydrogen production. This review highlights several key aspects of developing PCEC systems.

6.1. Air Electrode Materials

Air electrodes are integral to oxygen reduction and evolution reactions in PCECs. The development of high-performance air electrodes involves improving ionic conductivity, electronic conductivity, and catalytic activity, particularly at intermediate temperatures. Materials like single perovskites, double perovskites, and RP phase perovskites have shown promise, offering a balance of thermal stability, chemical compatibility, and high conductivity. Research continues to optimize these materials to meet the specific demands of PCEC applications.

6.2. Fuel Electrode Materials

Fuel electrode materials are essential for driving the HER in PCECs. These materials must exhibit suitable ionic and electronic conductivities, along with high catalytic activity and stability in a reducing atmosphere. Commonly used fuel electrode materials include Ni-electrolyte composites and perovskite-based materials, though challenges exist in maintaining mechanical strength, porosity, and persistent redox stability. Ongoing research seeks to address these issues to enhance long-term performance and durability.

6.3. Regulation Strategies

Several strategies have been developed to optimize the performance of PCEC electrode materials, including chemical doping, electrode structure optimization, and multicomponent phase construction. Chemical doping can significantly enhance proton and electron conductivity by modifying the crystal structure or creating oxygen vacancies. However, doping must be carefully optimized to avoid drawbacks like phase instability or thermal expansion mismatches. Optimizing electrode structure, through tailoring the microstructure and porosity, can improve performance by increasing the availability of reaction sites and facilitating gas transport. The development of multiphase electrodes also offers a promising strategy, as combining different phases can enhance conductivity and stability while promoting better interactions between the electrode and electrolyte. These strategies provide a pathway to overcoming current limitations and improving the efficiency, stability, and scalability of PCEC systems.

7. Technical Challenges in Water Electrolysis

PCEC technology has made substantial progress in enabling efficient hydrogen production through water electrolysis. However, several technical challenges remain, hindering the full realization of its potential.

7.1. Limited Catalytic Activity of Air Electrode

Despite significant advancements in PCEC technology, air electrode performance remains a major challenge, particularly at lower temperatures (400–700 °C). The catalytic activity of air electrodes for ORR and OER decreases significantly at lower temperatures, limiting overall system efficiency.^[154] This issue becomes more pronounced in larger cells, where Faradaic efficiency tends to drop, sometimes falling below 80%, compared to over 98% in smaller button cells with identical electrodes and electrolytes. Key factors such as water absorption, oxygen vacancy concentration, and electrode stability play a critical role in determining Faradaic efficiency and become more significant as cell size increases.^[155] Developing air electrodes with better water resistance, fuel flexibility, and enhanced stability under these harsh conditions is crucial to improving the reliability and efficiency of PCEC systems.

7.2. Proton Conductivity

Despite advances in proton conductivity through doping and structural optimization, achieving a balance between high conductivity and structural stability remains challenging.^[156] Dopants in perovskite oxides show promise but may reduce mechanical strength or introduce thermal expansion mismatches.^[157] Electronic leakage also limits Faraday efficiency, especially at elevated temperatures.^[158] Inadequate sealing can lead to side reactions and energy loss. Furthermore, addressing degradation mechanisms like hydrogen embrittlement and metal migration is vital for improving the reliability and lifespan of PCEC system.

7.3. Mechanical Issues

Mechanical stability is another key challenge in PCEC systems. Fuel electrodes, particularly those with proton-conducting materials like BZCYYb, suffer from poor compatibility with nickel, which weakens the structural integrity of the electrode and compromises its performance. This problem is exacerbated during the fabrication, installation, and high-temperature operation stages, where mechanical stresses such as thermal cycling and vibrations can lead to failure. Proton conductors also exhibit high water absorption, which leads to chemical expansion, powdering, and hydrolysis, thus further decreasing their mechanical strength. Similarly, air electrodes require high water uptake to improve ORR/OER activity, but this leads to similar issues of chemical expansion, water-induced degradation, and TEC mismatches, which can result in cracks, delamination, and other structural problems, thereby reducing the overall mechanical stability of the cell. Fortunately, in a recent study, Yang et al.^[159] introduced a chemical hydration strategy to counteract thermal expansion, thereby enhancing the mechanical stiffness and fracture strength of the air electrode. This strategy promotes thermo-mechanical durability in proton-conducting ceramic cells by strengthening intergranular bonding within the bulk air electrode after hydration, which effectively prevents granule detachment during thermal contraction. This work highlights the importance of bulk-phase mechanical engineering in improving the structural robustness of PCEC.

7.4. Material Degradation

Durability concerns are particularly important in high-temperature, high-humidity environments typical of PCEC operation. In air electrodes, CO₂ reacts with electrode materials under these conditions, leading to chemical degradation, phase structure breakdown, and a reduction in catalytic activity. On the fuel electrode side, Ni coarsening is a common issue, where Ni particles aggregate and reduce the number of available catalytic sites, diminishing the electrode's performance. Furthermore, Ni migration within the electrolyte during operation can impair the proton conductivity of the electrolyte, negatively impacting the overall efficiency of the system. The combination of these degradation mechanisms contributes to the limited longevity and reliability of PCECs, which is a major challenge for their widespread adoption.

7.5. Cost

The commercialization of PCEC technology faces significant challenges, particularly with scalability and cost. Producing defect-free proton-conducting electrolytes on a large scale remains difficult due to the risk of cracks and structural weaknesses during sintering. Achieving uniform densification of these materials requires precise control over the manufacturing process, which is both cost-intensive and technically challenging. The increasing cost of raw materials, including doped perovskite oxides and advanced ceramic composites for electrodes and electrolytes, further complicates the economic feasibility of PCECs. Despite

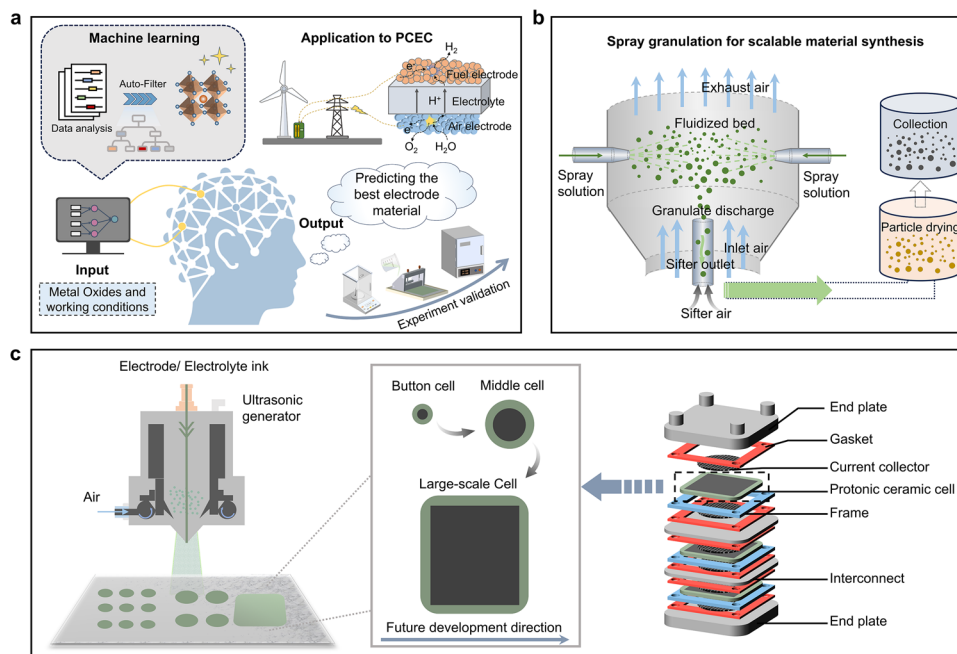


Figure 21. a) Research process illustration of machine learning for advancing PCEC electrode materials. b) The schematic of spray granulation. c) Illustration of the fabricating and testing process for large-scale planar electrolysis cells.

advances in fabrication techniques such as multilayer tape casting, hot pressing, and 3D printing, scaling up from lab-scale button cells to industrial-sized devices remains difficult.^[160] To make PCECs commercially viable, there is a need for cost-effective synthesis and assembly methods. Additionally, PCECs face stiff competition from well-established electrolysis technologies, such as ALK and PEM,^[161] which are already well-integrated into the market. Therefore, PCECs must demonstrate clear performance and cost advantages to capture market share and become commercially competitive.

8. Future Perspective

8.1. Machine Learning for Electrode Materials

Traditional materials development faces several challenges, including long cycles and high trial-and-error costs. With the advancements in artificial intelligence (AI) and the increase in material databases, machine learning (ML) is gradually being applied to materials science. Future research will likely see more AI-assisted design for air electrode materials in PCECs. Various strategies in AI development for PCEC materials and other inorganic non-metallic materials have emerged, with researchers leveraging machine learning models to identify high-performance materials with desired properties.^[162] For instance, machine learning models have been developed to uncover the factors influencing the proton incorporation capabilities of oxides, providing valuable guidance for designing efficient air electrodes, as shown in **Figure 21a**. Combining experimental data with DFT calculations has allowed researchers to validate the prediction accuracy of these machine learning models, particularly regarding proton conductivity and ORR/OER activity.^[163] Machine learning accelerates material discovery, reduces ex-

perimental costs, and optimizes material design, thus significantly promoting the development of new materials. However, challenges remain, such as poor data quality, lack of standardized experimental procedures, and limited understanding of material-property relationships.^[164] Overcoming these barriers will require interdisciplinary collaboration, improved data-sharing practices, and enhanced model explainability to fully unlock the potential of machine learning in material research.

8.2. Standard Protocol for Performance Assessment

While many high-performance electrode materials have been reported, a significant issue remains the lack of standardized testing protocols. Variations in electrode structure (e.g., effective area, porosity, thickness), preparation conditions (e.g., thermal history, coating methods), and test environments (e.g., gas composition, H_2 flow in fuel electrodes, temperature conditions) can lead to inconsistencies in the performance evaluation of electrodes. These inconsistencies complicate comparative studies and hinder the development of reliable performance benchmarks. Inconsistent thermodynamic conditions, such as varying temperature cycles and the effects of gas environments (N_2/O_2 ratios or H_2 flow), also influence electrode behavior. Additionally, the absence of third-party certification and standardized battery testing fixtures increases the risk of experimental errors. The lack of uniform test fixtures—essential for accurate mass transfer and sealing—further contributes to discrepancies in the assessment of electrode materials. Addressing these issues by standardizing testing protocols and establishing certification frameworks would facilitate more meaningful comparisons and accelerate the development of reliable, high-performance electrodes.

8.3. Scalable Synthesis for Advanced Materials

Current high-performance electrode materials often require sophisticated and intricate fabrication methods, such as pulsed laser deposition (PLD) for stabilizing the electrode-electrolyte interface.^[125] While these methods significantly enhance cell performance, they are technically complex, require expensive equipment, and are challenging to scale up for industrial applications. Additionally, materials prepared using techniques like sol-gel methods, though commonly employed in research, are not suitable for large-scale industrial production due to time-consuming processes and complex steps. For technology to progress toward commercialization, there is a need to focus more on scalable, cost-effective synthesis methods, such as coprecipitation, solid-state synthesis, and spray granulation (Figure 21b). By adopting these methods, the development of electrode materials and water electrolysis technologies can better align with industrial manufacturing needs, reducing costs and enabling broader implementation of PCEC technologies in large-scale systems.

8.4. Validation in Large-scale Cells

Electrodes that exhibit excellent performance in small-scale button cells often struggle to deliver similar results in large-scale systems. In button cells, high water vapor content alleviates the bottleneck caused by proton conductivity and proton uptake capabilities, enabling high performance. However, in larger cells, the need for efficient water vapor utilization and the presence of localized hot spots impose stricter demands on the electrode's water absorption capacity. Additionally, the electronic conductivity and interconnection compatibility in larger cells can limit performance, even if these factors do not pose significant issues in smaller cells. Therefore, performance optimization should not only focus on button cells but also consider large-scale electrolysis systems and stacks, where the electrochemical conditions differ significantly. Recently, research efforts have gradually expanded beyond button cells to investigate larger-scale cells.^[165] Moreover, attention has also been shifting toward the design and testing of large-scale planar electrolysis cells,^[165,166] as shown in Figure 21c. For future research, it is essential to extend the testing and development of electrode materials to larger cells to better understand how they perform under the operational conditions typical of commercial devices.

Looking ahead, further advancements in the development of electrode materials are crucial for enhancing the efficiency and scalability of PCECs. Future research should focus on improving the stability, durability, and long-term performance of both the fuel and air electrodes while refining material synthesis methods to meet the demands of large-scale production. Optimizing the interaction between electrode materials and electrolytes will also be essential to boost the overall performance of PCECs. In addition, leveraging cutting-edge technologies such as machine learning and standardizing performance assessment protocols will help accelerate material discovery and innovation. As PCEC technology matures, these advancements will be pivotal in unlocking its full potential for efficient and sustainable hydrogen production, position-

ing PCECs as a promising solution for future clean energy applications.

Acknowledgements

Z.L. and L.Z. contributed equally to this work. This work was supported by grants from the National Natural Science Foundation of China (22405228), the Guangdong Basic and Applied Basic Research Foundation (No. 2023A1515110259, 2025A1515011951), the Strategic Hiring Scheme (BDD3) and Research Centre for Carbon-Strategic Catalysis (CE01) of The Hong Kong Polytechnic University. C.J.Z. was involved in this work supported by JRMF (Junior Researcher Mentoring Programme) hosted by The Hong Kong Polytechnic University.

Conflict of Interest

The authors declare no conflict of interest.

Keywords

advanced electrode materials, hydrogen production, protonic ceramic electrolysis cells, water electrolysis

Received: February 21, 2025

Revised: May 16, 2025

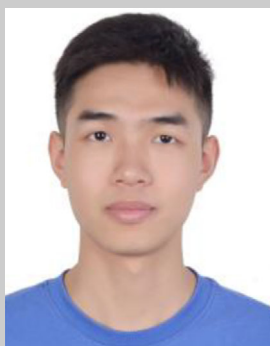
Published online:

- [1] a) A. Odenweller, F. Ueckerdt, G. F. Nemet, M. Jensterle, G. Luderer, *Nat. Energy* **2022**, 7, 854; b) Y. Wang, F. Chu, J. Zeng, Q. Wang, T. Naren, Y. Li, Y. Cheng, Y. Lei, F. Wu, *ACS Nano* **2021**, 15, 210; c) X. Yang, C. P. Nielsen, S. Song, M. B. McElroy, *Nat. Energy* **2022**, 7, 955.
- [2] a) C. Lei, W. Zhou, Q. Feng, Y. Lei, Y. Zhang, Y. Chen, J. Qin, *Nano-Micro Lett.* **2019**, 11, 45; b) R. Xu, R. Sun, H.-Q. Xu, G. Xie, J. Ge, *J. Mater. Chem. A* **2024**, 12, 26316.
- [3] a) L. Chen, Y. Song, Y. Liu, L. Xu, J. Qin, Y. Lei, Y. Tang, *J. Energy Chem.* **2020**, 50, 395; b) A. Hauch, R. Kungas, P. Blennow, A. B. Hansen, J. B. Hansen, B. V. Mathiesen, M. B. Mogensen, *Science* **2020**, 370, aba6118; c) J. T. S. Irvine, D. Neagu, M. C. Verbraeken, C. Chatzichristodoulou, C. Graves, M. B. Mogensen, *Nat. Energy* **2016**, 1, 15014; d) M. Mohebbi Nejad, P. Ahmadi, E. Houshfar, *Fuel* **2023**, 336, 126835.
- [4] Y. Song, X. Zhang, K. Xie, G. Wang, X. Bao, *Adv. Mater.* **2019**, 31, 1902033.
- [5] Z. Lei, C. I. Sathish, Y. Liu, A. Karokoti, J. Wang, L. Qiao, A. Vinu, *J. Yi, EcoMat* **2022**, 4, 12186.
- [6] P. Moçoteguy, A. Brisse, *Int. J. Hydrogen Energy* **2013**, 38, 15887.
- [7] A. V. Kasyanova, I. A. Zvonareva, N. A. Tarasova, L. Bi, D. A. Medvedev, Z. Shao, *Mater. Rep.s: Energy* **2022**, 2, 100158.
- [8] Q. Hu, C. Tian, D. Bao, H. Zhong, X. Zhang, *Next Energy* **2024**, 4, 100144.
- [9] Y. Zhang, R. Knibbe, J. Sunarso, Y. Zhong, W. Zhou, Z. Shao, Z. Zhu, *Adv. Mater.* **2017**, 29, 1770345.
- [10] a) J. Chi, H. Yu, *Chin. J. Catal.* **2018**, 39, 390; b) F. M. Sapountzi, J. M. Gracia, C. J. Weststrate, H. O. A. Fredriksson, J. W. Niemantsverdriet, *Prog. Energy Combust. Sci.* **2017**, 58, 1; c) S. S. Kumar, H. Lim, *Energy Rep* **2022**, 8, 13793.
- [11] L. Bi, S. Boulfrad, E. Traversa, *Chem. Soc. Rev.* **2014**, 43, 8255.
- [12] M. Choi, D. Kim, T. K. Lee, J. Lee, H. S. Yoo, W. Lee, *Adv. Energy Mater.* **2024**, 15, 2400124.

- [13] a) N. Wang, H. Toriumi, Y. Sato, C. Tang, T. Nakamura, K. Amezawa, S. Kitano, H. Habazaki, Y. Aoki, *ACS Appl. Energy Mater.* **2020**, *4*, 554; b) H. Ding, W. Wu, C. Jiang, Y. Ding, W. Bian, B. Hu, P. Singh, C. J. Orme, L. Wang, Y. Zhang, D. Ding, *Nat. Commun.* **2020**, *11*, 1907.
- [14] a) K. Zhu, L. Zhang, N. Shi, B. Qiu, X. Hu, D. Huan, C. Xia, R. Peng, Y. Lu, *ACS Nano* **2024**, *18*, 5141; b) W. Tang, H. Ding, W. Bian, W. Wu, W. Li, X. Liu, J. Y. Gomez, C. Y. Regalado Vera, M. Zhou, D. Ding, *J. Mater. Chem. A* **2020**, *8*, 14600.
- [15] a) N. Yu, I. T. Bello, X. Chen, T. Liu, Z. Li, Y. Song, M. Ni, *Nanomicro Lett.* **2024**, *16*, 177; b) L. Yang, X. Ren, W. Peng, A. Wang, D. Yan, J. Li, L. Jia, *J. Power Sources* **2023**, *586*, 233652.
- [16] a) M. Saqib, I.-G. Choi, H. Bae, K. Park, J.-S. Shin, Y.-D. Kim, J.-I. Lee, M. Jo, Y.-C. Kim, K.-S. Lee, S.-J. Song, E. D. Wachsman, J.-Y. Park, *Energy Environ. Sci.* **2021**, *14*, 2472; b) K. Park, H. Bae, H. K. Kim, I. G. Choi, M. Jo, G. M. Park, M. Asif, A. Bhardwaj, K. S. Lee, Y. C. Kim, S. J. Song, E. D. Wachsman, J. Y. Park, *Adv. Energy Mater.* **2022**, *13*, 2202999.
- [17] a) S. Oh, H. Kim, I. Jeong, D. Kim, H. Yu, K. T. Lee, *J. Korean Ceram. Soc.* **2024**, *61*, 224; b) Y. Wang, S. Li, X. Hou, T. Cui, Z. Zhuang, Y. Zhao, H. Wang, W. Wei, M. Xu, Q. Fu, C. Chen, D. Wang, *Adv. Mater.* **2024**, *36*, 2412598.
- [18] D. Sarantaridis, A. Atkinson, *Fuel Cells* **2007**, *7*, 246.
- [19] M. Liang, Y. Song, B. Xiong, D. Liu, D. Xue, L. Shen, K. Shi, Y. Song, J. Li, Q. Niu, *Adv. Funct. Mater.* **2024**, *34*, 2408756.
- [20] M. Wang, L.-C. Wang, H. Li, W. Wu, S. W. Snyder, G. Gao, F. Chen, Y. Yang, D. Ding, *Carbon* **2022**, *199*, 379.
- [21] L. Mingyi, Y. Bo, X. Jingming, C. Jing, *J. Power Sources* **2008**, *177*, 493.
- [22] P. Kazempoor, R. J. Braun, *Int. J. Hydrogen Energy* **2014**, *39*, 2669.
- [23] K. D. Kreuer, *Annu. Rev. Mater. Res.* **2003**, *33*, 333.
- [24] N. Wang, S. Hinokuma, T. Ina, H. Toriumi, M. Katayama, Y. Inada, C. Zhu, H. Habazaki, Y. Aoki, *Chem. Mater.* **2019**, *31*, 8383.
- [25] a) Q. Li, Q. Yin, Y. S. Zheng, Z. J. Sui, X. G. Zhou, D. Chen, Y. A. Zhu, *Langmuir* **2019**, *35*, 9962; b) T. Ueki, M. Watanabe, *Macromol* **2008**, *41*, 3739.
- [26] J. Kim, S. Sengodan, S. Kim, O. Kwon, Y. Bu, G. Kim, *Renew. Sustain. Energy Rev.* **2019**, *109*, 606.
- [27] I. N. Sora, V. Felice, F. Fontana, *Chem. Eng. Trans.* **2015**, *43*, 1753.
- [28] C. Duan, J. Tong, M. Shang, S. Nikodemski, M. Sanders, S. Ricote, A. Almansoori, R. O'Hayre, *Science* **2015**, *349*, 1321.
- [29] H. Tian, Z. Luo, Y. Song, Y. Zhou, M. Gong, W. Li, Z. Shao, M. Liu, X. Liu, *Int. Mater. Rev.* **2023**, *68*, 272.
- [30] a) J. H. Lee, H. Kim, S. M. Kim, T. W. Noh, H. Y. Jung, H. Y. Lim, H. G. Jung, J. W. Son, H. R. Kim, B. K. Kim, *Adv. Energy Mater.* **2012**, *2*, 461; b) J. Kim, A. Jun, J. Shin, G. Kim, *J. Am. Ceram. Soc.* **2014**, *97*, 651; c) D. Ding, M. Liu, Z. Liu, X. Li, K. Blinn, X. Zhu, M. Liu, *Adv. Energy Mater.* **2013**, *3*, 1149.
- [31] a) C. Sındırac, *Izmir Institute of Technology (Turkey)* **2019**, 28472684; b) Z. Shao, S. M. Haile, *Nature* **2004**, *431*, 170; c) Y. Zhang, G. Yang, G. Chen, R. Ran, W. Zhou, Z. Shao, *ACS Appl. Mater. Interfaces* **2016**, *8*, 3003.
- [32] W. Huang, C. Tian, J. Meng, N. Xu, Y. Zhang, L. Zhao, H. Zhong, *J. Phys. Chem. C* **2024**, *128*, 10826.
- [33] L. R. Tarutina, M. A. Gordeeva, D. E. Matkin, M. T. Akopian, G. N. Starostin, A. V. Kasyanova, A. P. Tarutin, N. A. Danilov, I. A. Starostina, D. A. Medvedev, *Chem. Eng. J.* **2024**, *490*, 151615.
- [34] M. Liang, Y. Song, D. Liu, L. Xu, M. Xu, G. Yang, W. Wang, W. Zhou, R. Ran, Z. Shao, *Appl. Catal. B-Environ.* **2022**, *318*, 121868.
- [35] M. Liang, F. He, C. Zhou, Y. Chen, R. Ran, G. Yang, W. Zhou, Z. Shao, *Chem. Eng. J.* **2021**, *420*, 127717.
- [36] Y. Shin, Y.-D. Kim, M. Sanders, S. P. Harvey, M. Walker, R. O'Hayre, *J. Mater. Chem. A* **2022**, *10*, 24839.
- [37] H. Ding, W. Wu, C. Jiang, Y. Ding, W. Bian, B. Hu, P. Singh, C. J. Orme, L. Wang, Y. Zhang, *Nat. Commun.* **2020**, *11*, 1907.
- [38] R. Liu, S. Kim, S. Taniguchi, T. Oshima, Y. Shiratori, K. Ito, K. Sasaki, *J. Power Sources* **2011**, *196*, 7090.
- [39] X. Xu, W. Wang, W. Zhou, Z. Shao, *Small Methods* **2018**, *2*, 1800071.
- [40] A. Taskin, A. Lavrov, Y. Ando, *Prog. Solid State Chem.* **2007**, *35*, 481.
- [41] a) M. Burriel, J. Peña-Martínez, R. J. Chater, S. Fearn, A. V. Berenov, S. J. Skinner, J. A. Kilner, *Chem. Mater.* **2012**, *24*, 613; b) J. H. Kim, L. Moggi, F. Prado, A. Caneiro, J. A. Alonso, A. Manthiram, *J. Electrochem. Soc.* **2009**, *156*, B1376.
- [42] a) D. Ávila-Brandé, G. King, E. Urones-Garrote, A. Llobet, S. García-Martín, *Adv. Funct. Mater.* **2014**, *24*, 2510; b) J. Kim, S. Sengodan, G. Kwon, D. Ding, J. Shin, M. Liu, G. Kim, *ChemSusChem* **2014**, *7*, 2811.
- [43] M. Papac, V. Stevanović, A. Zakutayev, R. O'Hayre, *Nat. Mater.* **2021**, *20*, 301.
- [44] E. Völlestad, R. Strandbakke, M. Tarach, D. Catalán-Martínez, M.-L. Fontaine, D. Beeff, D. R. Clark, J. M. Serra, T. Norby, *Nat. Mater.* **2019**, *18*, 752.
- [45] J. Pan, Y. Ye, M. Zhou, X. Sun, Y. Chen, *Energy Fuels* **2022**, *36*, 12253.
- [46] K. Xu, H. Zhang, Y. Xu, F. He, Y. Zhou, Y. Pan, J. Ma, B. Zhao, W. Yuan, Y. Chen, *Adv. Funct. Mater.* **2022**, *32*, 2110998.
- [47] Y. Zhou, E. Liu, Y. Chen, Y. Liu, L. Zhang, W. Zhang, Z. Luo, N. Kane, B. Zhao, L. Soule, *ACS Energy Lett.* **2021**, *6*, 1511.
- [48] Z. Du, W. Gong, K. Xu, F. Zhu, X. Zhang, Y. Chen, *J. Mater. Chem. A* **2024**, *12*, 28066.
- [49] Z. Du, F. He, H. Gao, Y. Xu, F. Zhu, K. Xu, J. Xia, H. Zhang, Y. Huang, Y. Liu, *Energy Storage Mater.* **2024**, *68*, 103345.
- [50] S. Park, Y. Kim, Y. Noh, T. Kim, H. Han, W. Yoon, J. Choi, S.-H. Yi, W.-J. Lee, W. B. Kim, *J. Mater. Chem. A* **2020**, *8*, 138.
- [51] X. Xu, Y. Pan, Y. Zhong, R. Ran, Z. Shao, **2020**, *Mater. Horiz.* *7*, 2519.
- [52] a) Z. Wang, W. Yang, Z. Zhu, R. Peng, X. Wu, C. Xia, Y. Lu, *J. Mater. Chem. A* **2014**, *2*, 16707; b) J. Hermet, M. Torrent, F. Bottin, G. Dezanneau, G. Geneste, *Phys. Rev. B Condens. Matter Mater. Phys.* **2013**, *87*, 104303.
- [53] Y. Chen, W. Zhou, D. Ding, M. Liu, F. Ciucci, M. Tade, Z. Shao, *Adv. Energy Mater.* **2015**, *5*, 1500537.
- [54] J. Druce, T. Ishihara, J. Kilner, *Solid State Ionics* **2014**, *262*, 893.
- [55] S. Chaianansutcharit, K. Hosoi, J. Hyodo, Y.-W. Ju, T. Ishihara, *J. Mater. Chem. A* **2015**, *3*, 12357.
- [56] J.-M. Bassat, P. Odier, A. Villesuzanne, C. Marin, M. Pouchard, *Solid State Ionics* **2004**, *167*, 341.
- [57] E. Boehm, J.-M. Bassat, P. Dordor, F. Mauvy, J.-C. Grenier, P. Stevens, *Solid State Ionics* **2005**, *176*, 2717.
- [58] A. Gilev, E. Kiselev, V. Cherepanov, *J. Mater. Chem. A* **2018**, *6*, 5304.
- [59] X.-D. Zhou, J. W. Templeton, Z. Nie, H. Chen, J. W. Stevenson, L. R. Pederson, *Electrochim. Acta* **2012**, *71*, 44.
- [60] L. Lei, J. Zhang, Z. Yuan, J. Liu, M. Ni, F. Chen, *Adv. Funct. Mater.* **2019**, *29*, 1903805.
- [61] C. Duan, J. Huang, N. Sullivan, R. O'Hayre, *Appl. Phys. Rev.* **2020**, *7*, 011314.
- [62] L. Schley, V. Vibhu, L. Nohl, I. C. Vinke, L. B. de Haart, R.-A. Eichel, *Energy Adv* **2024**, *3*, 861.
- [63] T. Murakami, J. R. Hester, M. Yashima, *J. Am. Chem. Soc.* **2020**, *142*, 11653.
- [64] H. Yang, P. Duan, Z. Zhuang, Y. Luo, J. Shen, Y. Xiong, X. Liu, D. Wang, *Adv. Mater.* **2025**, *37*, 2415265.
- [65] a) C. Duan, R. Kee, H. Zhu, N. Sullivan, L. Zhu, L. Bian, D. Jennings, R. O'Hayre, *Nat. Energy* **2019**, *4*, 230; b) Z. Liu, M. Zhou, M. Chen, D. Cao, J. Shao, M. Liu, J. Liu, *Ceram. Int.* **2020**, *46*, 19952.
- [66] C. Duan, R. J. Kee, H. Zhu, C. Karakaya, Y. Chen, S. Ricote, A. Jarry, E. J. Crumlin, D. Hook, R. Braun, *Nature* **2018**, *557*, 217.
- [67] D. Neagu, T.-S. Oh, D. N. Miller, H. Ménard, S. M. Bukhari, S. R. Gamble, R. J. Gorte, J. M. Vohs, J. T. Irvine, *Nat. Commun.* **2015**, *6*, 8120.
- [68] Y. Liu, Z. Shao, T. Mori, S. P. Jiang, *Mater. Rep.: Energy* **2021**, *1*, 100003.
- [69] S. Bi, C. Ye, Y. Liu, Y. Zhang, Y. Wang, Z. Liu, M. Wang, L. Zhou, X. Lin, L. Zhang, *J. Am. Ceram. Soc.* **2023**, *106*, 6911.

- [70] Y. Song, J. Liu, Y. Wang, D. Guan, A. Seong, M. Liang, M. J. Robson, X. Xiong, Z. Zhang, G. Kim, *Adv. Energy Mater.* **2021**, *11*, 2101899.
- [71] H. An, H.-W. Lee, B.-K. Kim, J.-W. Son, K. J. Yoon, H. Kim, D. Shin, H.-I. Ji, J.-H. Lee, *Nat. Energy* **2018**, *3*, 870.
- [72] Z. Huang, Y. Yang, H. Lv, C. Shi, T. Li, Y. Ling, T. Chen, S. Wang, *J. Eur. Ceram. Soc.* **2023**, *43*, 428.
- [73] M. Marrony, M. Ancelin, G. Lefevre, J. Dailly, *Solid State Ionics* **2015**, *275*, 97.
- [74] M. B. Mogensen, M. Chen, H. L. Frandsen, C. Graves, A. Hauch, P. V. Hendriksen, T. Jacobsen, S. H. Jensen, T. L. Skafte, X. Sun, *Fuel Cells* **2021**, *21*, 415.
- [75] C. Sun, J. A. Alonso, J. Bian, *Adv. Energy Mater.* **2021**, *11*, 2000459.
- [76] Y. Zhang, B. Chen, D. Guan, M. Xu, R. Ran, M. Ni, W. Zhou, R. O'Hayre, Z. Shao, *Nature* **2021**, *591*, 246.
- [77] X. Xu, H. Wang, M. Fronzi, X. Wang, L. Bi, E. Traversa, *J. Mater. Chem. A* **2019**, *7*, 20624.
- [78] K. Park, M. Saqib, H. Lee, D. Shin, M. Jo, K. M. Park, M. Hamayun, S. H. Kim, S. Kim, K.-S. Lee, R. O'Hayre, M. Choi, S.-J. Song, J.-Y. Park, *Energy Environ. Sci.* **2024**, *17*, 1175.
- [79] A. Mahata, P. Datta, R. N. Basu, *Ceram. Int.* **2017**, *43*, 433.
- [80] P. Zhong, K. Toyoura, L. Jiang, L. Chen, S. A. Ismail, N. Hatada, T. Norby, D. Han, *Adv. Energy Mater.* **2022**, *12*, 2200392.
- [81] W. Li, B. Guan, T. Yang, Z. Li, W. Shi, H. Tian, L. Ma, T. L. Kalapos, X. Liu, *J. Power Sources* **2021**, *495*, 229764.
- [82] R. Ren, Z. Wang, C. Xu, W. Sun, J. Qiao, D. W. Rooney, K. Sun, *J. Mater. Chem. A* **2019**, *7*, 18365.
- [83] Y. Yang, H. Bao, H. Ni, X. Ou, S. Wang, B. Lin, P. Feng, Y. Ling, *J. Power Sources* **2021**, *482*, 228959.
- [84] F. He, Y. Zhou, T. Hu, Y. Xu, M. Hou, F. Zhu, D. Liu, H. Zhang, K. Xu, M. Liu, Y. Chen, *Adv. Mater.* **2023**, *35*, 2209469.
- [85] Z. Liu, Z. Tang, Y. Song, G. Yang, W. Qian, M. Yang, Y. Zhu, R. Ran, W. Wang, W. Zhou, Z. Shao, *Nanomicro Lett.* **2022**, *14*, 217.
- [86] F. He, M. Hou, D. Liu, Y. Ding, K. Sasaki, Y. Choi, S. Guo, D. Han, Y. Liu, M. Liu, Y. Chen, *Energy Environ. Sci.* **2024**, *17*, 3898.
- [87] a) B. Wang, G. Long, Y. Li, H. Jia, D. Qiu, J. Wang, G. Liu, K. Wang, Y. Ji, *Int. J. Hydrogen Energy* **2018**, *43*, 6677; b) Y. P. Fu, A. Subardi, M. Y. Hsieh, W. K. Chang, J. Stevenson, *J. Am. Ceram. Soc.* **2016**, *99*, 1345.
- [88] L. Li, H. Yang, Z. Gao, Y. Zhang, F. Dong, G. Yang, M. Ni, Z. Lin, *J. Mater. Chem. A* **2019**, *7*, 12343.
- [89] G.-M. Park, K. Park, M. Jo, M. Asif, Y. Bae, S.-H. Kim, A. K. Azad, S.-J. Song, J.-Y. Park, *J. Alloys Compd.* **2023**, *968*, 171987.
- [90] Z. Zhu, M. Zhou, K. Tan, Z. Fan, D. Cao, Z. Liu, M. Chen, Y. Chen, M. Chen, J. Liu, *ACS Appl. Mater. Interfaces* **2023**, *15*, 14457.
- [91] X. Cheng, G. Li, R. Ren, C. Xu, J. Qiao, W. Sun, Z. Wang, K. Sun, *Ceram. Int.* **2023**, *49*, 19879.
- [92] Z. Wang, Y. Wang, Y. Xiao, Y. Zhang, X. Wang, F. Wang, T. He, *Small* **2024**, *20*, 2312148.
- [93] D. Kim, I. Jeong, S. Ahn, S. Oh, H. N. Im, H. Bae, S. J. Song, C. W. Lee, W. Jung, K. T. Lee, *Adv. Energy Mater.* **2024**, *14*, 2304059.
- [94] C. Lu, R. Ren, Z. Zhu, G. Pan, G. Wang, C. Xu, J. Qiao, W. Sun, Q. Huang, H. Liang, Z. Wang, K. Sun, *Chem. Eng. J.* **2023**, *472*, 144878.
- [95] Z. Liu, D. Cheng, Y. Zhu, M. Liang, M. Yang, G. Yang, R. Ran, W. Wang, W. Zhou, Z. Shao, *Chem. Eng. J.* **2022**, *450*, 137787.
- [96] F. H. Taylor, J. Buckeridge, C. R. A. Catlow, *Chem. Mater.* **2017**, *29*, 8147.
- [97] S. Choi, S. Yoo, J. Kim, S. Park, A. Jun, S. Sengodan, J. Kim, J. Shin, H. Y. Jeong, Y. Choi, *Sci. Rep.* **2013**, *3*, 2426.
- [98] K. Pei, Y. Zhou, K. Xu, H. Zhang, Y. Ding, B. Zhao, W. Yuan, K. Sasaki, Y. Choi, Y. Chen, M. Liu, *Nat. Commun.* **2022**, *13*, 2207.
- [99] M. Liang, Y. Wang, Y. Song, D. Guan, J. Wu, P. Chen, A. Maradesa, M. Xu, G. Yang, W. Zhou, W. Wang, R. Ran, F. Ciucci, Z. Shao, *Appl. Catal. B-Environ.* **2023**, *331*, 122682.
- [100] S. Xu, H. Qiu, S. Jiang, J. Jiang, W. Wang, X. Xu, W. Kong, T. D. Chivurugwi, A. Proskurin, D. Chen, C. Su, *Nano Res.* **2024**, *17*, 8086.
- [101] C. Yang, Y. Tian, C. Yang, G. Kim, J. Pu, B. Chi, *Adv. Sci.* **2023**, *10*, 2304224.
- [102] V. Dhongde, A. Singh, J. Kala, U. Anjum, M. A. Haider, S. Basu, *Mater. Rep. Energy* **2022**, *2*, 100095.
- [103] W. Wang, Y. Yang, D. Huan, L. Wang, N. Shi, Y. Xie, C. Xia, R. Peng, Y. Lu, *J. Mater. Chem. A* **2019**, *7*, 12538.
- [104] X. Li, T. Xia, Z. Dong, J. Wang, Q. Li, L. Sun, L. Huo, H. Zhao, *Mater. Today Chem.* **2023**, *29*, 101469.
- [105] L. Zhang, W. Sun, C. Xu, R. Ren, X. Yang, J. Qiao, Z. Wang, K. Sun, *J. Mater. Chem. A* **2020**, *8*, 14091.
- [106] T. Sivakumar, J. B. Wiley, *Mater. Res. Bull.* **2009**, *44*, 74.
- [107] G. Li, Y. Gou, R. Ren, C. Xu, J. Qiao, W. Sun, Z. Wang, K. Sun, *J. Power Sources* **2021**, *508*, 230343.
- [108] W. Guo, R. Guo, L. Liu, G. Cai, C. Zhang, C. Wu, Z. Liu, H. Jiang, *Int. J. Hydrogen Energy* **2015**, *40*, 12457.
- [109] N. Tarasova, I. Animitsa, *Solid State Ionics* **2018**, *317*, 21.
- [110] Y. Li, Y. Li, Y. Wan, Y. Xie, J. Zhu, H. Pan, X. Zheng, C. Xia, *Adv. Energy Mater.* **2019**, *9*, 1803156.
- [111] A. Trivino-Pelaez, J. Mosa, D. Perez-Coll, M. Aparicio, G. C. Mather, *J. Eur. Ceram. Soc.* **2023**, *43*, 99.
- [112] R. Ren, X. Yu, Z. Wang, C. Xu, T. Song, W. Sun, J. Qiao, K. Sun, *Appl. Catal. B-Environ.* **2022**, *317*, 121759.
- [113] X. Chen, N. Yu, Y. Song, T. Liu, H. Xu, D. Guan, Z. Li, W. H. Huang, Z. Shao, F. Ciucci, *Adv. Mater.* **2024**, *36*, 2403998.
- [114] S. Joo, A. Seong, O. Kwon, K. Kim, J. H. Lee, R. J. Gorte, J. M. Vohs, J. W. Han, G. Kim, *Sci. Adv.* **2020**, *6*, abb1573.
- [115] S. Vafaenezhad, A. R. Hanifi, M. A. Laguna-Bercero, T. H. Etsell, P. Sarkar, *Mater. Futures* **2022**, *1*, 042101.
- [116] Y. Chen, Y. Zhang, J. Baker, P. Majumdar, Z. Yang, M. Han, F. Chen, *ACS Appl. Mater. Interfaces* **2014**, *6*, 5130.
- [117] H. N. Wadley, N. A. Fleck, A. G. Evans, *Compos. Sci. Technol.* **2003**, *63*, 2331.
- [118] a) T. Li, Z. Wu, K. Li, *J. Power Sources* **2014**, *251*, 145; b) S. Smart, C. Lin, L. Ding, K. Thambimuthu, J. D. Da Costa, *Energy Environ. Sci.* **2010**, *3*, 268.
- [119] B. Chen, H. Xu, M. Ni, *Sci. Bull.* **2016**, *61*, 1324.
- [120] a) M. Hou, F. Zhu, Y. Liu, Y. Chen, *J. Eur. Ceram. Soc.* **2023**, *43*, 6200; b) L. Zhao, X. Zhang, B. He, B. Liu, C. Xia, *J. Power Sources* **2011**, *196*, 962.
- [121] Y. Pan, K. Pei, Y. Zhou, T. Liu, M. Liu, Y. Chen, *J. Mater. Chem. A* **2021**, *9*, 10789.
- [122] Y. Ling, F. Huang, B. Wang, T. Li, *Electrochem. Commun.* **2024**, *166*, 107775.
- [123] A. Tarutin, A. Kasyanova, J. Lyagaeva, G. Vdovin, D. Medvedev, *J. Energy Chem.* **2020**, *40*, 65.
- [124] A. Zekri, K. Herbrig, M. Knipper, J. Parisi, T. Plaggenborg, *Fuel Cells* **2017**, *17*, 359.
- [125] S. Choi, C. J. Kucharczyk, Y. Liang, X. Zhang, I. Takeuchi, H.-I. Ji, S. M. Haile, *Nat. Energy* **2018**, *3*, 202.
- [126] S. J. Yang, W. Chang, H. J. Jeong, D. H. Kim, J. H. Shim, *Int. J. Energy Res.* **2021**, *46*, 6553.
- [127] A. Hauch, K. Brodersen, M. Chen, M. B. Mogensen, *Solid State Ionics* **2016**, *293*, 27.
- [128] X. Chen, J. Lin, L. Sun, T. Liu, J. Wu, Z. Sheng, Y. Wang, *Electrochim. Acta* **2019**, *298*, 112.
- [129] N. Ai, Z. Lü, K. Chen, X. Huang, X. Du, W. Su, *J. Power Sources* **2007**, *171*, 489.
- [130] S. D. Ebbesen, X. Sun, M. B. Mogensen, *Faraday Discuss.* **2015**, *182*, 393.
- [131] B. H. Rainwater, M. Liu, M. Liu, *Int. J. Hydrogen Energy* **2012**, *37*, 18342.

- [132] Q. Wang, X. Tong, S. Ricote, R. Sažinas, P. V. Hendriksen, M. Chen, *Adv. Powder Mater.* **2022**, *1*, 100003.
- [133] M. Saqib, J.-I. Lee, J.-S. Shin, K. Park, Y.-D. Kim, K. B. Kim, J. H. Kim, H.-T. Lim, J.-Y. Park, *J. Electrochem. Soc.* **2019**, *166*, F746.
- [134] Y. Zhou, W. Zhang, N. Kane, Z. Luo, K. Pei, K. Sasaki, Y. Choi, Y. Chen, D. Ding, M. Liu, *Adv. Funct. Mater.* **2021**, *31*, 2105386.
- [135] Y. Niu, Y. Zhou, W. Zhang, Y. Zhang, C. Evans, Z. Luo, N. Kane, Y. Ding, Y. Chen, X. Guo, W. Lv, M. Liu, *Adv. Energy Mater.* **2022**, *12*, 2103783.
- [136] K. Pei, S. Luo, F. He, J. Arbiol, Y. Xu, F. Zhu, Y. Wang, Y. Chen, *Appl. Catal. B-Environ.* **2023**, *330*, 122601.
- [137] Y. Wang, K. Pei, B. Zhao, Y. Zhao, H. Wang, Q. Niu, Y. Chen, *Energy Fuels* **2021**, *35*, 14101.
- [138] Z. Wang, P. Lv, L. Yang, R. Guan, J. Jiang, F. Jin, T. He, *Ceram. Int.* **2020**, *46*, 18216.
- [139] C. Yang, X. Zhang, H. Zhao, Y. Shen, Z. Du, C. Zhang, *Int. J. Hydrogen Energy* **2015**, *40*, 2800.
- [140] S. J. Yang, W. Chang, H. J. Jeong, D. H. Kim, J. H. Shim, *Int. J. Energy Res.* **2022**, *46*, 6553.
- [141] H. Zheng, M. Riegraf, N. Sata, R. Costa, *J. Mater. Chem. A* **2023**, *11*, 10955.
- [142] B. A. Rosen, *Electrochem.* **2020**, *1*, 32.
- [143] O. Celikbilek, C.-A. Thieu, F. Agnese, E. Call, C. Lenser, N. H. Menzler, J.-W. Son, S. J. Skinner, E. Djurado, *J. Mater. Chem. A* **2019**, *7*, 25102.
- [144] M. Liang, Y. Zhu, Y. Song, D. Guan, Z. Luo, G. Yang, S. P. Jiang, W. Zhou, R. Ran, Z. Shao, *Adv. Mater.* **2022**, *34*, 2106379.
- [145] E. Y. Konyshcheva, X. Xu, J. Irvine, *Adv. Mater.* **2012**, *24*, 528.
- [146] a) M. Li, B. Hua, L.-C. Wang, J. D. Sugar, W. Wu, Y. Ding, J. Li, D. Ding, *Nat. Catal.* **2021**, *4*, 274; b) K. Pei, Y. Zhou, Y. Ding, K. Xu, H. Zhang, W. Yuan, K. Sasaki, Y. Choi, M. Liu, Y. Chen, *J. Power Sources* **2021**, *514*, 230573.
- [147] D. Ding, X. Li, S. Y. Lai, K. Gerdes, M. Liu, *Energy Environ. Sci.* **2014**, *7*, 552.
- [148] Y. Song, Y. Chen, W. Wang, C. Zhou, Y. Zhong, G. Yang, W. Zhou, M. Liu, Z. Shao, *Joule* **2019**, *3*, 2842.
- [149] X. Zhang, R. Song, D. Huan, K. Zhu, X. Li, H. Han, C. Xia, R. Peng, Y. Lu, *Small* **2022**, *18*, 2205190.
- [150] T. Hu, F. Zhu, J. Xia, F. He, Z. Du, Y. Zhou, Y. Liu, H. Wang, Y. Chen, *Adv. Funct. Mater.* **2023**, *33*, 2305567.
- [151] Y. Huang, F. He, K. Xu, H. Gao, X. Zhang, Y. Xu, Z. Du, F. Zhu, W. Gong, C. Jian, *Adv. Funct. Mater.* **2024**, *34*, 2409598.
- [152] C. Berger, E. Bucher, R. Merkle, C. Nader, J. Lammer, W. Grogger, J. Maier, W. Sitte, *J. Mater. Chem. A* **2022**, *10*, 2474.
- [153] S. Cheng, Y. Wang, L. Zhuang, J. Xue, Y. Wei, A. Feldhoff, J. Caro, H. Wang, *Angew. Chem., Int. Ed.* **2016**, *55*, 10895.
- [154] Y. Wang, Y. Ling, B. Wang, G. Zhai, G. Yang, Z. Shao, R. Xiao, T. Li, *Energy Environ. Sci.* **2023**, *16*, 5721.
- [155] A. N. Zainon, M. R. Somalu, A. M. K. Bahrain, A. Muchtar, N. A. Baharuddin, M. A. SA, N. Osman, A. A. Samat, A. K. Azad, N. P. Brandon, *Int. J. Hydrogen Energy* **2023**, *48*, 20441.
- [156] J. Cao, Y. Ji, Z. Shao, *Energy Environ. Sci.* **2022**, *15*, 2200.
- [157] C. Zhou, X. Shen, D. Liu, J. Cui, Y. Yi, M. Fei, J. Zhou, L. Zhang, R. Ran, M. Xu, *J. Power Sources* **2022**, *530*, 231321.
- [158] L. Q. Le, C. Meisel, C. H. Hernandez, J. Huang, Y. Kim, R. O'Hayre, N. P. Sullivan, *J. Power Sources* **2022**, *537*, 231356.
- [159] H. Yang, Y. Zhang, Z. Liu, C. Hu, J. Li, H. Liao, M. Shao, M. Ni, B. Chen, Z. Shao, H. Xie, *Nat. Commun.* **2025**, *16*, 3154.
- [160] N. Li, A. Zarkadoulas, V. Kyriakou, *Prog. Energy* **2024**, *6*, 043007.
- [161] A. Lahrichi, Y. El Issmaeli, S. S. Kalanur, B. G. Pollet, *J. Energy Chem.* **2024**, *94*, 688.
- [162] J. Wei, X. Chu, X.-Y. Sun, K. Xu, H.-X. Deng, J. Chen, Z. Wei, M. Lei, *InfoMat* **2019**, *1*, 338.
- [163] N. Wang, B. Yuan, C. Tang, L. Du, R. Zhu, Y. Aoki, W. Wang, L. Xing, S. Ye, *Adv. Mater.* **2022**, *34*, 2203446.
- [164] B. Yuan, N. Wang, C. Tang, L. Meng, L. Du, Q. Su, Y. Aoki, S. Ye, *Nano Energy* **2024**, *122*, 109306.
- [165] R. J. Braun, A. Dubois, K. Ferguson, C. Duan, C. Karakaya, R. J. Kee, H. Zhu, N. P. Sullivan, E. Tang, M. Pastula, *ECS Trans.* **2019**, *91*, 997.
- [166] L. Q. Le, C. H. Hernandez, M. H. Rodriguez, L. Zhu, C. Duan, H. Ding, R. P. O'Hayre, N. P. Sullivan, *J. Power Sources* **2021**, *482*, 228868;



Zhipeng Liu is currently pursuing his Ph.D. at The Hong Kong Polytechnic University under the supervision of Prof. Jingjie Ge. His research involves the development of high-performance perovskite-based materials for protonic ceramic cells in high-temperature energy conversion systems, along with large-scale cell fabrication and stack design.



Lilin Zhang is currently pursuing his Ph.D. at The Hong Kong Polytechnic University under the supervision of Prof. Jingjie Ge. He holds a Bachelor's and a Master's degrees from Zhengzhou University. His current research focuses on the rational design and efficient synthesis of single-atom catalysts and PCEC air electrode materials for sustainable energy applications.



Bin Chen received his PhD degree in Mechanical Engineering from The Hong Kong Polytechnic University. He is currently an associate professor in the College of Civil and Transportation Engineering, Shenzhen University. His research interests include advanced energy materials and energy conversion devices, such as fuel cells and electrolyzers. He has published over 80 papers in international academic SCI journals, with an H-index of 40.



Jingjie Ge is an Assistant Professor in the Department of Applied Biology and Chemical Technology at The Hong Kong Polytechnic University. She received her Ph.D. from the University of Science and Technology of China (USTC). Her current research focuses on the atomic precision design of nanocatalysts for green chemistry and sustainable energy. She has authored or co-authored over 40 SCI papers with an H-index of 23. She is the Young Editorial Committee Member of Nano Research, MedMat, and Materials Reports: Energy.